SURFACE PROPERTIES OF KAOLINITE PARTICLES —THEIR INTERACTIONS AND FLOTATION CONSIDERATIONS

by

Jing Liu

A dissertation submitted to the faculty of
The University of Utah
in partial fulfillment of the requirements for the degree of

Doctor of Philosophy

Department of Metallurgical Engineering

The University of Utah

May 2015

The University of Utah Graduate School

STATEMENT OF DISSERTATION APPROVAL

The dissertation of **Jing Liu**

has been approved by the following supervisory committee members:

Jan D. Miller	, Chair	**10/23/2014** Date Approved
Michael L. Free	, Member	**10/23/2014** Date Approved
Vladimir Hlady	, Member	**10/23/2014** Date Approved
Sanja Miskovic	, Member	**10/23/2014** Date Approved
Xuming Wang	, Member	**10/23/2014** Date Approved

and by **Manoranjan Misra** , Chair/Dean of

the Department/College/School of **Metallurgical Engineering**

and by David B. Kieda, Dean of The Graduate School.

ABSTRACT

Clay minerals, for example kaolinite, have many important applications while at the same time existing as common gangue minerals in the tailings from mineral processing plants during the recovery of valuable resources. To develop improved technology for the processing of kaolinite particles, the surface charging properties of kaolinite are studied in this dissertation. In addition, the dissertation objectives include the investigation of kaolinite particle interactions and the analysis of the reverse flotation mechanism of kaolinite from bauxite ore.

To prepare ordered edge surfaces of kaolinite particles, a novel protocol was developed. A sandwich sample with kaolinite edge surfaces in between two resin substrates was prepared by ultramicrotome. The charge of the edge surfaces was found to be negative above pH 4 using atomic force microscopy. In addition, the ionic strength effect on the charge of selected phyllosilicates was investigated. It is found that the magnitude of the charge of the silica faces is dependent on the degree of isomorphous substitution and is not so dependent on the ionic strength. However, the charges of the alumina face and the edge surfaces of kaolinite particles are related to the ionic strength.

The kaolinite particle interactions were investigated by Brownian dynamics simulation using a coarse-grained model. At low pH, aggregated particle structures/clusters are found to be formed by the electrostatic interactions of silica face to alumina face and alumina face to edge surface. In contrast, the particles are well dispersed and no clusters

are formed at higher pH. The structure of kaolinite clusters was validated by SEM and Micro Computed Tomography.

The nature of the reverse flotation of kaolinite particles from bauxite was analyzed based on the surface properties of kaolinite particles and on particle cluster formation. It is concluded that the cluster size and the exposed silica faces account for effective reverse flotation of kaolinite from bauxite ores at low pH.

It is expected that the findings in this dissertation will provide fundamental understanding for the development of new technologies and reagent schedules to more efficiently process clay minerals, including both flotation and flocculation processes.

TABLE OF CONTENTS

ABSTRACT ..... **iii**

LIST OF TABLES ..... **vii**

ACKNOWLEDGEMENTS ..... **ix**

CHAPTERS

1. INTRODUCTION **1**

1.1 Clay Mineralogy 3
1.2 Surface Features of Kaolinite 6
1.3 Kaolinite Particle Aggregation 9
1.4 Flotation Chemistry of Clay Minerals 10
1.5 Research Objectives 11
1.6 Dissertation Organization 12

2. SURFACE FORCES AT KAOLINITE AND OTHER PHYLLOSILICATE SURFACES **14**

2.1 Introduction 14
2.2 Materials and Methods 17
2.2.1 Materials 17
2.2.2 Sample Preparation 18
2.2.3 Atomic Force Microscopy 19
2.2.4 Tip Evaluation 21
2.2.5 Theoretical Model 22
2.2.6 Molecular Dynamics Simulation 24
2.2.7 Cluster Size Measurements Using PCS 26
2.3 Results and Discussion 26
2.3.1 Properties of Kaolinite Edge Surfaces 26
2.3.2 Effect of Ionic Strength on the Silica Face of Selected Phyllosilicates 35
2.3.3 Effect of Ionic Strength on the Properties of Kaolinite Surfaces 43
2.3.4 Effect of Ionic Strength on the Cluster Size 47
2.4 Summary 49

3. BROWNIAN DYNAMICS SIMULATION OF KAOLINITE PARTICLE

INTERACTIONS AND CLUSTER FORMATION 53

3.1 Introduction 53
3.2 Experimental Methods 57
3.2.1 Coarse-Grained Model 57
3.2.2 Simulation Details 58
3.2.3 Cluster Identification and Description 61
3.2.4 Surface Area of Particle Structures 62
3.2.5 Viscosity Simulation and Calculation Based on Particle Structures 63
3.2.6 SEM Imaging 64
3.2.7 X-ray Micro Computed Tomography 66
3.3 Results and Discussion 67
3.3.1 Effect of pH on Particle Interactions and Particle Structures 67
3.3.2 Ellipsoid Enveloped Clusters 72
3.3.3 Effect of Simulation Time—Aggregated Particle Size and Structure 76
3.3.4 Comparison of Simulated Viscosity with Experimental Results 84
3.3.5 Effect of Ionic Strength on Particle Interactions 89
3.3.6 Validation of Cluster Structure 94
3.4 Summary 100

4. ANALYSIS OF THE REVERSE FLOTATION OF KAOLINITE FROM BAUXITE WITH DODECYL AMINE COLLECTOR 103

4.1 Introduction 103
4.2 Materials and Methods 108
4.2.1 Materials 108
4.2.2 X-ray Diffraction 108
4.2.3 Zeta Potential Measurements 109
4.2.4 Contact Angle Measurements 110
4.3 Results and Discussion 110
4.3.1 Characterization of Gibbsite and Pyrophyllite Samples 110
4.3.2 Effect of pH on the Contact Angle of Kaolinite Model Surfaces 113
4.3.3 Effect of Dodecyl Amine Concentration on the Contact Angle of Kaolinite Model Surfaces 116
4.3.4 Discussion of Reverse Flotation 118
4.4 Summary 121

5. SUMMARY, CONCLUSION, AND RESEARCH RECOMMENDATIONS 123

REFERENCES 128

LIST OF TABLES

Tables

1.1. Chemical composition and features of selected phyllosilicates. R^{2+} represents divalent cation, x represents an integer number..... 5

2.1. Intermolecular potential parameters for kaolinite/water interaction (Berendsen et al. 1981; Cygan et al. 2004)..... 25

2.2. Dominant surface groups on clay edge surfaces and corresponding protonation constants (log K_H) (Hiemstra et al. 1989; Avena et al. 2003; Pokrovsky and Schott 2004; Jodin et al. 2005)..... 33

3.1. The surface charge density of silica and alumina surfaces at 1mM KCl used in the simulation..... 60

3.2. Number of primary kaolinite particles and their corresponding particle size for the simulation..... 69

3.3. Surface area of typical aggregated particle structures after the simulation of 10 ns and areas of the silica and the alumina surfaces in each particle structure. The percent of each surface area (silica and alumina) for the particle structures is listed together with the average of the six particle structures. The particle structure number is corresponding to that labeled in Figure 3.7. 72

3.4. Volume of each aggregated structure, the cluster volume if the cluster is fitted by an ellipsoid model, and the percent solids in the cluster. 74

3.5. Experimental data for the relative particle area, porosity, and density of kaolinite clusters reported in the literature..... 77

3.6. Surface area of typical aggregated particle structures after simulation for 20 ns and the surface area of the silica and alumina surfaces. The particle structure number corresponds to the number labeled in Figure 3.11..... 83

3.7. Surface area of typical aggregated particle structures after simulation for 30 ns and the surface area of the silica and alumina surfaces. The aggregated particle structure number corresponds to the number labeled in Figure 3.12..... 83

3.8. Kaolinite suspension concentration expressed both by weight, by volume, and by the number of particles for viscosity calculation by simulation. The kaolinite density is 2.6 g/cm^3. 85

3.9. Average aggregated particle structure size for the simulation with a standard particle size distribution and mono-sized particles. The mean particle size for both cases is a particle size with 122 spheres. 85

3.10. Simulation results of the viscosity of kaolinite suspension as compared with experimental results. 88

3.11. Effect of particle shape on the viscosity for 5wt% suspensions. 90

3.12. The parameters used for simulations at different ionic strength as well as the average aggregated particle structure size (number of particles) for each ionic strength. 90

4.1. Surface charge and wettability of pyrophyllite and gibbsite in comparison with the silica face surface and alumina face surface of kaolinite. 107

4.2. Contact angle results for gibbsite surface in dodecyl amine hydrochloride solution using captive bubble method. 113

4.3. Contact angle results for pyrophyllite basal plane surface in dodecyl amine hydrochloride solution using captive bubble method. 115

ACKNOWLEDGEMENTS

First of all, I would like to express my sincere appreciation to my advisor, Professor Jan D. Miller, for all his help, guidance, and encouragement during my thesis research. He is such a knowledgeable person with great vision for the research. I enjoyed discussions with him about the research and have always been inspired by him. His mentorship is not only about guiding me to achieve good results; more importantly, I learned a way to think analytically and to solve problems efficiently. I feel so honored to be one of the luckiest persons to work with Professor Miller.

Thanks are also extended to Dr. Michael Free, Dr. Vladimir Hlady, Dr. Sanja Miskovic, and Dr. Xuming Wang for being the members of my supervisory committee and their valuable advice and comments on my dissertation. Particularly Dr. Xuming Wang provided many helpful suggestions for my dissertation research.

I would also like to thank previous students Dr. Vishal Gupta from FLSmidth and Dr. Xihui Yin from Kemira. Their previous efforts on the study of kaolinite provide a foundation for the success of this research. In addition, they gave me a lot of wonderful advice and suggestions. It has always been very helpful discussing with them.

Thanks are also extended to Dr. Chen-Luh Lin for helping me initiate the simulation of particle interactions. I would like to thank Ms. Linda Nikolova from the Electron Microscopy Core Laboratory for helping me prepare kaolinite samples. I also would like to thank Dr. Hao Du from the Chinese Academy of Sciences for encouraging me to pursue

my PhD with Professor Miller at the University of Utah. Thanks are also extended to my colleagues and friends for their support and help.

Finally, I want to thank the Department of Metallurgical Engineering at the University of Utah for providing me this wonderful opportunity. A special thanks is extended to Ms. Dorrie Spurlock for her support and help for the last 4 years.

Last, but not least, I would like to express my love and gratitude to my family and my fiancé for all their support all these years.

CHAPTER 1

INTRODUCTION

Phyllosilicate minerals, or clay minerals, are among the most important and useful industrial minerals because they have wide-ranging applications. For example, they are widely used in paper, ceramics, cosmetic products, catalyst, rubber, and polymer composites (Grim 1962; Van Olphen 1977; Murray 1991, 2000; Lagaly and Bergaya 2013). The world production of kaolin clay in 2013 was 37 Mt, of which the U.S. produced 5.95 Mt, valued at $895 million (R.L.Virta 2014). Kaolinite, as a white pigment, accounts for over 38% of the 18 Mt of pigment used for world papermaking in 2004 (Harris 2004). Of recent interest to researchers is the dispersion of some clays in polymer to form nanocomposites with improved adhesion, and lower required filler volume to achieve desired properties (Zeng et al. 2005). Economic lightweight ceramic proppants (additives for drilling fluids and products for oilwell cementing) have been produced from calcined kaolin clay and have been used for increased gas and oil production (Lemieux and Rumpf 1991).

However, clay minerals (for example kaolinite, pyrophyllite, illite, and montmorillinite), are also very common gangue minerals, and are difficult to remove during the processing of mineral resources. Examples include oil sands, potash, phosphate, bauxite, rare earth resources, and metal sulfide ores such as copper, nickel, and PGM ores

(Zhang and Bogan 1995; Liu et al. 2004; Zhong et al. 2008; Marino 2012).

In geotechnology, the hydration or dehydration of clay may result in slope instability and/or failure (Call 1992). Most of the phosphate deposits in central Florida contain about 10% clay minerals, making the recovery of the phosphate minerals extremely difficult. After phosphate recovery, the tailings which might contain 30–50% clay are discarded. It usually takes 3–5 years for sedimentation and consolidation to reach 50–60% solids, requiring a lot of land to be used for tailing disposal (Zhang and Bogan 1995). The important role clays played in tailings has drawn extensive attention in recent years. Examples of related conferences include Tailings 2014, Paste 2014, Tailings and Mine Waste Conference 2014, and International Oil Sands Tailings Conference 2014. Understanding the interactions among clay particles with/without flocculants is one of the most critical issues for the study of tailings and their disposal. In this regard, clay surface chemistry research is indispensable to establish the charging and rheological behavior of clay particles, and to improve flotation and dewatering technology. In addition, such surface chemistry information is important to understand slope stability. Finally, surface chemistry research is important to support industries which use clay minerals, including polymer composites, papermaking, cosmetics, etc.

Particular attention is given to the surface properties of kaolinite due to its widespread applications as well as its representative anisotropic surface features found in many phyllosilicate minerals. The difficulty to prepare clay particles of less than a micrometer in size for analysis of face surfaces and edge surfaces, particularly kaolinite particles, should be recognized. In this regard, a protocol for the preparation and characterization of clay particles, specifically kaolinite, is developed using ultramicrotome

and surface force measurements by Atomic Force Microscopy (AFM).

1.1 Clay Mineralogy

The definition of clay and clay minerals always differs for people from diverse backgrounds and diverse interests (e.g., geologist, engineer, colloid chemist, and ceramist) (Grim 1953; Bailey 1980; Guggenheim and Martin 1995; Schoonheydt et al. 1999). In this study, clay minerals are regarded as phyllosilicate minerals, usually with a particle size less than 2 μm. Phyllosilicate minerals basically consist of two types of sheets, namely a silica tetrahedral sheet and an alumina or magnesia octahedral sheet. Depending on the ratio of silica and alumina/magnesia sheets, phyllosilicates can be classified as bilayer phyllosilicates (1:1 type) or trilayer phyllosilicates (2:1 type) as shown in Figure 1.1 (A) and (B). The serpentine and kaolin groups belong to the bilayer phyllosilicates, where the serpentine group has the magnesium atom at the center of the octahedron, making a trioctahedral sheet or a "brucite type" sheet; the kaolin group has the aluminum atom at the center of the octahedron, making a dioctahedral sheet or a "gibbsite type" sheet. Trilayer phyllosilicates include the groups of talc, muscovite, illite, smectite, and chlorite. As a matter of fact, bilayer phyllosilicates contain more hydroxyl groups than trilayer phyllosilicates due to sharing of oxygen atoms in the octahedral sheet with an additional tetrahedral sheet.

Depending on the nature of the crystal structure, isomorphous substitution of the clay minerals can happen and cause the layer charge, which is the charge deficiency on the 2:1 layer due to substitutions in tetrahedral, octahedral, or both positions. The layer charge of the mica group can be 1 or 2. The most common mica group mineral is muscovite [$KAl_2AlSi_3O_{10}(OH)_2$], having the layer charge as 1, which is attributed to the substitution

of one fourth of the silicon atoms in the tetrahedral layer by aluminum atoms. The layer charge of illite is ~0.75, and the layer charge of smectite is 0.2–0.6 (Bergaya et al. 2011). The existence of the layer charge for the phyllosilicate layers accounts for the accommodation of interlayer cations to balance the charge (K^+, Na^+, NH_4^+, etc.). The lower the layer charge is, the easier for the interlayer cations to exchange with cations in solution (Van Olphen 1977). The amount of exchangeable cations, expressed in milliequivalents per 100 g of dry clay, is called the cation exchange capacity (CEC). Table 1.1 shows the ideal chemical composition and features of typical phyllosilicates. The interlayer of the chlorite mineral is a brucite layer or gibbsite layer, making a 2:1:1 structure, as shown in Figure 1.1 (C).

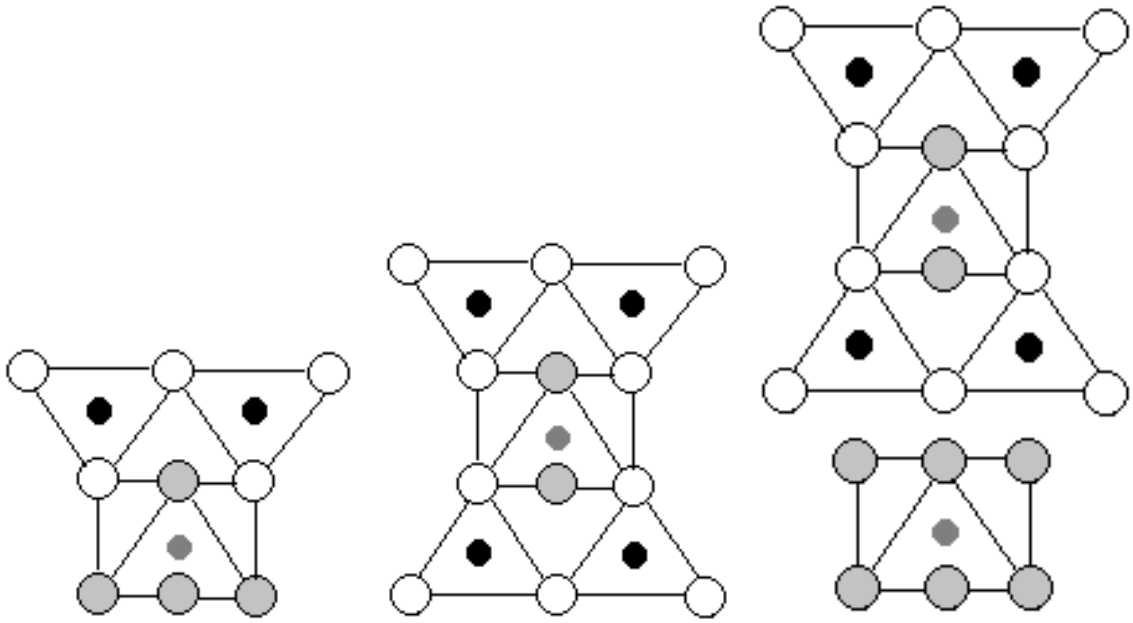

Figure 1.1. Crystal structures of bilayer phyllosilicate (A), trilayer phyllosilicate (B) and 2:1:1 phyllosilicate (C). The open circles represent oxygen atoms, the large grey circles represent hydroxyl groups, the dark circles represent silicon atoms, and the small grey circles represent aluminum or magnesium atoms.

Table 1.1. Chemical composition and features of selected phyllosilicates. R^{2+} represents divalent cation, x represents an integer number.

Mineral Type	Octahedra Type	Typical Clay Minerals	Chemical Composition
Bilayer (1:1 layer)	Dioctahedra	Kaolinite (kaolin group)	$Al_2Si_2O_5(OH)_4$
		Halloysite (kaolin group)	$Al_2Si_2O_5(OH)_4 \cdot 2H_2O$
	Trioctahedra	Antigorite (serpentine group)	$Mg_3Si_2O_5(OH)_4$
		Chrysotile (serpentine group)	$Mg_3Si_2O_5(OH)_4$
Trilayer (2:1 layer)	Dioctahedra	Pyrophyllite	$Al_2Si_4O_{10}(OH)_2$
		Muscovite (mica group)	$KAl_2AlSi_3O_{10}(OH)_2$
		Illite (interlayer deficient mica)	$K_{0.65}Al_{0.65}Al_2Si_{3.35}O_{10}(OH)_2$
		Montmorillonite (smectite group)	$(Na,K)_{0.33}(Al_{1.67}Mg_{0.33})Si_4O_{10}(OH)_2$
	Trioctahedra	Talc	$Mg_3Si_4O_{10}(OH)_2$
		Phlogopite (mica group)	$KMg_3AlSi_3O_{10}(OH)_2$
		Saponite (smectite group)	$(Na,K)_{0.33}Mg_3(Al_{0.33}Si_{3.67})O_{10}(OH)_2$
2:1:1 Type	Tioctahedra	Clinochlore (chlorite group)	$Mg_5Al_2Si_3O_{10}(OH)_8$
Fibrous Clay	Dioctahedra	Palygorskite	$MgAl_3Si_8O_{20}(OH)_3(OH_2)_4 \cdot x(R^{+2}(H_2O)_4)$
	Trioctahedra	Sepiolite	$Mg_8Si_{12}O_{30}(OH)_4(OH_2)_4(H_2O)_8$

Exceptions of phyllosilicate minerals include: 1) halloysite 2) palygorskite and sepiolite. The chemical composition of halloysite is the same as that of kaolinite except the interlayer water is present in halloysite [$Al_2Si_2O_5(OH)_4 \cdot 2H_2O$]. The mismatch between the silica tetrahedral sheet and alumina octahedral sheet results in different morphologies of halloysite, such as spheres, tubes, and plates (Joussein et al. 2005). On the other hand, palygorskite and sepiolite differ from other phyllosilicates in that they lack continuous octahedral sheets due to the periodic inversion of SiO_4 tetrahedra, forming a fibrous

structure.

1.2 Surface Features of Kaolinite

Kaolinite occurs in primary and secondary deposits, forming from the decomposition of feldspar or mica. As one of the most common and most important minerals, kaolinite is soft and usually white, with a specific gravity of 2.6 and a hardness of 2–2.5 (Mohs relative hardness scale). Kaolinite [$Al_2Si_2O_5(OH)_4$] has a 1:1 layered structure, has a low swelling capacity, and has a low cation-exchange capacity (1–15 meq/100g). Kaolinite particles consist of three surfaces, one silica tetrahedral basal plane surface, one alumina octahedral basal plane surface, and one edge surface, as shown in Figure 1.2. The spacing, distance between two repeating kaolinite bilayers, is about 0.72 nm.

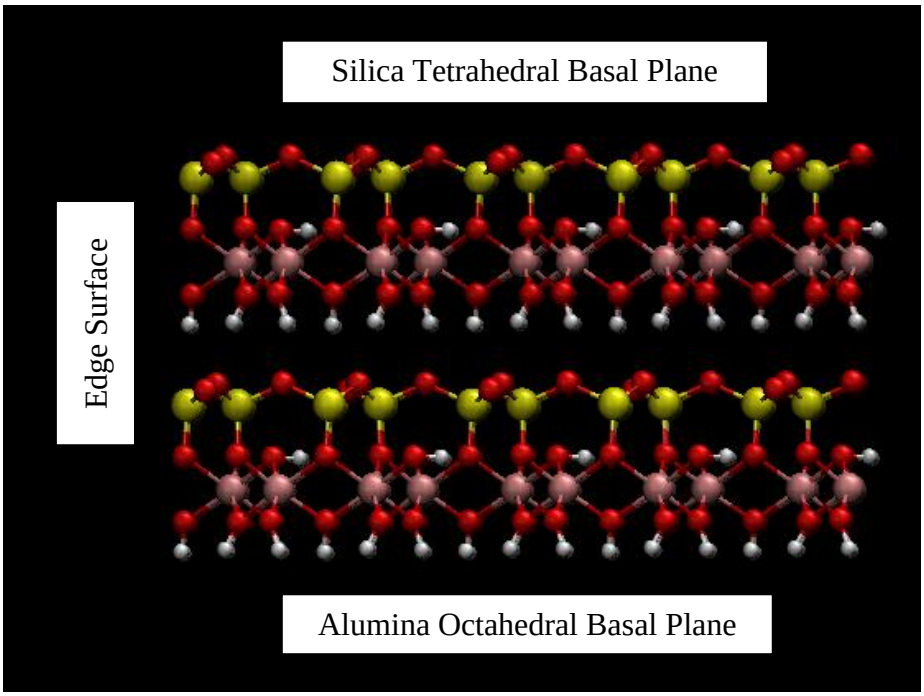

Figure 1.2. Crystal structure of kaolinite. Red: Oxygen; Yellow: Silicon; Purple: Aluminum; White: Hydrogen.

Attempts have been made to study the surface charge characteristics of kaolinite particles. The point of zero charge (PZC) of kaolinite particles measured by electrophoresis is determined to be pH 3.6 (Hu et al. 2003), or even less than pH 3 (Gupta 2011). It is also reported that the PZC of kaolinite particles shifts to higher pH with higher alumina content (Miller et al. 2007) and increasing ionic strength (Chassagne et al. 2009). In addition, the potentiometric titration technique has been used to determine the point of zero net charge (p.z.n.c.) and the point of zero net proton charge (p.z.n.p.c.) of kaolinite as pH 3.3–3.6 and pH 5.0–5.4, respectively (Schroth and Sposito 1996). Unfortunately, both techniques only provide information on the overall/average of the surface charge properties of kaolinite particles, without taking into consideration the platy shape and anisotropic charging features of kaolinite particles. In fact, the chemical composition and structure of preferred cleavage (001) face and (00$\underline{1}$) face should be different judging from the mineral structure of kaolinite: one is the silica face and the other is the alumina face. Not to mention, each surface exhibits different charging characteristics, determined by different charging mechanisms: isomorphous substitution on the basal plane and hydrolysis reactions of broken bonds on the edge surface (Bergaya et al. 2011). Therefore, it is hard to understand the meaning of the overall surface charge of kaolinite particles as might be determined by electrophoresis and potentiometric titration. With that in mind, it is necessary to determine the charge of the face surfaces and edge surfaces of kaolinite individually.

However, the difficulty of handling small particles with an average particle size of only ~500 nm has hindered the adventure of unravelling the charge of each of the kaolinite surfaces. Another challenge in the research is to identify each of the three different kaolinite surfaces. Until recently, research progress on the surface characterization and wettability

of the basal planes of kaolinite has been made as reported in the literature (Gupta and Miller 2010; Yin et al. 2012). Gupta and Miller measured the surface charge of both kaolinite basal plane surfaces by ordering individual particles on a substrate; the results showed that the isoelectric point (IEP) of the alumina face of kaolinite particles is between pH 6–8, and the IEP of the silica face is below pH 4 (Gupta and Miller 2010). In the meantime, crystal lattice images of both basal planes taken by Atomic Force Microscopy (AFM) have matched the ideal crystal structure of each basal plane, and have confirmed that the surfaces prepared are the silica face and alumina face, respectively. Furthermore, Yin et al. studied the wettability of the two basal planes of kaolinite particles, showing the silica face of kaolinite particles is more hydrophobic than the alumina face, which is verified by the results of molecular dynamic simulation as well (Yin et al. 2012).

An edge surface is commonly exposed for clay mineral particles. However, the size of the edge surface for kaolinite particles is only 10–50 nm. The huge challenge of ordering and characterizing kaolinite edge surfaces is self-evident. Researchers have reported that the ultramicrotome equipment is able to cut molecularly smooth clay edge surfaces for large particles of mica, talc, and chlorite, and the properties of these edge surfaces have been revealed by AFM (Yan et al. 2011; Yin et al. 2013). Nevertheless, success was achieved only for those clay minerals of large size (>5 mm) and well-defined crystallinity. Such samples are easily sealed in epoxy resin for cutting and preparation of the edge surface using the ultramicrotome. For small particles like kaolinite, reliable results for the surface properties of kaolinite edge surface have not been reported.

Despite the difficulty to study the edge surface of kaolinite, many researchers expressed their expectations for the surface charge of kaolinite edge surfaces. Van Olphen

believed that the entire edge surface may carry a positive double layer (Van Olphen 1977). His argument was based on Thiessen's electron micrograph of a mixture of kaolinite particles (Thiessen 1942). The conclusion is very ambiguous when the positively charged alumina basal plane surface of kaolinite is considered and in the absence of a detailed description of the experimental procedure. The PZC of the kaolinite edge surface has been reported to vary from pH 4.5 to pH 7.5 (Flegmann et al. 1969; Rand and Melton 1975; Kretzschmar et al. 1998; Gupta et al. 2011). It is expected that the variation is found because of different measurement techniques as well as the assumptions. Rand and Melton anticipated the IEP of the kaolinite edge surface to be at pH 7.5, where the transition point for the Bingham yield value is formed for kaolinite suspensions (Rand and Melton 1975). But those results are concluded from the rheological behavior or adsorption behavior of kaolinite particles, with a misconstrued hypothesis that both basal planes are negatively charged (Flegmann et al. 1969; Rand and Melton 1975; Kretzschmar et al. 1998). Gupta et al. roughly estimated the PZC of the kaolinite edge surface at ~pH 4.5 by subtracting the surface charge of each face from the total surface charge measured by the titration method (Gupta et al. 2011). However, it has to be mentioned that indirect estimation of the surface charge can vary over a broad range and sometimes can even be very misleading. A reliable experimental measurement of the properties of the kaolinite edge surface has to be accomplished.

1.3 Kaolinite Particle Aggregation

The clay colloidal stability relies on the modes of particle association or aggregation in suspension. For kaolinite particles, three different surfaces are exposed to the environment, resulting in the following possible particle association: face to face, edge

to face, and edge to edge. The modes of the particle interaction can be governed by van der Waals force, electrical double layer force, hydrophobic force, hydration force, etc. Expectations of the kaolinite particle interaction have been discussed based on previous knowledge of the surface properties of kaolinite particles. Typically, a card-house structure with edge to face interaction and/or edge to edge interaction is anticipated (Van Olphen 1977). The fabric of kaolinite particles in suspension has been studied based on the rheological behavior (Palomino and Santamarina 2005). Several researchers have tried to verify the structure of kaolinite particle aggregates in suspension by imaging using a freeze-drying technique and cryo SEM (O'Brien 1971; Zbik et al. 2008; Gupta et al. 2011). As expected, the card-house structure has been observed and the particle aggregation is significantly influenced by pH, but concerns exist if the particle aggregation structure will change during drying or freezing.

1.4 Flotation Chemistry of Clay Minerals

Clay minerals widely exist as gangue minerals in potash, bauxite, phosphate, and iron ores as well as oil sands. The particle size of clay minerals is usually below 2 microns, which is too fine for the flotation process. It is believed that the fine particles in flotation differ from the coarse particles in physico-chemical properties (Fuerstenau 1980). The small mass and momentum cause clay particles to report to the froth either by entrainment during froth flotation or by mechanical entrapment within the hydrophobic particles being floated. Besides, excessive consumption of the collector for the flotation of clay or fine particles is formed due to the large specific surface area of such fine particles.

Froth flotation is considered as one of the most efficient technologies for the removal of impurities from kaolin or removing kaolinite from other valuable minerals

(Willis et al. 1999). Yoon and Hilderbrand successfully used hydroxamate collectors to purify kaolin clay by flotation of impurities from kaolinite (Hilderbrand and Yoon 1986). In the meantime, continuous efforts on the removal of kaolinite for the beneficiation of other valuable minerals have been made using cationic collectors (Bittencourt et al. 1990; Hu et al. 2005; Zhong et al. 2008; Ma et al. 2009; Xia et al. 2009; Yu et al. 2010; Marino 2012). One of the first, if not the first, attempts at removing kaolinite from bauxite by flotation was reported by Bittencourt et al., using a quaternary ammonium salt collector at pH 6 and in this way a high purity gibbsite (97.4%) concentrate was produced (Bittencourt et al. 1990). Hu et al. have used dodecyl amine collector for reverse flotation of kaolinite from bauxite and reached the flotation recovery ~62% at low pH (Hu et al. 2005). Ma et al. studied the effect of amine collector type, pH, and ionic strength on the flotation behavior of kaolinite (Ma et al. 2009). Marino et al. have compared the direct bauxite flotation with the reverse flotation of kaolinite, and achieved higher alumina grade with direct flotation, but higher alumina recovery with reverse flotation (Marino 2012). However, a detailed analysis of the kaolinite flotation mechanism has not been reported since the surface chemistry of kaolinite has only recently been partially established.

1.5 Research Objectives

Thesis research objectives include the following major goals.

1) Determine the charge of selected surfaces for layered silicate particles, particularly the charge of the kaolinite edge surface, which has not been reported, based on surface force measurements using Atomic Force Microscopy (AFM).
2) Based on surface charge information and DLVO theory, describe the aggregation of kaolinite particles into clusters by Brownian dynamics simulation technique and

verify the simulation results by experiment using PCS, and image analysis with SEM and X-ray CT.

3) Explain the reverse amine flotation of kaolinite from bauxite ore based on surface chemistry experiments with model surfaces and data reported in the literature.

1.6 Dissertation Organization

After the Introduction presented in Chapter 1, a new protocol developed for the preparation of kaolinite edge surfaces for examination by Atomic Force Microscopy (AFM) is presented in Chapter 2. The surface charge of kaolinite edge surfaces is then calculated from AFM surface force measurements. The wettability of kaolinite edge surfaces is revealed by Molecular Dynamics Simulation (MDS). Moreover, a discussion on the surface properties of the kaolinite edge surface is presented in comparison to those of other clay minerals. Results from the effect of ionic strength on charging of the silica face of selected phyllosilicates, including muscovite, talc, and kaolinite, are reported. The influence of isomorphous substitution degree on the surface charge of phyllosilicates is revealed. In addition, the effect of ionic strength on the charging of each kaolinite surface is presented.

Chapter 3 discusses kaolinite particle–particle interaction using Brownian dynamics simulation technique. A coarse-grained model, built for kaolinite particles, is presented. Cluster formation is analyzed as a function of pH, concentration, simulation time, and ionic strength. The cluster formation is expected to account for rheological properties. In this regard, the kaolinite suspension viscosity is simulated and compared with experimental results. Finally experimental validations of the cluster structure are employed using both SEM and X-ray CT.

Chapter 4 analyzes the reverse flotation of kaolinite from bauxite with dodecyl

amine collector. The basal plane surfaces of gibbsite and pyrophyllite are used as model surfaces in this research to represent the alumina and silica basal plane surfaces of kaolinite, respectively. Qualifications of the model surfaces are examined in terms of the chemical structure, the surface charge, and the wettability. The hydrophobicity of the two kaolinite basal plane surfaces with the adsorption of the dodecyl amine collector is examined as a function of pH and collector dosage.

Chapter 5 summarizes the findings of this dissertation and provides discussion for future research.

CHAPTER 2

SURFACE FORCES AT KAOLINITE AND OTHER PHYLLOSILICATE SURFACES

2.1 Introduction

The surface properties, especially the surface charge and hydrophobicity of kaolinite particles, play an important role in their flotation chemistry and sedimentation processes. The anisotropic features of kaolinite particles make the behavior of kaolinite particles more difficult to predict, since each particle is expected to have three different surfaces—the silica tetrahedral face surface, the alumina octahedral face surface, and the edge surface. It is desired to determine the properties of each kaolinite surface. Gupta and Miller measured the surface charges of both kaolinite basal plane surfaces using Atomic Force Microscopy (AFM), showing that the isoelectric point (IEP) of the alumina face surface is between pH 6–8, and the IEP of the silica face surface is below pH 4 (Gupta and Miller 2010). Furthermore, Yin et al. studied the wettability of the two basal planes of kaolinite particles by measuring the hydrophobic force between the sample surface and a hydrophobic diamond-like-carbon AFM tip, showing that the silica face of kaolinite particles is more hydrophobic than the alumina face (Yin et al. 2012).

However, success on the direct characterization of the properties of the kaolinite edge surface has not been accomplished due to the absence of an appropriate sample

preparation method for the kaolinite edge surface, which has a thickness of 10–50 nm. The PZC of the kaolinite edge surface has been estimated to be between pH 4.5 to pH 7.5 (Rand and Melton 1975; Kretzschmar et al. 1998; Gupta et al. 2011). Nevertheless, those expectations are based on a rough estimation or the assumption that both basal plane surfaces carry the same charge, which has been proved to be not true. A reliable experimental measurement of the properties of the kaolinite edge surface has yet to be accomplished.

Recently, Yan et al. and Yin et al. successfully prepared molecularly smooth clay edge surfaces for large particles of mica, talc, and chlorite using an ultramicrotome, and the properties of these edge surfaces have been revealed by AFM (Yan et al. 2011; Yin et al. 2013). However, for small particles like kaolinite, reliable results for the charge of the edge surfaces have not been reported.

Clays, including kaolinite, are very common gangue minerals in the processing of mineral and energy resources, e.g., potash, phosphate, bauxite, rare earth resources, and metal sulfide ores (copper, nickel, and PGM), coal, and oil sands (Brogoitti 1974; Shang and Lo 1997; Liu et al. 2004; Zhong et al. 2008; Marino 2012). Although considerable research has been reported on the surface charge/particle interaction of clay minerals, as a function of pH, very limited research has been reported on the behavior of the clay minerals as a function of ionic strength such as might be expected in salty water (Chang and Sposito 1996; Palomino and Santamarina 2005).

The availability of fresh water resources is of global concern, especially in dry, remote areas (e.g., southern Peru and northern Chile). Industries with large water consumption such as the mining industry are in a difficult position. The use of saline water

or seawater in the mineral processing and mining industries has gained more and more attention recently. Of course, the reuse of process water with higher ionic strength is one way to conserve fresh water resources. Already, mineral processing plants using salty water have been in operation (Drelich and Miller 2012; Peng et al. 2012). However, many problems have been reported because of the high ionic strength of such salty water (Castro 2012; Laskowski et al. 2013). Studies have shown that high ionic strength promotes particle aggregation and flocculation phenomenon (Van Olphen 1977; Pashley and Karaman 2005).

The surface charge of clay particles results in formation of their electrical double layer in aqueous suspensions. The DLVO theory, composed of van der Waals attraction and electrostatic interactions, most commonly accounts for particle interactions and can account for collector or specific adsorption of solutes in some cases (Yavuz et al. 2003; Ma et al. 2009; Gupta et al. 2011). The effect of electrolyte on the surface charge of the particles depends on the type of electrical double layer. If the surface potential of the particles is determined by the aqueous phase concentration of potential-determining ions, the magnitude of the surface potential is not supposed to be affected by the presence of an indifferent electrolyte, but the surface charge density will vary with solution composition. In contrast, if the surface charge of the particle is determined by lattice substitution or crystal imperfections, the surface charge density is expected to be independent of ionic strength (Van Olphen 1977; Kosmulski 2001). However, the constant surface potential and constant surface charge models are not always appropriate, depending on the degree of dissociation ionizable surface sites (Tadros and Lyklema 1968; Roy and Sengupta 1988; Thomas et al. 1989; de Almeida Gomes and Boodts 1999; Israelachvili 2011).

Atomic Force Microscopy has been widely applied in imaging and measuring the

surface forces between the sharp tip of a cantilever and selected surfaces of interest (Assemi et al. 2008; Gupta and Miller 2010; Yan et al. 2011; Yin et al. 2012; Yin et al. 2013) Based on the geometry of AFM tips, the Derjaguin–Landau–Verwey–Overbeek (DLVO) theory, including the electrostatic force and van der Waals force, has been established (Drelich et al. 2007). The advantage of AFM force measurements for surface properties of clay minerals is that AFM force measurements are able to acquire information for a particular surface, even for a particular point, unlike electrophoresis and titration techniques which can only measure the integral properties of particle surfaces.

In this chapter, a new protocol to prepare kaolinite edge surfaces of 10–50 nm in thickness will be described, and the surface charge of the kaolinite edge surface will be measured by AFM. In addition, the effect of ionic strength on the properties of selected phyllosilicates will be discussed.

2.2 Materials and Methods

2.2.1 Materials

A clean kaolinite sample was obtained from the St. Austell area in Cornwall, UK. Characteristic data for this sample and its preparation can be found in the literature (Gupta 2011). No further cleaning of the kaolinite sample was performed. The kaolinite suspension was prepared in high purity Milli-Q water (Millipore Inc.). Muscovite mica sheets were purchased from SPI Supplies (West Chester, PA). High quality talc samples were obtained from the College of Mines and Earth Science collection, at the University of Utah. The resistivity of the DI water was 18 MΩ-cm in all experiments. To calibrate AFM tips, fresh muscovite mica sheets purchased from SPI Supplies (West Chester, PA) and fused silica wafer were used. Potassium chloride was used as the background electrolyte and adjusted

to the desired value for surface force measurements. The pH was adjusted to its desired value using 0.1 M and 0.01 M HCl, or 0.1 M and 0.01 M KOH solutions. All chemicals used were of ACS grade.

The silica wafer was rinsed in RCA SC-1 cleaning solution composed of 5 vol H_2O, 1 vol H_2O_2, 1 vol NH_4OH at 80 ℃ for 20 minutes, followed by rinsing with DI water and drying with ultra high purity N_2 gas. In this way, contamination with any organic material was expected to be removed (Nalaskowski et al. 2003; Gupta and Miller 2010).

2.2.2 Sample Preparation

To prepare kaolinite edge surfaces, a 6% kaolinite suspension was prepared and the pH was adjusted to about 9 using the KOH solution. Rapid magnetic stirring for 1 hour followed by sonication for 30 minutes was applied to make sure that the particles were completely dispersed. The suspension was centrifuged at 3000 rpm for 30 seconds, and the supernatant decanted. The supernatant suspension was then sonicated for another 30 minutes and centrifuged at 3000 rpm for 1.5 minutes. The resulting sediment was treated again by centrifugation for 30 seconds and 1.5 minutes to remove both residual fine and coarse kaolinite particles. The final dilute kaolinite suspension was heated and concentrated to about 7wt%. The average size of the resulting kaolinite particles was estimated to be 500–700 nm. The concentrated kaolinite suspension was pipetted onto a hardened epoxy resin (Electron Microscopy Sciences, Hatfield, PA), thinly spread over the resin surface, and immediately transferred to a hot plate (T~120 ℃). After the kaolinite film was dry, another epoxy resin layer was carefully put on the top of the dried kaolinite particles. The resin was baked to cure the sample, forming an epoxy resin sandwich structure with layered kaolinite particles in the center of the epoxy resin sandwich. The

epoxy block was trimmed by a razor blade under an optical microscope to make the kaolinite basal surfaces as perpendicular as possible to the cutting edge of the ultramicrotome knife. The block was then mounted on the ultramicrotome (EM UC6, Leica Microsystems Inc.) for cutting. After cutting a smooth surface, the block was glued on the magnetic disk with epoxy (EpoxyBond 110^{TM}, Allied High Tech Products, Inc., CA). Before being used in the AFM study, the block surface was cleaned with Milli-Q water and ethanol, and dried with ultra high purity nitrogen gas.

In the case of basal plane experiments for fresh muscovite and talc basal plane surfaces, preparation was accomplished by peeling off several layers with adhesive tape. The alumina and silica basal plane surfaces of kaolinite were prepared following procedures described in the literature (Gupta and Miller 2010). To identify the influence of ionic strength on the properties of selected phyllosilicates, potassium chloride solutions at concentrations of 1 mM, 10 mM, 50 mM, and 100 mM were used as the background electrolyte for surface force measurements. All experiments for the study of ionic strength were conducted at pH 5.6.

2.2.3 Atomic Force Microscopy

A picoforce AFM with Nanoscope V controller (Veeco Instruments Inc., Santa Barbara, CA) was used with a PF-type scanner designed for picoforce measurements. Sharp triangular silicon tips on a silicon nitride cantilever (SNL-10, Bruker AFM Probes, CA) with spring constants varying from 0.25 N/m to 0.33 N/m were used for AFM imaging and force measurements for kaolinite edge surfaces. Sharp triangular silicon nitride tips (NP-S10, Bruker AFM Probes, CA) with spring constants varying from 0.17 N/m to 0.25 N/m were used for AFM imaging and surface force measurements at basal plane surfaces

of phyllosilicates. A more accurate spring constant was determined after the force measurements had been completed, using the thermal tuning function provided in the Nanoscope V 7.20 software.

The force measurements of kaolinite edge surfaces were performed in 5 mM KCl solution at pH 4, 6, and 9 using the fluid cell provided in the picoforce AFM. First, an image of the surface with kaolinite particles was collected, and then using the point and shoot feature of the Nanoscope software, the surface forces of the kaolinite edge surfaces were measured. The contact mode of operation was used to obtain images of the surface. Force measurements were taken at a minimum of 10 locations. At each location, at least 20 force curves were taken. Five fresh-cut surfaces were used in this study. All the force measurements were performed at a scan rate of 1 Hz and captured at a resolution of 512 points/measurement. The raw force files were analyzed with SPIP software (Image Metrology, Lyngby, Denmark), which converts the deflection–distance curves to force–distance curves. Baseline correction and hysteresis correction were involved in preparation of the force curves.

Before the force measurements on the kaolinite basal plane surfaces, an image was taken, and then the point and shoot feature of the nanoscope software was used for the force measurements at the basal surfaces of kaolinite particles. However, the muscovite and talc basal plane surfaces are atomically smooth; therefore, the point and shoot feature is not necessary. Force measurements were taken at 5–10 locations. At each location, at least 20 force curves were taken. All the force measurements were performed at a scan rate of 1 Hz and captured at a resolution of 512 points/measurement. The force measurements were performed at pH 5.6 in KCl solutions of 1 mM, 10 mM, 50 mM, and 100 mM, using the

fluid cell provided with the picoforce AFM.

2.2.4 Tip Evaluation

Considering the previous estimation on the thickness of kaolinite particles reported to be about 11.2 nm, a very sharp AFM tip was carefully selected (Gupta 2011). The silicon tip (SNL-10, Bruker AFM Probes, CA) has a normal tip radius of 2 nm, as claimed by the manufacturer. The morphology of the tip was examined with a Hitachi S-4800 high resolution field emission scanning electron microscope. A pyramid-like sharp tip was found as shown in Figure 2.1. The tip quality and radius were evaluated with the Nanoscope software (Veeco Inc., Santa Barbara, CA) by reverse imaging of a sharp test grating TGT1 (NT-MDT Co. Moscow, Russia). The tip evaluation was performed after force measurements, making sure the tip was not worn or damaged. The tip radius of the silicon tips (SNL-10) used for the force measurements at the edge surfaces of kaolinite particles is between 2–4 nm, while the radius of the silicon nitride tips (NP-S10) used for the force measurements at the basal surfaces of phyllosilicates is between 15–25 nm.

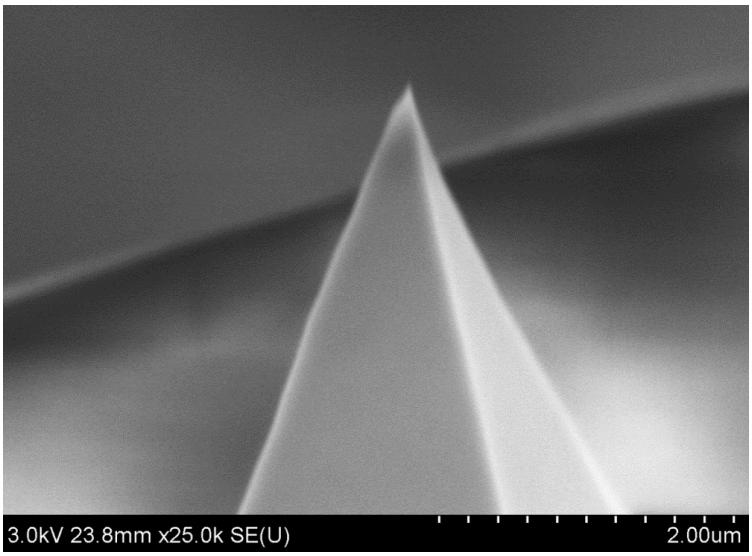

Figure 2.1. Typical Hitachi SEM image of a silicon AFM tip used in this study.

2.2.5 Theoretical Model

The geometry of the silicon AFM tip can be approximated as being conical in shape with a spherical cap at its apex. The geometry of the system and the parameters used for analysis are shown in Figure 2.2. The symbols α and β are the geometrical angles for the spherical cap at the tip end and for the conical tip, with $\alpha+\beta = 90°$. D is the distance from the end of the tip to the substrate, L is the distance between a differential surface section of the tip and the substrate, r is the radius of the circle of the tip at a given vertical position, and R is the radius of the spherical cap at the tip end (Drelich et al. 2007).

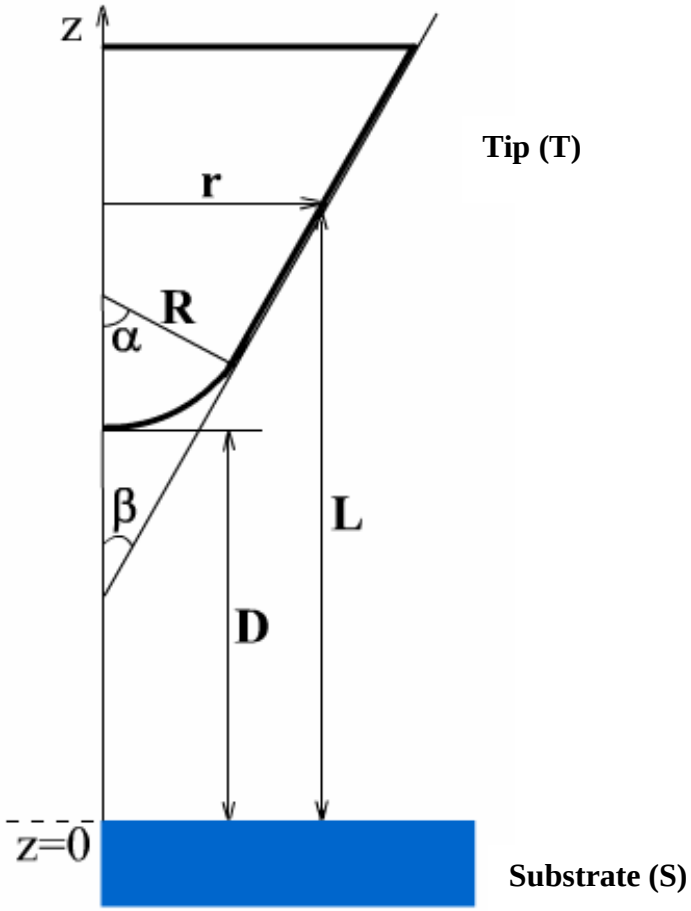

Figure 2.2. Geometry of the AFM tip and parameters used for theoretical DLVO calculations.

The DLVO theoretical model for the conical tip-flat substrate system is derived and discussed in the literature (Drelich et al. 2007). Only the final equations are given below. The total DLVO force

$$F^{DLVO} = F^{vdw} + F^{edl} \tag{2-1}$$

van der Waals forces

$$F^{vdw} = \frac{A}{6}\left[\frac{(R+D)-2L_1}{L_1^2} - \frac{R-D}{D^2}\right] - \frac{A}{3\tan^2\alpha}\left(\frac{1.0}{L_1} + \frac{(R\sin\alpha\tan\alpha - D - R(1-\cos\alpha)}{L_1^2}\right) \tag{2-2}$$

Electrostatic double layer force of constant surface charge density:

$$F^{edl} = \frac{4\pi}{\varepsilon_0\varepsilon\kappa^2}\sigma_T\sigma_S(\alpha_0 e^{-\kappa D} - \alpha_1 e^{-\kappa L_1}) + \frac{2\pi}{\varepsilon_0\varepsilon\kappa^2}(\sigma_T^2 + \sigma_S^2)(\alpha_2 e^{-2\kappa D} - \alpha_3 e^{-2\kappa L_2}) + \frac{4\pi}{\varepsilon_0\varepsilon\kappa^2\tan\alpha}\left[b_1\sigma_T\sigma_S e^{-\kappa L_1} + b_2\frac{(\sigma_T^2+\sigma_S^2)}{2}e^{-2\kappa L_1}\right] \tag{2-3}$$

Electrostatic double layer force of constant surface potential:

$$F^{edl} = 4\pi\varepsilon_0\varepsilon\psi_T\psi_S(\alpha_0 e^{-\kappa D} - \alpha_1 e^{-\kappa L_1}) - 2\pi\varepsilon_0\varepsilon(\psi_T^2 + \psi_S^2)(\alpha_2 e^{-2\kappa D} - \alpha_3 e^{-2\kappa L_2}) + \frac{4\pi\varepsilon_0\varepsilon\kappa}{\tan\alpha}\left[b_1\psi_T\psi_S e^{-\kappa L_1} - b_2\frac{(\psi_T^2+\psi_S^2)}{2}e^{-2\kappa L_1}\right] \tag{2-4}$$

Where:

$$L_1 = D + R(1-\cos\alpha),\ \alpha_0 = \kappa R - 1,\ \alpha_1 = \kappa R\cos\alpha - 1,\ \alpha_2 = \alpha_0 + 0.5,\ and\quad \alpha_3 = \alpha_1 + 0.5 \tag{2-5}$$

$$b_1 = R\sin\alpha - \frac{D + R(1-\cos\alpha)}{\tan\alpha} + \frac{1}{\tan\alpha}(L_1 + \frac{1}{\kappa}) \tag{2-6}$$

$$b_2 = R\sin\alpha - \frac{D + R(1-\cos\alpha)}{\tan\alpha} + \frac{1}{\tan\alpha}(L_1 + \frac{1}{2\kappa}) \tag{2-7}$$

Here subscripts S and T refer to the substrate and the tip, respectively. ε is the dielectric constant of the solution in this system, ε_0 is the permittivity of vacuum, κ^{-1} is the Debye length, ψ is the surface potential, and A is the combined Hamaker constant of the tip-solution-substrate system ($A_{water} = 3.7 \times 10^{-20}$ J, $A_{silicon\text{-}nitride} = 1.62 \times 10^{-19}$ J, $A_{silica} = 6.5 \times 10^{-20}$ J, $A_{mica} = 7.0 \times 10^{-20}$ J, $A_{talc} = 1.93 \times 10^{-19}$ J, $A_{kaolinite} = 6.8 \times 10^{-20}$ J, $A_{kaolinite\ edge} = 1.20 \times 10^{-19}$ J) (Seemann et al. 2001; Gupta and Miller 2010; Gupta et al. 2011; Yan et al. 2011).

The surface potential ψ is linked with the surface charge density σ by the following Grahame equation (Masliyah and Bhattacharjee 2006):

$$\sigma = \sqrt{8c_0 \varepsilon \varepsilon_0 k_B T} \sinh\left(\frac{e\psi}{2k_B T}\right) \tag{2-8}$$

Where c_0 is the ionic concentration at the surface, k_B is the Boltzmann constant, T is the absolute temperature, and e is the electronic charge.

2.2.6 Molecular Dynamics Simulation

Amber 12 was used for the Molecular Dynamics Simulation (MDS) study of the wettability of the kaolinite edge surface. A cubic cell of (100 Å × 36 Å × 21 Å) in size containing three layers of kaolinite surfaces and 1215 water molecules was used. The crystal structure of kaolinite was created following the lattice parameters provided by American Mineralogist Crystal Structure Database (Bish 1993). The CLAYFF force field was used for the kaolinite crystal and the simple point charge (SPC) model was applied for water molecules in the simulation system (Berendsen et al. 1981; Cygan et al. 2004). The intermolecular potential parameters are presented in Table 2.1.

Table 2.1. Intermolecular potential parameters for kaolinite/water interaction (Berendsen et al. 1981; Cygan et al. 2004).

Species	Charge [e]	ε [Kcal/mol]	σ [Å]
Silicon	2.10	1.84×10^{-6}	3.706
Bridging oxygen	-1.05	0.1554	3.165
Hydroxyl oxygen	-0.95	0.1554	3.165
Hydroxyl hydrogen	0.42	0	0
Octahedral oxygen	-1.05	0.1554	3.165
Aluminum	1.58	1.33×10^{-6}	4.794
Water hydrogen	0.41	0	0
Water oxygen	-0.82	0.1554	3.169

The pair potential force field used in this study is a combination of Lennard–Jones and Coulomb electrostatic interactions, and expressed as follows.

$$U_{pair} = \sum_i \sum_j \left(4\varepsilon \left[\left(\frac{\sigma_{ij}}{r_{ij}} \right)^{12} - \left(\frac{\sigma_{ij}}{r_{ij}} \right)^{6} \right] + \frac{q_i q_j}{r_{ij}} \right) \tag{2-9}$$

Where ε is the energy parameter, σ is the size parameter, q is the charge, and r_{ij} is the distance between species i and j. Lorentz–Berthelot mixing rules have been applied to calculate the potential parameters of pairs:

$$\varepsilon_{ij} = \sqrt{\varepsilon_i \varepsilon_j} \tag{2-10}$$

$$\sigma_{ij} = \frac{\sigma_i + \sigma_j}{2} \tag{2-11}$$

The MD simulations were performed using periodic boundary condition in all three dimensions. Following the procedures reported in the literature, the kaolinite crystal was initially simulated as a NPT assembly with the pressure fixed at 0.1 Mpa and the temperature fixed at 298 K (Wang et al. 2004; Du and Miller 2007; Yin 2012). After adding

SPC water molecules into the system, the simulation was run under NVT assembly using Nose–Hoover thermostat (Melchionna et al. 1993; Martyna et al. 1994). The Ewald summation has been used for computing electrostatic interactions. The Leap–Frog method with a time step of 1 fs has been applied for integrating the particle motion. A total of 500 ps was run for the equilibration of the system, and another 1 ns was applied for the simulation.

2.2.7 Cluster Size Measurements Using PCS

The cluster size of kaolinite particles in suspension at the desired ionic strength was measured by photon correlation spectroscopy (PCS). The scattered light from the particles by their Brownian motion is collected at a scattering angle of 90 °by an optical fiber, and detected by a photo-electric detector. Kaolinite suspensions (0.05wt%) at pH 5.6 were prepared in 1 mM KCl, 10 mM KCl, 50 mM KCl, 100 mM KCl, 500 mM KCl, and 1000 mM KCl solutions and each suspension was sonicated for 30 minutes. Another 30 minutes was allowed to stabilize the suspension. A small amount of kaolinite suspension at the desired ionic strength was taken to the cuvette for PCS analysis. Each experiment was replicated 3 times and the average cluster size was obtained.

2.3 Results and Discussion

2.3.1 Properties of Kaolinite Edge Surfaces

2.3.1.1 Images of Kaolinite Surfaces

SEM images were taken after the kaolinite film was spread on the resin surface, as shown in Figure 2.3. Note both the resin and kaolinite particles are very nonconductive, which causes a charging issue during SEM imaging. Since the sputtering of carbon or gold

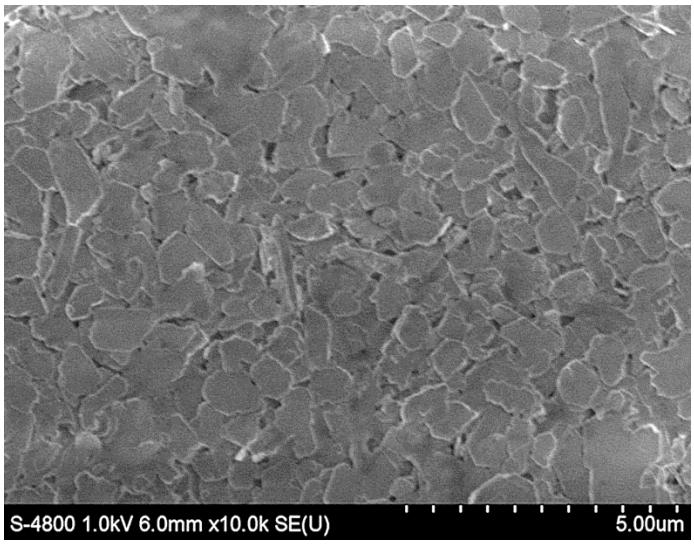

Figure 2.3. Typical Hatachi SEM image of oriented, layered kaolinite particles on the resin surface.

may destroy the surface morphology of kaolinite particles, this procedure was not performed. Most of the kaolinite particles are laying on the resin surface with the basal planes facing up; very few particles have exposed edge surfaces on the resin surface. This helps to confirm that most of the kaolinite edge surfaces will be exposed after the ultramicrotome cut of the resin sandwich. A typical AFM image of oriented kaolinite edge surfaces is shown in Figure 2.4. The root-mean-square roughness of the AFM image is 8.75 nm. Note the roughness was coming from the particles, not the diamond blade, since the resin section is extremely smooth. The very high aspect ratio of the kaolinite edge surface is shown in Figure 2.4, which is completely different from the basal plane surfaces of the kaolinite particles shown in Figure 2.3. It is evident that the edge surfaces of kaolinite particles have been prepared. The thickness of the kaolinite particles is 38.3 nm $\pm$11.7 nm, which is slightly thicker than that reported in the literature (Gupta 2011). This is probably due to the removal of kaolinite particles of small size by centrifugation during sample preparation.

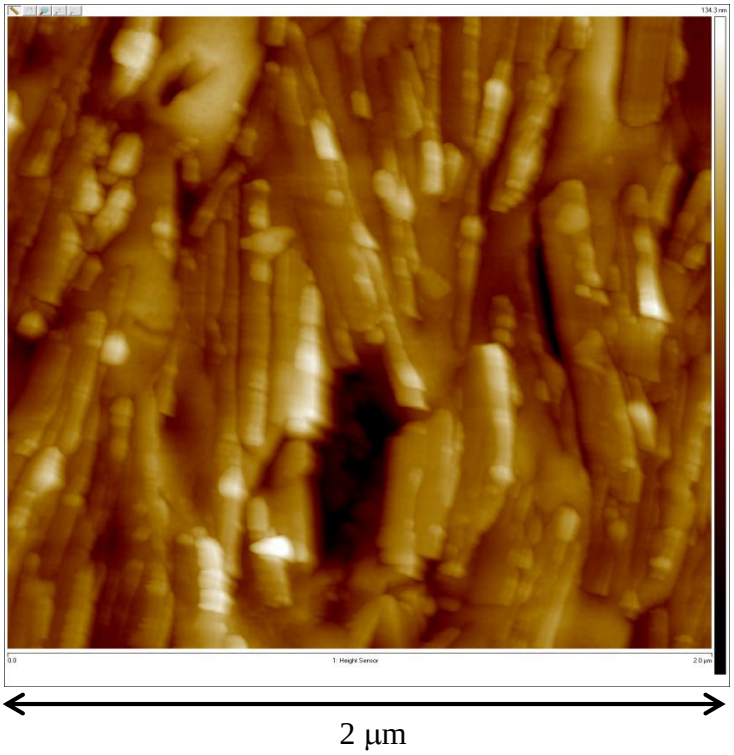

Figure 2.4. Typical AFM image of kaolinite edge surfaces.

2.3.1.2 AFM Tip Characterization Using Muscovite Surfaces

Before examination of kaolinite edge surfaces, it is important to first determine the surface charge and surface potential of the AFM tip. The surface potential values of muscovite have been widely reported by several techniques (Scales et al. 1990; Zembala and Adamczyk 1999; Yan et al. 2011). Therefore, the basal plane surface of muscovite was used to determine the surface charge of the AFM tip at various pH values. Note here we used 5 mM KCl solutions instead of 1 mM KCl solutions, the results of which are reported in the literature (Nalaskowski et al. 2007; Gupta and Miller 2010; Yan et al. 2011; Yin et al. 2013). An ionic strength of 5 mM KCl was selected because the interaction force between the AFM tip and the kaolinite surface is too small at pH 4, probably because the surface charge density at either the AFM tip or the kaolinite surface is too small at pH 4 and an ionic strength of 1 mM KCl. However, at higher ionic strength, although the double

layer is compressed, the magnitude of the surface charge increased in the absence of strongly adsorbed species (Kosmulski 2001). Before each experiment, a freshly cleaved muscovite mica basal plane was acquired by using adhesive tape to peel off several mica layers. Typical force curves of the AFM tip interacting with the mica surface are shown in Figure 2.5. The experimental force measurement data were found to fit very well with DLVO theoretical force curves, particularly for separation distances greater than 3–4 nm. This discrepancy at very short separation distances is probably caused by non-DLVO forces, which are not considered in the DLVO theoretical fit. According to the literature (Nishimura et al. 1992; Yan et al. 2011), the muscovite basal plane should be negatively charged at all pH values studied due to isomorphous substitution, which indicates the AFM tip is negatively charged at pH 4 in 5 mM KCl solution. The negative double layer on the surface of the silicon tip at pH 4 is probably due to surface oxidation of the silicon tip, which forms a silica layer (Siddiqui et al. 2011).

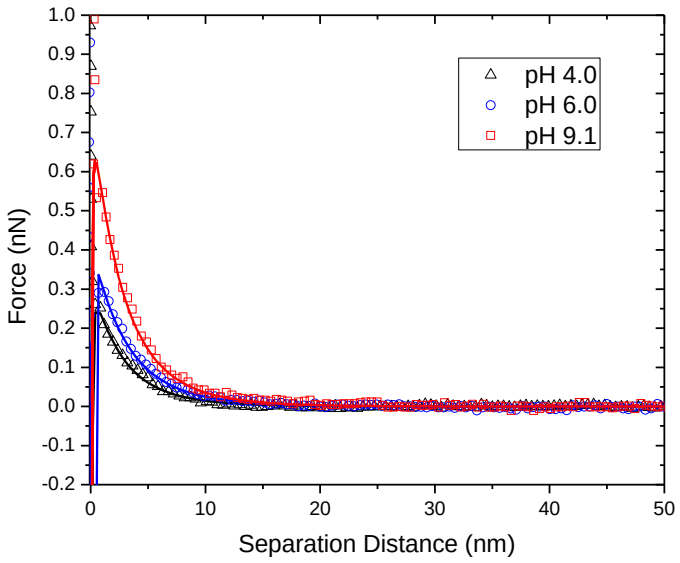

Figure 2.5. Interaction forces measured between a silicon tip and muscovite basal plane surfaces in 5 mM KCl solutions at pH 4.0, 6.0, and 9.1. Symbols correspond to experimental data. The solid lines represent the DLVO theoretical fit.

2.3.1.3 Interaction Forces between AFM Tip and Kaolinite Edge Surfaces

Typical force curves between the AFM tip and kaolinite edge surfaces are shown in Figure 2.6. For all three pH values studied, repulsive interaction between the AFM tip and kaolinite edge surfaces is demonstrated. In addition, the magnitude of the electrostatic repulsive force increases gradually with increasing pH values. We have confidence that forces were measured at the kaolinite edge surface because forces measured at a resin surface are very weak and distinctly different from forces at the kaolinite edge surface. As discussed previously, the surface charge of the AFM tip is negative at the pH values studied. Unexpectedly, the point of zero charge (PZC) of the kaolinite edge surface is below pH 4.

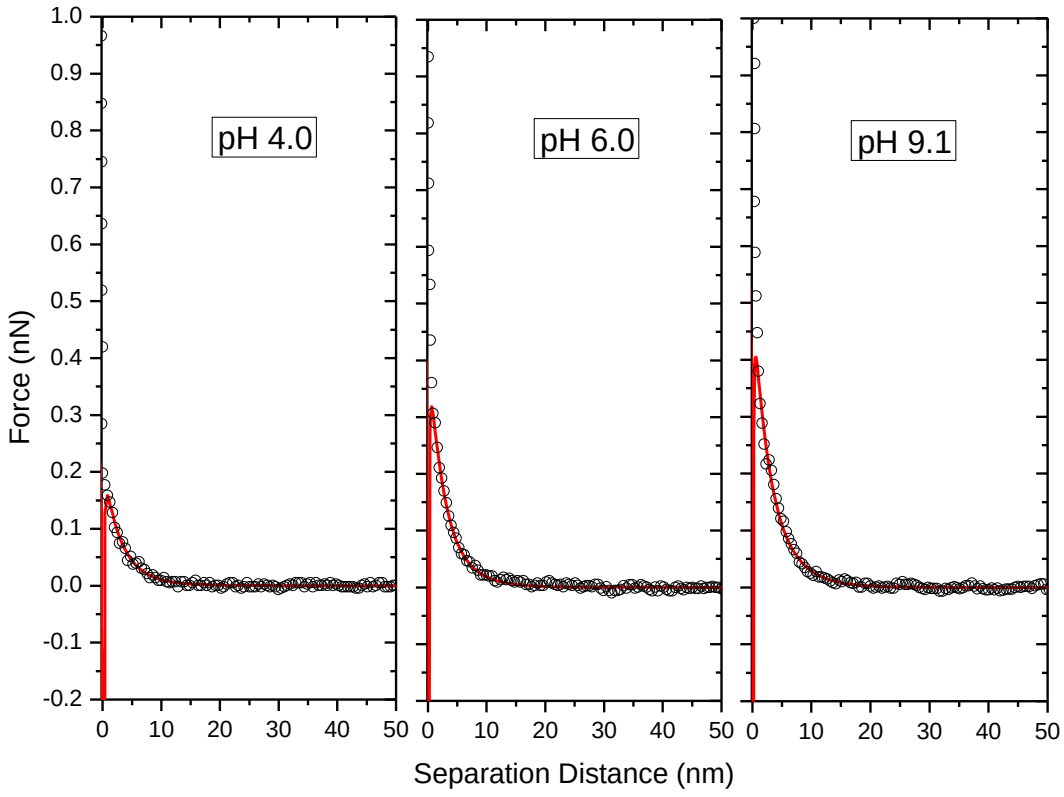

Figure 2.6. Typical interaction force curves between an AFM tip and kaolinite edge surfaces in 5 mM KCl solutions at different pH values. Symbols correspond to experimental data. The solid lines represent DLVO theoretical fits.

The surface charge density of the AFM tip was derived by measuring the surface forces between the AFM tip and a silicon wafer, assuming that the surface charge density of the AFM tip is equal to that of the silicon wafer. The measured force profiles fit very well with the classical DLVO theory down to separation distances of 3–4 nm, as shown in Figure 2.6. The surface charge density and surface potential of kaolinite edge surfaces at various pH values as obtained from fitting the force profiles are shown in Figure 2.7.

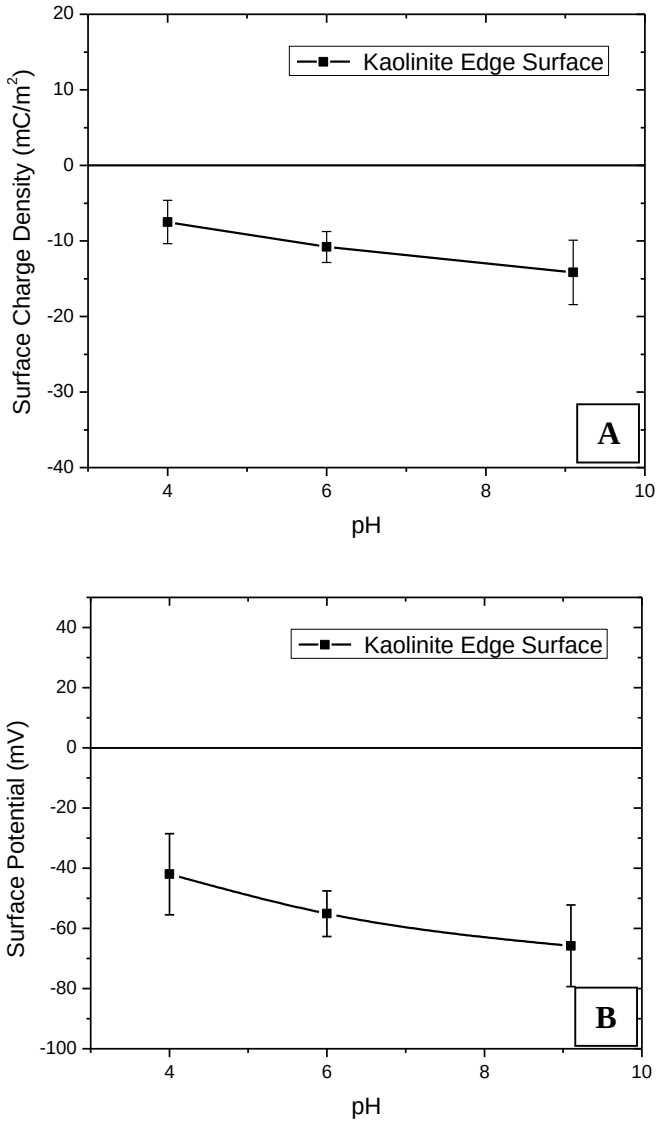

Figure 2.7. Surface charge density (A) and surface potential (B) of kaolinite edge surfaces as a function of pH in 5mM KCl solutions.

As previously mentioned, very limited research on the characteristics of kaolinite edge surfaces has been reported. Gupta et al. have estimated the point of zero charge (PZC) of the kaolinite edge surface to be pH 4.5 (Gupta et al. 2011). However, their conclusion is based on two different sources of experimental data, potentiometric titration data of whole kaolinite particles and the AFM surface force measurements on both the silica and alumina faces of kaolinite. Consequently, the estimated PZC for the edge surface has to be a very rough approximation because the edge surface charge is calculated based on the areas of each surface of the kaolinite particle. It is expected that the surface areas of the basal plane surfaces and the edge surfaces of anisotropic kaolinite particles vary over a very wide range, a situation which could introduce errors during the calculation of the edge surface charge and estimation of the edge surface PZC (see Figure 2.3 and Figure 2.4).

Yan et al. measured the PZCs of the edge surfaces of talc and muscovite, which were found to be pH 8.1 and 7.5, respectively (Yan et al. 2011). The protonation-deprotonation reactions of surface acid groups occur on the edge surface of clay minerals. The singly coordinated groups are considered to dominate the charging mechanism of the clay edge surfaces, namely Si-O^-, Si-OH, and Al-$OH^{1/2-}$ or Mg-$OH^{2/3-}$. The protonation reactions are shown in Equations (2-12) and (2-13). The equilibrium constants for protonation reactions are given in Table 2.2 (Hiemstra et al. 1989; Pokrovsky and Schott 2004; Jodin et al. 2005; Yan et al. 2011).

$$M_nO^{n\nu-2} + H^+ = M_nOH^{n\nu-1} \qquad K_H \qquad (2\text{-}12)$$

$$M_nOH^{n\nu-1} + H^+ = M_nOH_2^{n\nu} \qquad K_H \qquad (2\text{-}13)$$

Where *n* is an integer that represents the number of metal ions (M) bonded to the protonating oxygen and ν is the bond valence defined as ν=z/CN, where z is the metal ion

Table 2.2. Dominant surface groups on clay edge surfaces and corresponding protonation constants (log K_H) (Hiemstra et al. 1989; Avena et al. 2003; Pokrovsky and Schott 2004; Jodin et al. 2005)

Surface Group	Log K_H
$Si - O^-$	11.9
Si – OH	-1.9
$Al - OH^{1/2-}$	7.9-10.0
$Mg - OH^{2/3-}$	10

charge and CN is its coordination number.

The Si-OH is expected to be unreactive at the edge surface (Avena et al. 2003). It is expected that $Si\text{-}O^-$ will contribute a negative charge even in the acid pH range; $Al\text{-}OH^{1/2-}$ and $Mg\text{-}OH^{2/3-}$ undergo protonation and become positively charged below ~pH 10. We believe that the PZC of the muscovite edge surface is lower than that of the talc edge surface due to their different octahedral structures. Muscovite has a dioctahedral structure, with aluminum occupying only 2/3 of the octahedral centers, whereas talc has magnesium at all octahedral centers. The absence of aluminum in the octahedral sites of muscovite happens to be compensated for by the significant isomorphous substitution of aluminum in the silica tetrahedral layer, where about 1/4 of Si^{4+} ions are substituted by Al^{3+} ions. Consequently, the PZC of the muscovite edge surface is a little lower than that of talc. In contrast, kaolinite maintains the dioctahedral structure but has very little isomorphous substitution in the silica tetrahedral layer. The PZC of the kaolinite edge surface is expected to be significantly lower than that of the muscovite and talc edge surfaces, as shown in this study. The result also suggests that the alumina octahedral layer may not have much influence on the charge of the kaolinite edge surface.

2.3.1.4 MDS of Kaolinite Edge Surfaces

A rectangular water box was placed on the edge surface of a kaolinite crystal, which was initially 2 Å away from the surface. After minimization and 500 ps of simulation, the system reaches equilibrium state. Another 1 ns of simulation was applied, and a snapshot of kaolinite edge surfaces/water after the 1.5 ns simulation is shown in Figure 2.8. The water molecules spread on kaolinite edge surfaces, showing the hydrophilic character of the edge surfaces. The hydrophilic nature of kaolinite edge surfaces is attributed to the broken bonds at the edge surfaces, and meets the expectations expressed by other researchers (Van Olphen 1977; Brady et al. 1996).

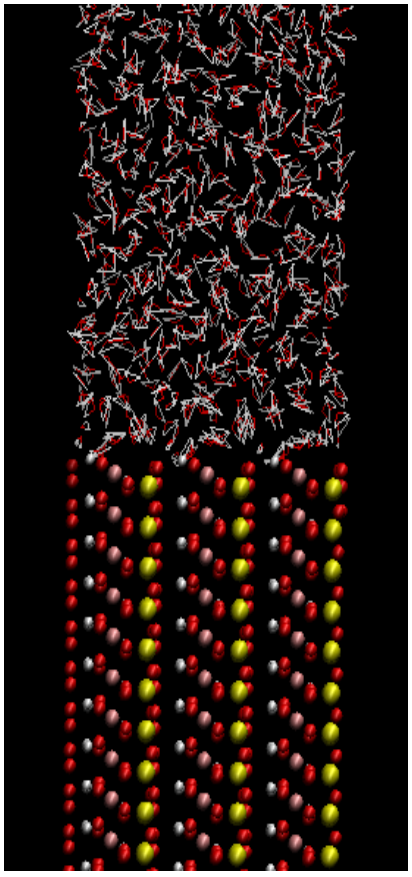

Figure 2.8. Snapshots of equilibrated configuration of kaolinite edge surfaces/water surface. Red: oxygen; yellow: silicon; green: aluminum; white: hydrogen.

2.3.2 Effect of Ionic Strength on the Silica Face of Selected Phyllosilicates

2.3.2.1 Interaction Forces between the AFM Tip and a Silica Wafer

The surface charge and surface potential of the AFM tip were determined by measuring the surface force between the AFM tip and a silica wafer. Figure 2.9 (A) is a representative AFM image of the silica wafer which has a surface roughness of 0.337 nm. Typical interaction forces between the AFM tip and the silica wafer surface are shown in Figure 2.9 (B). For all four ionic strength solutions, repulsive interaction was observed. The silica wafer is known to be negatively charged at neutral pH and at all four ionic strength conditions (Scales et al. 1990; Kosmulski 2001; Yan et al. 2011); therefore, the AFM tip is negatively charged in this study. Because of the compressed electrical double layer, the force/separation distance decreases significantly with increasing ionic strength.

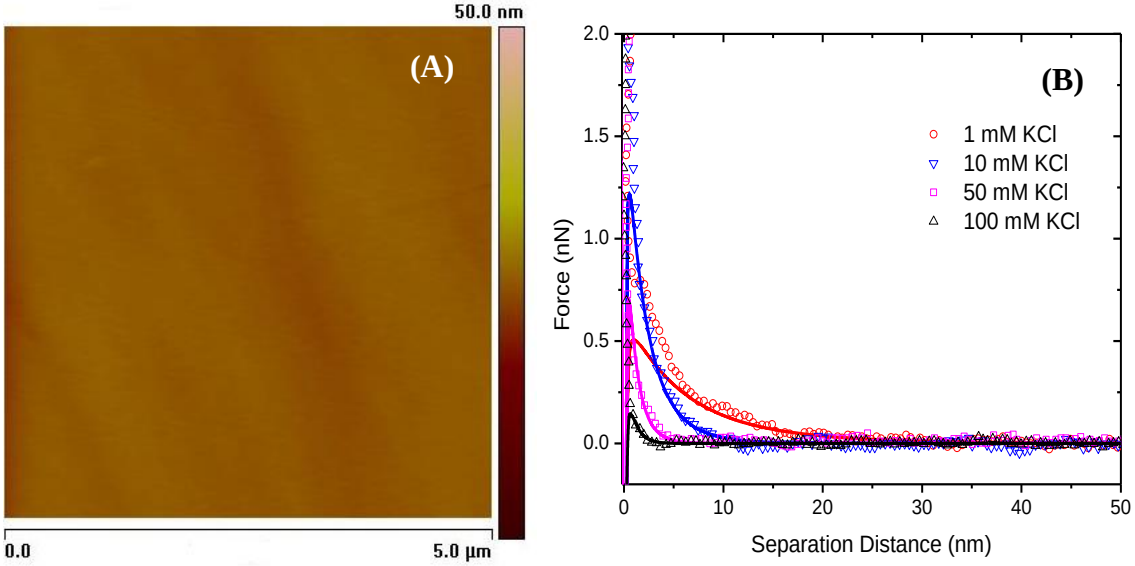

Figure 2.9. AFM force measurements at a fused silica wafer (A) Typical AFM image of a fused silica wafer (B) Typical interaction forces measured between the AFM tip and a silica wafer at pH 5.6, in 1 mM KCl, 10 mM KCl, 50 mM KCl, and 100 mM KCl solutions, respectively. Symbols correspond to experimental data. The solid lines represent the DLVO theoretical fit.

The experimental force measurement data fit very well with DLVO theoretical fitting curves in Figure 2.9 (B), especially for distances greater than the debye length. The debye lengths (κ^{-1}) for the 1 mM KCl, 10 mM KCl, 50 mM KCl, and 100 mM KCl solutions are 9.60 nm, 3.04 nm, 1.36 nm, and 0.96 nm, respectively. The discrepancy between theory and experiment at smaller separation distances is probably caused by non-DLVO forces, which are not taken into consideration in the DLVO theoretical fitting.

The surface potential of silica as a function of ionic strength from AFM fitted force curves is shown in Figure 2.10. The fitted surface potential results of the silica surface show that the surface potential decreases with increasing ionic strength. These results are similar to the zeta potential results reported in the literature (Kosmulski 2001). The difference between the AFM fitted surface potential and the zeta potential from the literature is probably because the AFM data represents a potential closer to the surface than that calculated from zeta potential measurements. The fitted potential by AFM seems to be a better estimation of the real surface potential than the zeta potential (Sokolov et al. 2006).

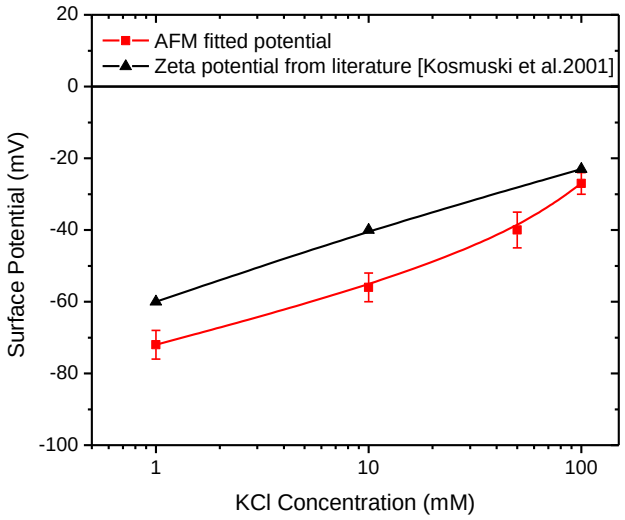

Figure 2.10. Comparison of AFM fitted surface potentials of a fused silica surface with the zeta potential results reported in literature for pH 5.6 (Data source: Kosmulski 2001).

2.3.2.2 Muscovite Basal Plane Surface

The origin of the surface charge of the muscovite basal plane surface is usually considered to be due to isomorphous substitution in the crystal lattice. In theory, the surface charge density of the muscovite basal plane surface is supposed to be independent of ionic strength (Van Olphen 1977). A representative AFM image of a muscovite basal plane surface, which has a surface roughness of 0.341 nm, is shown in Figure 2.11 (A). The surface force measurements for the muscovite basal plane surfaces are shown in Figure 2.11 (B). For all ionic strength conditions, repulsive interaction between the AFM tip and the muscovite basal plane surface is demonstrated, indicating that the muscovite basal plane surface is negatively charged (Yan et al. 2011). The measured force profiles fit very well with the DLVO theoretical fitting curves, especially at distances greater than κ^{-1}.

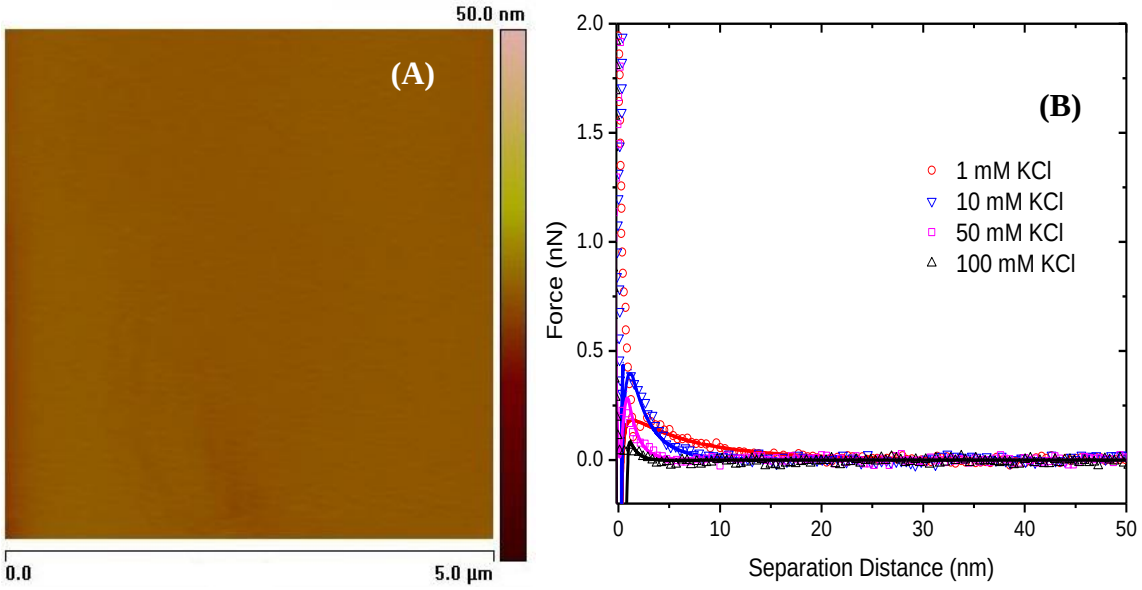

Figure 2.11. AFM force measurements at the muscovite surface (A) Typical AFM image of a muscovite basal plane surface (B) Interaction forces between the AFM tip and the muscovite basal plane surface as a function of ionic strength at pH 5.6. Symbols correspond to experimental data. The solid lines represent the DLVO theoretical fit.

2.3.2.3 Talc Basal Plane Surface

A representative AFM image of a talc basal plane surface, which has a surface roughness of 0.838 nm, is shown in Figure 2.12 (A). The surface force measurements on the talc basal plane surfaces are shown in Figure 2.12 (B). For all ionic strength conditions, repulsive interaction between the AFM tip and the talc basal plane surface is demonstrated, indicating the talc basal plane surface is negatively charged at pH 5.6 (Yan et al. 2011). Note because of the very hydrophobic nature of the talc surface, bubbles are easily generated when injecting aqueous solution and when the AFM tip approaches the surface. Care must be exercised to avoid bubble generation. Experimental difficulties have been experienced with the 100 mM KCl solution and the data are not presented in Figure 2.12 (B).

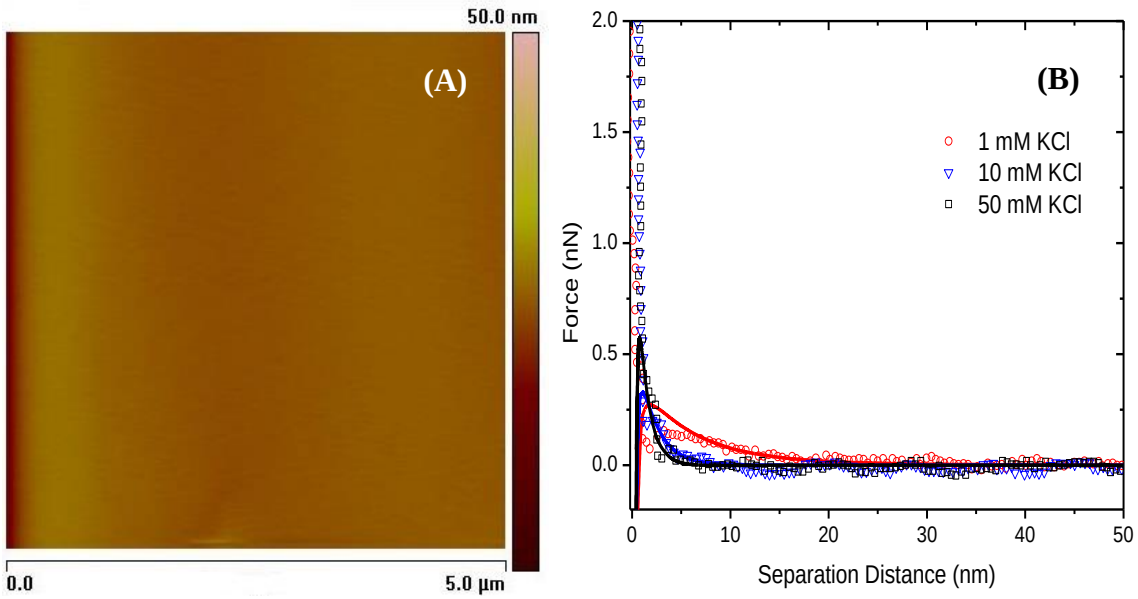

Figure 2.12. AFM force measurements at the talc surface (A) Typical AFM image of a talc basal plane surface (B) Interaction forces between the AFM tip and the talc basal plane surface as a function of ionic strength at pH 5.6. Symbols correspond to experimental data. The solid lines represent the DLVO theoretical fit.

2.3.2.4 Kaolinite Silica Face

A representative AFM image of kaolinite particles with the silica faces exposed is shown in Figure 2.13 (A). The surface force measurements on the kaolinite silica faces at different ionic strength conditions are shown in Figure 2.13 (B). For all ionic strength conditions, repulsive interaction between the AFM tip and the kaolinite silica face is demonstrated, indicating the kaolinite silica face is negatively charged at pH 5.6 (Gupta and Miller 2010). A detailed discussion on the surface charge of kaolinite silica faces as a function of ionic strength will be given in section 2.3.2.5.

2.3.2.5 Comparison of the Surface Charges of the Silica Faces of Selected Phyllosilicates as a Function of Ionic Strength

Results based upon fitting of the force curves, the surface charge densities and surface potentials of the muscovite basal plane surface, the talc basal plane surface, and the kaolinite silica surface are summarized in Figure 2.14 (A) and (B), respectively, as a function of ionic strength. Note for 50 mM KCl and 100 mM KCl solutions, the variance for the estimated values is relatively large, caused by the limitation of the AFM technique when measuring the surface force at a highly screened electrical double layer and very short separation distance. It is obvious that the muscovite basal plane surface maintains the highest surface charge density, followed by the kaolinite silica surface and the talc basal plane surface. These results are consistent with the degree of isomorphous substitution in the phyllosilicate lattice, where muscovite is believed to have one fourth of the silicon substituted by aluminum, the kaolinite silica face has moderate isomorphous substitution, and talc is thought to have only a very small amount of substitution (Van Olphen 1977; Meunier and Fradin 2005; Yin et al. 2012; Mierczynska-Vasilev and Beattie 2013).

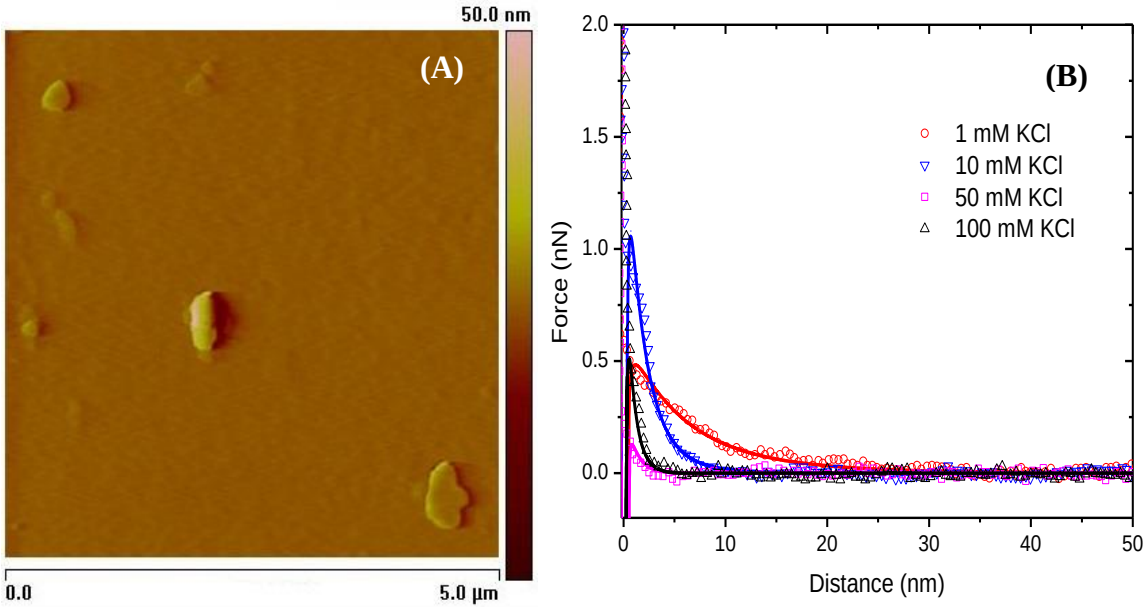

Figure 2.13. AFM force measurements at the kaolinite silica face surface (A) Typical AFM image of a kaolinite silica face (B) Interaction forces between the AFM tip and the kaolinite silica face as a function of ionic strength at pH 5.6. Symbols correspond to experimental data. The solid lines represent the DLVO theoretical fit.

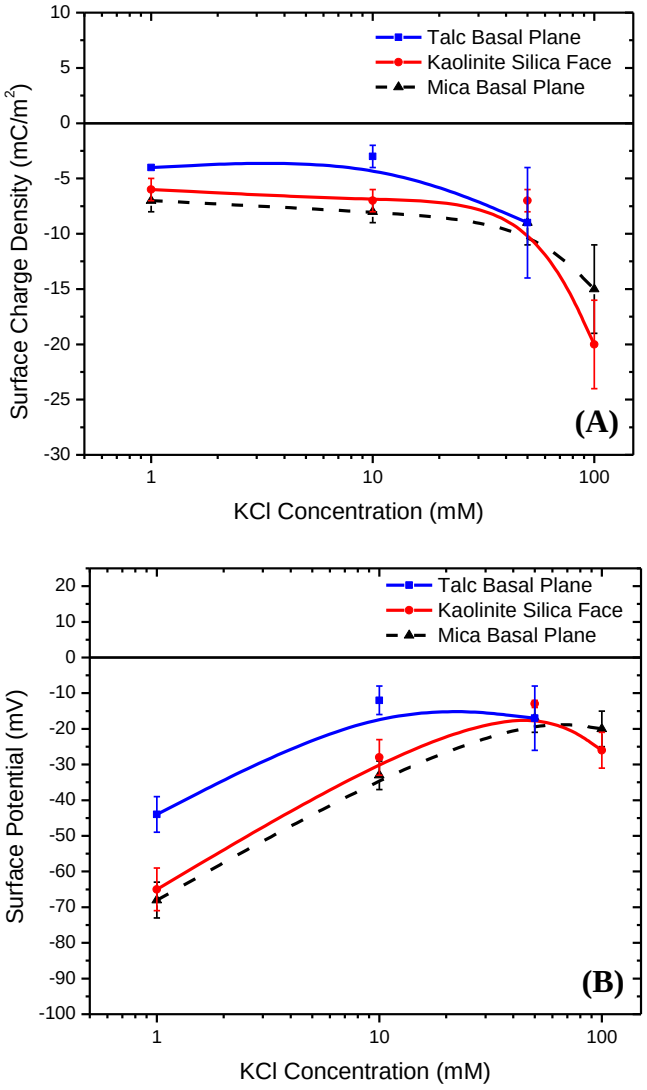

Figure 2.14. Surface charge densities (A) and surface potentials (B) of the muscovite (mica) basal plane surface, talc basal plane surface, and kaolinite silica face as a function of ionic strength at pH 5.6.

The isomorphous substitution is also believed to be responsible for the wetting characteristics of these three clay minerals (Yin et al. 2012), with wetting by water decreasing in the sequence, muscovite face > kaolinite silica face > talc face. The sequence is from mica with a hydrophilic surface state, to kaolinite with some moderate hydrophobic character, to talc which is strongly hydrophobic.

The surface charge densities of all three clay minerals are almost constant for low ionic strength solutions, as expected, but increase at high ionic strength. The surface potentials of all three minerals decrease with increasing ionic strength for low ionic strength solutions, but change little at high ionic strength. The surface charge densities of clay minerals at high ionic strengths are difficult to maintain constant, maybe due to the strong compression of the electrical double layer and limited diffuse ions confined in the electrical double layer.

In the case of muscovite [$KAl_2AlSi_3O_{10}(OH)_2$], theoretically every fourth silicon in the tetrahedral layer is substituted by aluminum, and compensated by potassium ions. In this way, the surface charge of the muscovite basal plane is calculated to be about 340 mC/m^2. However, the surface charge density of the muscovite basal plane is measured to be about 10 mC/m^2 by AFM surface force measurements. This means only about 10/340 of the potassium ions, or about 3%, were released in order to account for the surface charge calculated from the AFM surface force measurements. Of course it should be recognized that the surface charge calculated from AFM measurements is at some small distance from the actual muscovite face surface.

2.3.3 Effect of Ionic Strength on the Properties of Kaolinite Surfaces

Typical force curves between the AFM tip and kaolinite alumina face and edge surfaces are shown in Figure 2.15 and Figure 2.16, respectively. Results for the silica face have already been presented in Figure 2.13. Attractive interaction between the AFM tip and the kaolinite alumina face is demonstrated for all ionic strength conditions, while repulsive interaction between the AFM tip and the kaolinite edge surfaces is observed. The results indicate that at pH 5.6, the kaolinite alumina face is positively charged, and the edge surface is negatively charged. As mentioned previously, the silica face is negatively charged at all pH values. These results are consistent with results reported in the literature (Gupta and Miller 2010; Liu et al. 2014). The experimental data fit very well with DLVO theoretical fitting curves, especially at larger separation distances.

The surface charge densities and surface potentials of kaolinite surfaces, obtained from the force curves, are summarized in Figure 2.17 (A) and (B). The kaolinite silica face tends to follow the constant surface charge model, while the surface potential decreases significantly with increasing ionic strength. However, for both the alumina face and the edge surface, protonation/deprotonation reactions are expected to occur in the aqueous solution, the surface charge density increases significantly, and the surface potential remains constant as the ionic strength increases. At neutral pH and higher ionic strength, the increased surface charge of the kaolinite alumina and edge surfaces is expected to promote the alumina face to silica face interaction between particles, and the alumina face to edge surface interaction. The overall particle interaction is expected to be enhanced. However, at the 100 mM KCl solution, the surface charge density of the alumina face slightly decreases and that of the silica face increases, which may be due to slight non-

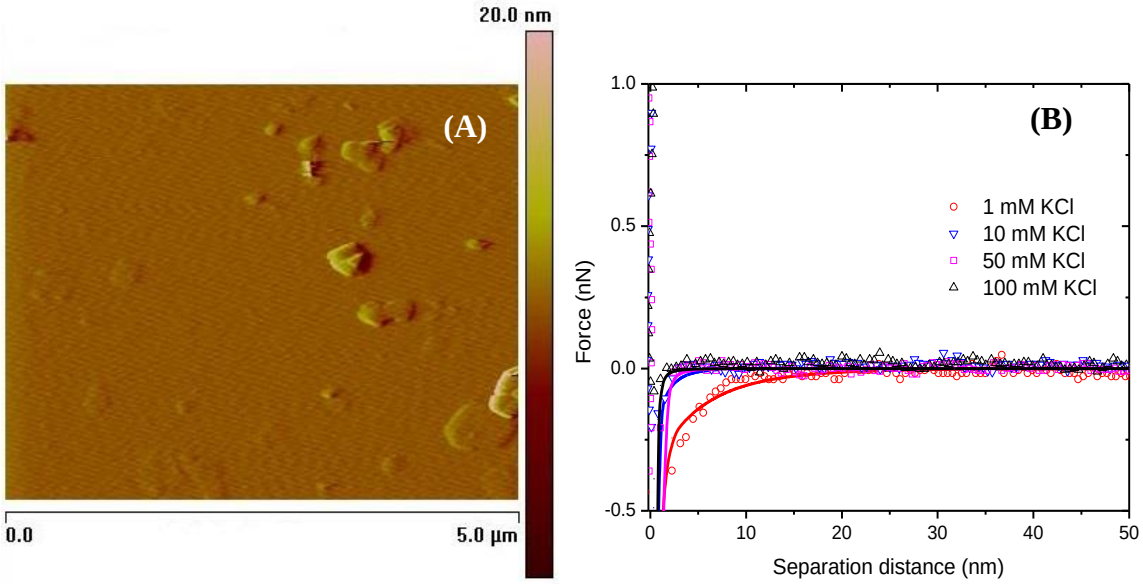

Figure 2.15. AFM force measurements at the kaolinite alumina face (A) Typical AFM image of a kaolinite alumina face (B) Interaction forces between the AFM tip and kaolinite alumina face as a function of ionic strength at pH 5.6. Symbols correspond to experimental data. The solid lines represent the DLVO theoretical fit.

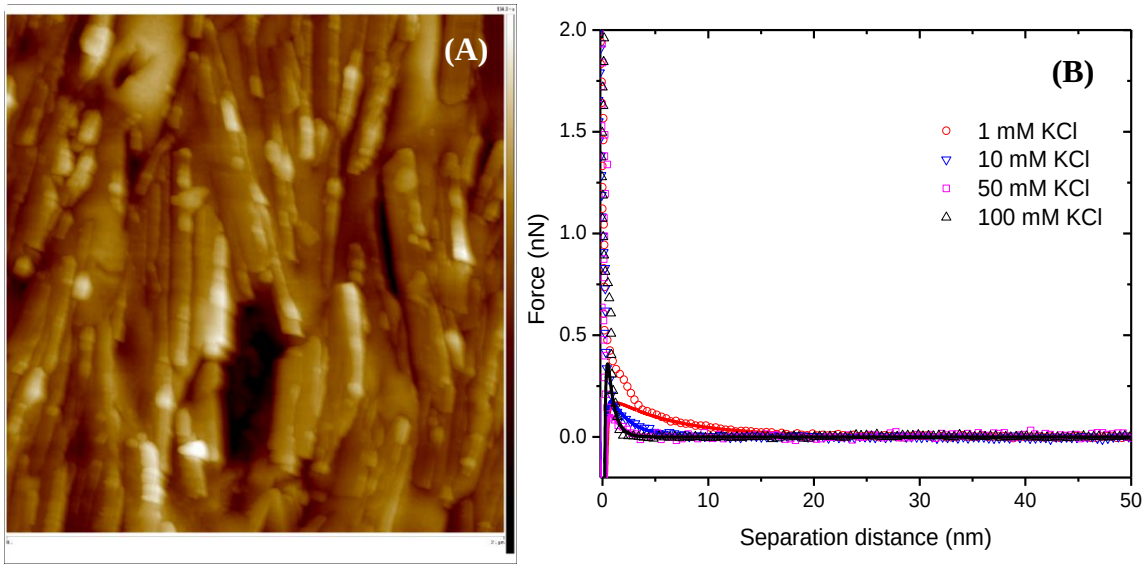

Figure 2.16. AFM force measurements at the kaolinite edge surface (A) Typical AFM image of a kaolinite edge surface (B) Interaction forces between the AFM tip and the kaolinite edge surface as a function of ionic strength at pH 5.6. Symbols correspond to experimental data. The solid lines represent the DLVO theoretical fit.

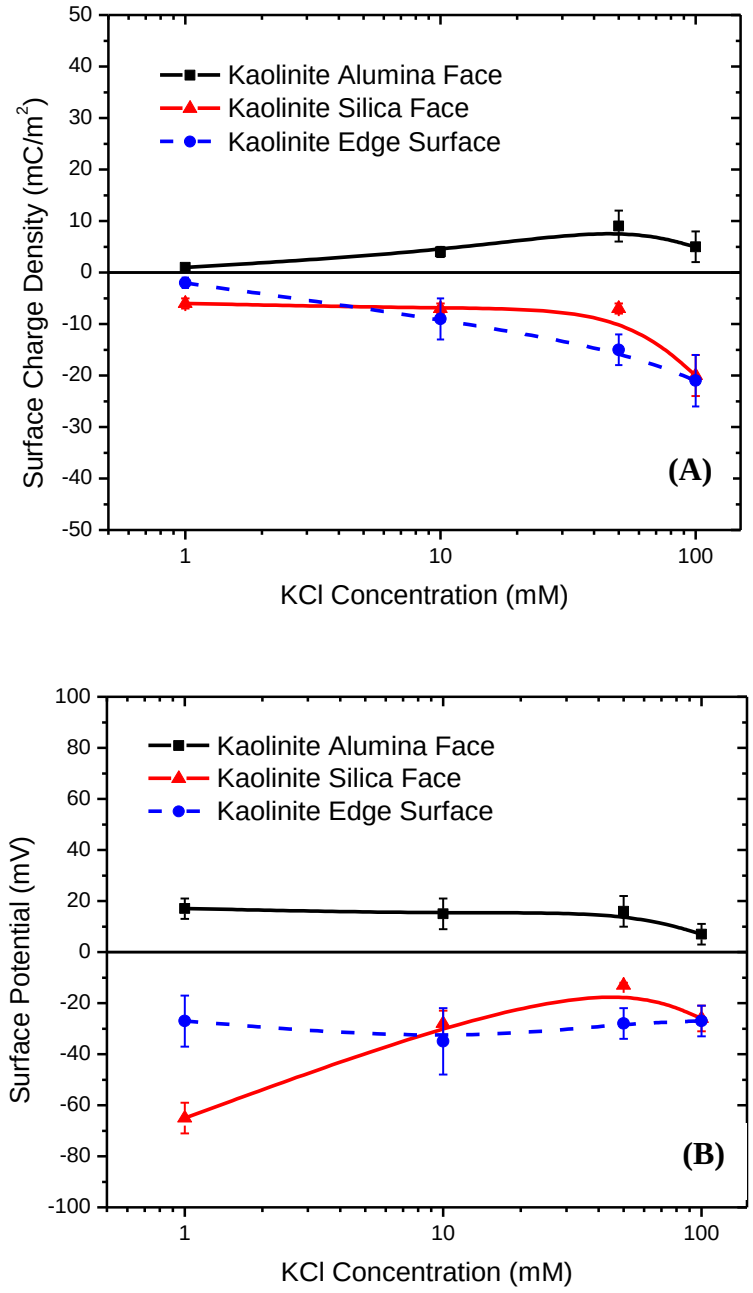

Figure 2.17. Surface charge densities (A) and surface potentials (B) of kaolinite surfaces as a function of ionic strength at pH 5.6.

specific adsorption of Cl^- under this condition. Note the electrical double layer has been compressed significantly as shown in Figure 2.13, Figure 2.15, Figure 2.16; a higher ionic strength solution greater than 100 mM was not used since AFM measurements and surface charge calculations under these circumstances will be difficult.

2.3.4 Effect of Ionic Strength on the Cluster Size

The cluster size of kaolinite particles in suspension at pH 5.6 is shown in Figure 2.18. As the ionic strength increases, the cluster size first increases, then decreases at 100 mM KCl solution, and finally increases again and reaches a plateau value of about 3 microns. Note for the photon correlation spectroscopy (PCS) method, the cluster size results are based on the assumption that the clusters have spherical geometry. For kaolinite particles, with a high aspect ratio, the results from PCS may be questioned, but it seems that the PCS results give an indication of how cluster size changes with ionic strength (Swartzen-Allen and Matijevic 1974). In any case, based on subsequent research results presented in Chapter 3, the kaolinite clusters grow to a size of a few microns and have an isometric shape. The size distribution is also shown to be slightly broader with increasing ionic strength, except for a small decrease for the 100 mM KCl solution.

The cluster size of kaolinite particles as a function of ionic strength is the result of the competition between electrostatic forces and van der Waals forces. The van der Waals attractive force is independent of ionic strength, and is of the right magnitude and range to compete with the electrostatic force (Parsegian et al. 1975; Van Olphen 1977). At low ionic strength, the electrostatic attractive forces between the alumina face and the silica face, and some alumina faces and edge surfaces, are dominant. With increasing ionic strength, the surface charge of the alumina face and the edge surface increases significantly, as shown

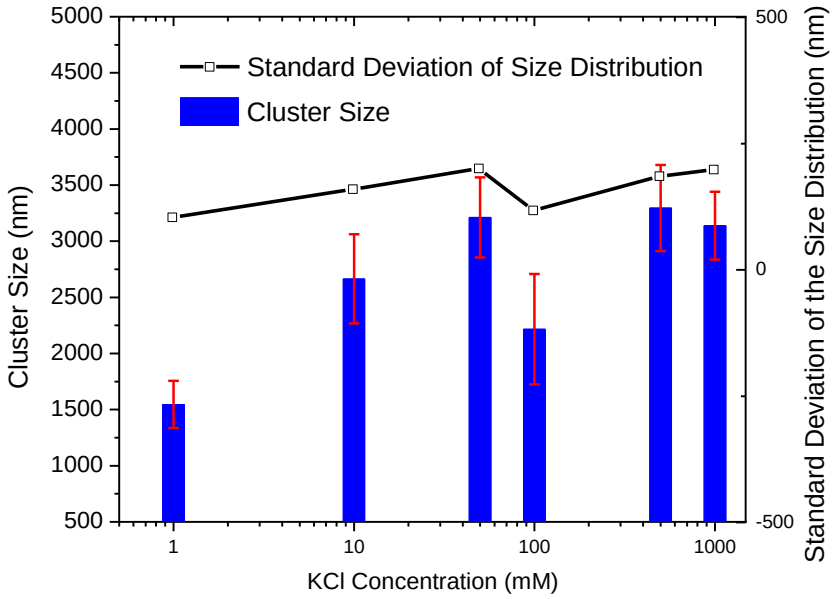

Figure 2.18. Kaolinite cluster size as a function of ionic strength (1 mM, 10 mM, 50 mM, 100 mM, 500 mM, and 1000 mM) at pH 5.6; the open square data represent the standard deviation of each size distribution.

in Figure 2.17, promoting the alumina face–edge surface interaction, and the alumina face–silica face interaction.

For 100 mM KCl solution, the surface charge of the positively charged alumina face decreases unexpectedly, and the attractive electrostatic interaction between the alumina face and silica face, and between the alumina face and edge surface, is weakened; the electrostatic repulsion is stronger because of the increase of the surface charge of the silica face and edge surface. Studies have suggested that a critical ionic strength exists for van der Waals interaction to dominate and change the particle interaction structure (Palomino and Santamarina 2005). In our study, when the ionic strength increases further, the van der Waals attraction is totally predominant, the cluster size increases again, and a cluster size plateau is finally reached. These results suggest that 100 mM is the critical ionic strength condition above which the van der Waals forces are dominant and account for the formation of stable kaolinite clusters a few microns in size.

2.4 Summary

With a new experimental protocol, well-oriented kaolinite particles (~500–700 nm) were prepared as an epoxy resin sandwich structure and cut with an ultramicrotome for the characterization of kaolinite edge surfaces. The kaolinite edge surfaces were imaged by AFM and identified according their surface morphology. The thickness of kaolinite edges was evaluated and found to be 38.3 nm ± 11.7 nm in this study. Interaction forces were measured between a very sharp silicon tip (radius of curvature estimated to be 3–4 nm) and kaolinite edge surfaces. The measured surface forces fit very well with the classical DLVO theory. The surface charge density and surface potential of kaolinite edge surfaces were calculated from fitting the force profiles. The point of zero charge of kaolinite edge surfaces

was found to be below pH 4, which is much lower than expected based on the PZC of other layered silicates edge surfaces. This conclusion regarding the kaolinite edge surface was based on repeatable measurements with multiple fresh surfaces. The AFM measurements suggest that the alumina octahedral layer does not have much influence on the charge of the kaolinite edge surface, which may be due to the lack of isomorphous substitution of Al^{3+} ions for Si^{4+} ions in the tetrahedral layer of the kaolinite structure. In addition, the hydrophilic character of kaolinite edge surfaces was established from MD simulations.

Research results successfully demonstrate a method to prepare kaolinite edge surfaces from 500 nm particles and the ability to measure the surface properties of clay mineral edge surfaces by AFM. With the methodology developed, investigation on the surface characteristics of other layered silicates is possible. We also believe our surface force results provide a better understanding of the interaction between kaolinite particles, which is important in many areas of technology, including improved flotation strategies for the recovery and utilization of valuable mineral and energy resources.

Using AFM, the surface charge and surface potential of muscovite basal plane surfaces, talc basal plane surfaces, and kaolinite surfaces were analyzed as a function of ionic strength based on DLVO theory. The silica face of these phyllosilicates follows the constant surface charge model with the addition of an electrolyte, the surface charge having a slight increase at high ionic strength. In addition, the surface charge of the muscovite was found to be much greater than the surface charge of the talc surface. The silica face of kaolinite shows a moderate surface charge density, consistent with, and explained by, the degree of isomorphous substitution in the crystal lattice. It is also expected that only 10 of 340 potassium ions, or about 3%, are released from the muscovite face surface in order to

account for the surface charge calculated from the AFM surface force measurements. The surface charge densities of the kaolinite alumina face and edge surface increased significantly with increasing ionic strength, except at high ionic strength, where the surface charge of the kaolinite silica face increases, and the surface charge of kaolinite alumina face decreases.

The cluster size of kaolinite particles for selected ionic strength solutions was measured by photon correlation spectroscopy. With increasing ionic strength, the cluster size first increases, decreases at 100 mM KCl solution, then increases again and finally reaches a plateau level of 3 microns. This is a reflection of the competition between the electrostatic interaction and the van der Waals attractive interaction. With increasing ionic strength, the van der Waals attraction becomes more significant and, as a result, bigger clusters are formed. For 100 mM KCl solution, an increase in electrostatic repulsion prevents the growth of the clusters. When the ionic strength increases further, the electrostatic repulsion is reduced, and the cluster formation is promoted again by the van der Waals attraction.

Results from this research are important for solving environmental issues, such as colloid transport, and are also useful in the development of flotation technology. The effect of ionic strength on the surface charge and cluster size of clay minerals has been established and will provide a foundation for the modeling of aggregation phenomena.

The effect of ionic strength on collector adsorption and the flotation recovery of clay minerals should be studied in the future. It is expected that the results from this study will provide scientific support in the use of saline water for the processing of mineral

resources containing clay minerals, including processing operations, such as flotation and sedimentation for water recovery and utilization.

CHAPTER 3

BROWNIAN DYNAMICS SIMULATION OF KAOLINITE PARTICLE INTERACTIONS AND CLUSTER FORMATION

3.1 Introduction

The behavior of kaolinite suspensions is of significant importance in many areas of technology, including mineral processing, specifically flotation and dewatering processes. Besides, understanding of kaolinite particle interactions is fundamental for research regarding suspension stability and rheological behavior. Due to the unique features of kaolinite particles, including their anisotropic surface charge and platy particle shape, the characteristics of kaolinite particle interactions can be very complex.

Attempts to study the structure of clay particle interactions has long been of interest. H. van Olphen described several modes of particle interaction: face to face, face to edge, and edge to edge (Van Olphen 1977). One of the three modes of particle interactions can be dominant, yet a mixture of two or three modes may exist. It is expected that a three-dimensional card-house structure will be formed with edge–face and edge–edge interactions. O'Brien suggested the face to face mode accounted for the aggregated structure as well, resulting in a large void ratio for the structure, as shown in Figure 3.1 (O'Brien 1971).

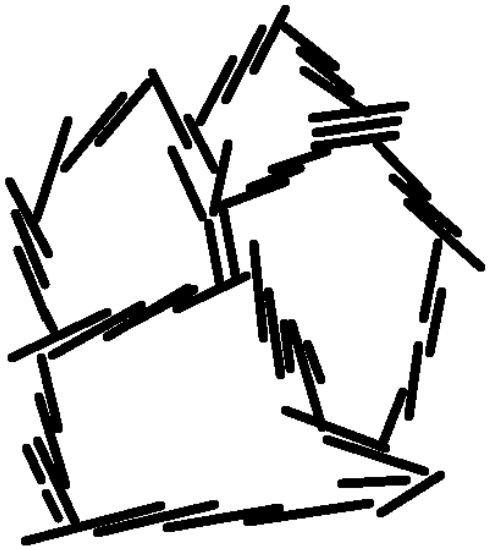

Figure 3.1. Stairstep card-house fabric of aggregated kaolinite particles (Data Source: O'Brien 1971).

Generally, the structure of clusters arising from particle interactions is considered to be a manifestation of the interplay of the electrostatic force and the van der Waals force (Mitchell and Soga 1976; Van Olphen 1977; Palomino and Santamarina 2005). Due to the misunderstanding of the surface properties of kaolinite particles, the significance of face to edge electrostatic interaction has been overestimated. Past researchers have incorrectly considered that the two kaolinite face surfaces are negatively charged and that the edge surface is positively charged. Recent results show that the alumina face surface and the silica face surface carry opposite charges at low pH, and the edge surface is negatively charged above pH 4 (Gupta and Miller 2010; Liu et al. 2014). The face to face electrostatic attraction is as important as, and even more important than, the face to edge electrostatic interaction. In other cases, for example at high ionic strength, the electric double layer is compressed, and the van der Waals interaction is dominant. In this regard, the interactions of face to face, face to edge, and edge to edge are all possible due to the van der Waals

attraction.

The fabric of kaolinite clusters has been anticipated based on the measurement of sedimentation and viscosity as a function of pH and ionic strength. The van der Waals attraction is expected to prevail beyond a critical pH level and a threshold ionic concentration (Rand and Melton 1977; Palomino and Santamarina 2005). Cluster structure has been inferred from the hypothesis that the face to edge interaction causes higher apparent viscosity and larger sedimentation volume, while the face to face interaction results in lower apparent viscosity and smaller sedimentation volume for the kaolinite suspension (Schofield and Samson 1954; Palomino and Santamarina 2005). At low pH (~pH 3), a face to face interaction is expected; at intermediate pH (pH 7–9) and intermediate salt concentrations (3 mM to 100 mM), suspension settling behavior suggests a mixture of particle interactions, which is initially dispersed then having edge to face interaction (Palomino and Santamarina 2005).

Direct examination of kaolinite clusters in–situ is difficult because the primary particles are below one micron in size and complex cluster structures are formed in the aqueous suspension. Imaging in a wet environment with such small particle size is a challenge for modern instruments. Some researchers have tried direct SEM imaging of kaolinite clusters by a freeze-drying technique, or cryo-SEM (O'Brien 1971; Pierre et al. 1995; Zbik et al. 2008; Gupta et al. 2011). Complex structures of particle clusters have been presented as a function of pH. However, concern exists if the cluster structure is maintained during drying or freezing. Further, the resolution of SEM without high vacuum is limited and discrimination of the two face surfaces of kaolinite is not achieved.

Simulation is another possible approach to describe the structure of kaolinite

clusters. Recent advances in computational power and development of corresponding software allow for analysis even at the molecular level. In this regard, simulation of kaolinite interactions and cluster formation is considered in this chapter. A wide range of simulation methods should be recognized, including the molecular scale (quantum chemistry, atomistic molecular dynamics), meso scale (coarse-grained MD, Dissipative Particle Dynamics) and macro scale (Computational Fluid Dynamics). Molecular dynamics simulation has been widely applied to the study of clay minerals, including the adsorption of water and collector (Boulet et al. 2004; Greenwell et al. 2005; Du and Miller 2007; Yin et al. 2013). The interfacial structure and orientation of water molecules at the clay surfaces have been explored. However, the all-atom molecular dynamics simulation is very time consuming with many pairwise potential calculations for inner atoms of the mineral crystal, which is not necessary for the simulation of particle interactions. In the meantime, it is recognized that the surface chemistry of kaolinite particles accounts for particle interactions; therefore, the macro-scale simulation which oversimplifies the surface chemistry of anisotropic kaolinite particles is not considered. Consequently, a meso-scale simulation for kaolinite particle interactions is appropriate.

Recently, particle interactions using a meso-scale simulation technique have been reported (Odriozola et al. 2004; Anderson et al. 2005; Markutsya et al. 2008; Suter et al. 2009). Molecular dynamics (MD) simulations on a mesoscopic scale have been carried out to study the dispersion of disc-shaped Laponite clay platelets (Kutter et al. 2000). Nevertheless, Markutsya et al. demonstrated that the computational efficiency for the simulation of nanoparticle aggregation by using Brownian dynamics (BD) is much greater than using MD, due to additional calculations for the aggregates and the solvent in MD

simulations (Markutsya et al. 2008). Unfortunately, only spherical particles or platy particles with one face surface have been simulated. Kaolinite cluster formation with the complex surface chemistry of kaolinite particles has not been studied. In this regard, a Brownian dynamics simulation of kaolinite particle interactions with two different basal plane surfaces (two different face surfaces) has been accomplished for the first time and the results are reported in this chapter.

3.2 Experimental Methods

3.2.1 Coarse-Grained Model

As shown in Figure 1.2, the crystal structure of kaolinite is very complex. If each of the atoms in the crystal is involved in the pairwise potential calculation as accomplished by traditional all-atom simulation methods, the simulation will be very time-consuming and not necessary for the simulation of particle interactions. In fact, for multiparticle interactions, the surface properties of the particles are most important, but the contribution from the pairwise potential of inner particle atoms is very limited. In this regard, a coarse-grained model of kaolinite particles has been constructed to include the surface properties of small kaolinite particles in order to facilitate computations.

Two types of spheres were used to construct the alumina and the silica surfaces of a hexagonal platy shaped particle, as shown in Figure 3.2. Each sphere has a diameter of 1 Å, which was arbitrarily selected to facilitate computation. One alumina sphere and one silica sphere with a vertical distance of 1 Å from their centers are grouped as one unit. The distance between the centers of two adjacent units is 2 Å. A typical kaolinite particle contains 61 units and 122 spheres in total. The surface charge of each sphere is assigned based on experimental AFM data (Gupta and Miller 2010). Appropriate coding was

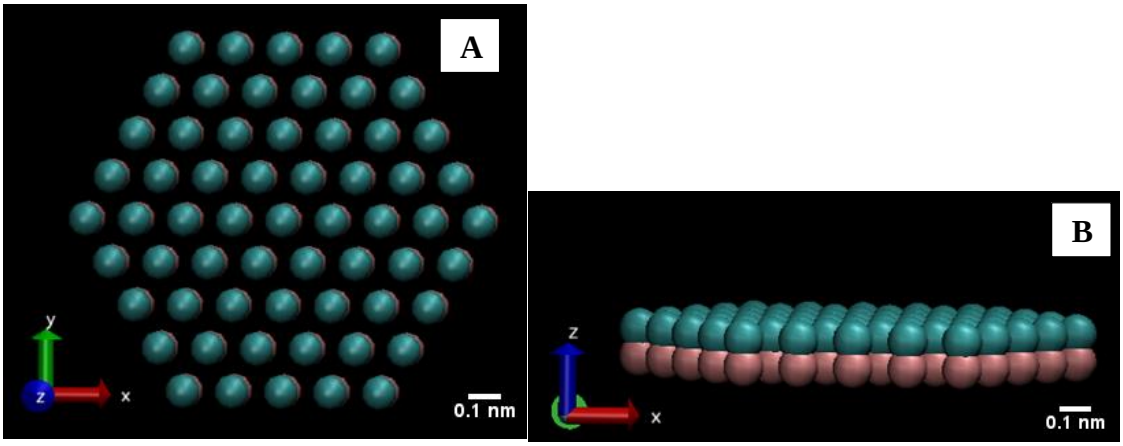

Figure 3.2. Coarse-grained model for kaolinite particles (A) Top view (B) Side view. Cyan spheres represent the alumina face surface of the kaolinite particle, and pink spheres represent the silica face surface of the kaolinite particle.

accomplished in Moltemplate 1.17 to generate their coordination (Jewett et al. 2013).

3.2.2 Simulation Details

LAMMPS (Large-scale Atomic/Molecular Massively Parallel Simulator) was used for the simulation of kaolinite particle interactions (Plimpton et al. 2007). Each kaolinite particle was built using the coarse-grained model introduced in Section 3.2.1. Brownian dynamics approach, which considers the motion of particles as Brownian, was used in the simulation, and the particle interaction, mainly caused by the charge of the surfaces, was considered as will be discussed in this section. All the simulations were performed in a cubic cell of (250 Å × 250 Å × 250 Å) in size, using periodic boundary conditions in all three dimensions. The number of particles was added according to the desired particle concentration for the kaolinite suspension.

The solvent (water) was treated as a structureless dielectric continuum characterized by its relative permittivity, ε_r. Monovalent salt and counterions were represented implicitly by the debye length, κ^{-1}.

The interactions between colloidal particles are computed by DLVO model (Derjaguin–Landau–Vervey–Overbeek), which describes the balance between the van der Waals potential and electrostatic potential.

The van der Waals potential between two colloidal particles (spheres) is expressed by the following equation (Hamaker 1937; Everaers and Ejtehadi 2003):

$$U_{vdw} = -\frac{A_{12}}{6}\left[\frac{2a_1a_2}{r_{12}^2-(a_1+a_2)^2}+\frac{2a_1a_2}{r_{12}^2-(a_1-a_2)^2}+\ln\left(\frac{r_{12}^2-(a_1+a_2)^2}{r_{12}^2-(a_1-a_2)^2}\right)\right] \tag{3-1}$$

A_{12} refers to Hamaker's constant, a_1 and a_2 are the radii of the two colloidal particles (spheres), and r_{12} is the distance between two colloidal particles (spheres).

Due to the existence of electrolytes, the electrostatic potential is expressed in the form of screened Coulomb or Yukawa potential, as described by the following equation.

$$U_{Yukawa} = \frac{A}{\kappa}e^{-\kappa(r-(a_1+a_2))} \qquad r < r_c \tag{3-2}$$

$$A = 2\times\pi\times a\times\varepsilon_0\times\varepsilon_r\times\kappa\times\psi^2 \tag{3-3}$$

Where r_c is the cutoff, ε_0 is the permittivity of free space, ε_r is the relative permittivity of fluid medium, κ is the inverse screening length, and ψ is the surface potential.

Therefore, the total DLVO potential is expressed as follows.

$$U_{DLVO} = U_{yukawa} + U_{vdw} \tag{3-1}$$

In fact the results for the potential between two primary particles (hexagon plates) is a summation of the colloidal potential considering all colloids (spheres) that are made up of each primary particle (hexagon plates). It is obvious that the potential calculation between spheres in the same particle is not necessary and is excluded.

In addition, in order to avoid particle penetration during collision, a shifted and

truncated Lennard–Jones potential is used for a distance $r_{12} \leq 2^{1/6}$.

$$U_{lj} = 4\varepsilon_{lj}\left(\left(\frac{\sigma_{lj}}{r_{12}}\right)^{12} - \left(\frac{\sigma_{lj}}{r_{12}}\right)^{6}\right) + \varepsilon_{lj} \qquad r_{12} \leq 2^{1/6} \tag{3-2}$$

Where ε_{lj} and σ_{lj} are the Lennard–Jones parameters, with ε_{lj} =0.5k_BT and σ_{lj} =1Å in all simulations.

The surface charge density used in the simulation was assigned as shown in Table 3.1. The simulation study is designed to provide a qualitative analysis for the formation of cluster structure as a function of pH, simulation time, and ionic strength, etc.; in this case, the assigned surface charge of kaolinite particles is suitable for our research purpose (Odriozola et al. 2004; Delhorme et al. 2012). As described in Chapter 2 and applied in the simulations, the silica surface of a kaolinite particle is negatively charged and the alumina surface of a kaolinite particle is positively charged at low pH (pH 5), and both surfaces are negatively charged at high pH (pH 8). In the simulations, the charge of the edge surface of a kaolinite particle is the average of the charges of two basal plane surfaces, which is negative at both pH 5 and pH 8 but more negative at pH 8.

Table 3.1. The surface charge density of silica and alumina surfaces at 1 mM KCl used in the simulation.

pH	Surfaces	Surface Charge Density
5	Silica Surface	-2.0 e/sphere
	Alumina Surface	0.5 e/sphere
8	Silica Surface	-1.8 e/sphere
	Alumina Surface	-1.3 e/sphere

A random initial configuration of the kaolinite particles was established first. Brownian dynamics was applied for the simulation of kaolinite particle interactions. A Langevin thermostat was applied to model the interaction of particles with a background implicit solvent (Schneider and Stoll 1978). Constant NVE (constant energy and constant volume) integration was performed to update the position and velocity of the particles each timestep. The temperature of the system was set to be 298K. For the first 500 ps of the simulation, a timestep of 1 fs was used. Later, timesteps of 2 fs were used for a total simulation of 10 ns, 20 ns, or 30 ns.

3.2.3 Cluster Identification and Description

The following terms used in this chapter need to be defined before further discussion.

1) Particle Structure

The particle structure established by the aggregation of kaolinite particles is discussed in terms of interactions of surfaces, the size distribution of structures, expressed as number of particles per structure, and the relative exposure of surfaces (alumina and silica faces).

2) Particle Cluster

A cluster consists of a particle structure and associated water. In this regard, the cluster size/shape is defined by the ellipsoid which envelopes the particle structure.

3) Cluster Size, Shape, and Composition

Cluster size is described from ellipsoid dimensions and number of particles per cluster, shape is described by the aspect ratio and its variation. Finally, then, the cluster composition is described by the water content.

The center of mass (C.M.) of each particle in the system was computed during the simulation, which is an available output option in LAMMPS. When the simulation finished, the aggregated particle structure size, defined as the number of particles in a particular particle structure, was determined with an implemented package 'nnclust' in R software by finding the nearest neighbors of each particle. The maximum separation distance of the C.M. for two adjacent particles was selected as 16 Å, the criterion for determining if the particles are in the same aggregated particle structure. The distance between each pair of particles was calculated and in this way, based on this distance criterion, aggregated particle structure identity was established.

3.2.4 Surface Area of Particle Structures

The external surface area of particles in each aggregated particle structure was calculated by EDTsurf method using the technique of Euclidean Distance Transform (EDT) (Xu and Zhang 2009). Triangulated mesh surfaces were constructed from volumetric solids by a Vertex-Connected Marching Cube algorithm (Lorensen and Cline 1987; Xu and Zhang 2009). Distance Transform is a transformation that converts a digital binary image to another grey scale image, where the value of each pixel in the image is the minimum distance from the background to the pixel by a predefined distance function. The distance function for Euclidean distance between two points (x_1, y_1, z_1) and (x_2, y_2, z_2) is described by the following equation:

$$d_{Euclidean} = \sqrt{(x_1 - x_2)^2 + (y_1 - y_2)^2 + (z_1 - z_2)^2} \quad (3\text{-}3)$$

In this way, the boundary points or the surface of an object *O* are determined by calculating the distance between a random point *x* and point *y* from the object *O*. Using the

space-filling method, the object is filled by volumetric solids (Greer and Bush 1978; Juffer and Vogel 1998). The voxels whose Euclidean distances are less than the probe radius (1.4 Å) were removed. The remaining solid is the surface of the object. The Vertex-Connected Marching Cube method was applied to construct the triangulated surfaces from the volumetric models. By way of example, analysis of the particle structure surface for a cluster is considered in Sections 3.3.1 and 3.3.2.

After being constructed with the EDTsurf method, the aggregated particle structures were exported to individual files for the analysis of surface area. The surface areas of silica faces and alumina faces in an aggregated particle structure were estimated by MeshLab based on their color (Cignoni et al. 2008).

3.2.5 Viscosity Simulation and Calculation Based on Particle Structures

The shear viscosity is usually expressed according to the following equation,

$$J = -\eta \frac{dV_x}{dy} \tag{3-4}$$

Where J is the momentum flux, V_x is the velocity of the fluid in x direction, $\frac{dV_x}{dy}$ is the spatial gradient of the velocity of the fluid moving in y direction, and η is the viscosity.

The Green–Kubo (GK) model was applied for the viscosity calculation from the simulation, which was implemented in LAMMPS (Green 1954; Kubo 1957). Instead of expressing the viscosity with the momentum flux vs. the velocity gradient as shown in equation (3-7), the Green–Kubo formula relates the ensemble average of the auto-correlation of the stress/pressure tensor to η as shown in Equation (3-8). By computing the average of the integrated pressure tensor over a correlation time of t, the viscosity η was

established. The average viscosity of each kaolinite suspension simulated was computed for an additional 1 ns.

$$\eta = \frac{V}{k_B T} \int_0^\infty dt \left\langle p(0)\, p(t) \right\rangle_0 \tag{3-5}$$

Where V is the volume of the system, T is the temperature, k_B is the Boltzmann constant, $p(0)$ and $p(t)$ represent the pressure tensor at time 0 and time t, and $\langle ... \rangle_0$ means the average over time t. A correlation time of 10 ps and a sampling interval of 5 were used to establish the correlation function for pressure and viscosity.

Experimental measurements for the viscosity of kaolinite suspensions were accomplished by Gupta (Gupta 2010) with HAAKE MARS III (Thermo Scientific Inc.) rheometer. The cone-and-plate geometry was used with a cone angle of $1°$ and diameter of 60 mm. The cone truncation was preset to 0.052 mm. All measurements were conducted at 25 ℃. Measurement accuracy of the rheometer was verified by performing measurements using deionized water, and also silicon oil of viscosity 10 cst. About 1.5 ml of kaolinite suspension was placed in between cone-and-plate, and the viscosity of the particle suspension of 1%, 3%, and 5% was measured. The experiments were repeated 3 times at each pH condition.

3.2.6 SEM Imaging

A concentrated kaolinite suspension (~50%wt) was prepared at the desired pH for SEM imaging. FEI QUANTA 600 FEG was used for Environmental SEM (ESEM) imaging of the kaolinite suspension at low vacuum. The kaolinite suspension of less than 1 ml was kept in a peltier cooled sample holder. The temperature and pressure were decreased slowly while the water vapor was still allowed in the SEM specimen chamber.

In this way, the cluster structure of the kaolinite suspension was imaged in a “wet” environment. However, the resolution of ESEM was decreased dramatically due to the low vacuum applied.

A WETSEM capsule (QX-102, QuantomiX Ltd., Israel) allows the SEM imaging of fully hydrated kaolinite suspension at high vacuum (Barshack et al. 2004). The schematic drawing shown in Figure 3.3 describes operation of the WETSEM capsules. 15 µl of the suspension was injected into a well-sealed WETSEM capsule, which was separated from the interior of the electron microscope by a thin, electron-transparent partition membrane. This membrane is strong enough to sustain a 1 atm pressure difference and, in this way, the sample inside the capsule can be maintained at atmospheric pressure while the SEM chamber reached high vacuum. The electrons penetrate a few microns into the wet cluster and an SEM image of the cluster structure is obtained.

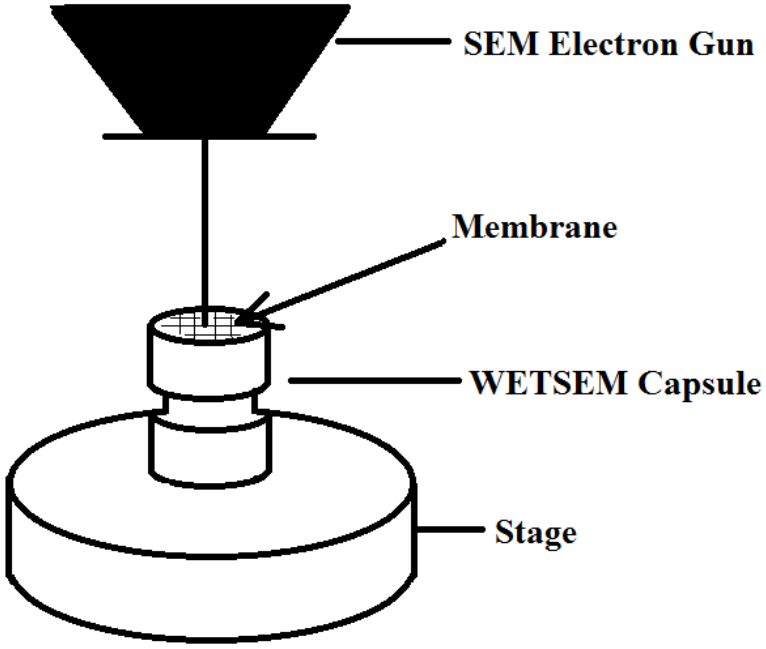

Figure 3.3. Schematic drawing of SEM imaging with a WETSEM capsule.

3.2.7 X-ray Micro Computed Tomography

A three-dimensional experimental technique, which is X-ray Micro CT (XMT), has been used to validate the structure and composition of kaolinite clusters. The kaolinite suspension at pH 4 was prepared and consolidated overnight. The wet sediment was packed and sealed in the sample holder for XMT scanning. The working theory of XMT is briefly described in Figure 3.4. The X-ray source transmitted through the sample, which is located in a rotational stage. A projection, formed by a set of line-integrals of the attenuation coefficients of the material along a given direction followed by the ray, is acquired by a 2D detector. The X-ray attenuation coefficient at each voxel depends on the characteristics of materials, including the mineral density, effective atomic number, and the X-ray energy (McCullough 1975). A set of transform functions and algorithms are applied to reconstruct the three-dimensional images of the sample from the projection data, which have been described in the literature (Lin and Miller 2002; Videla et al. 2006).

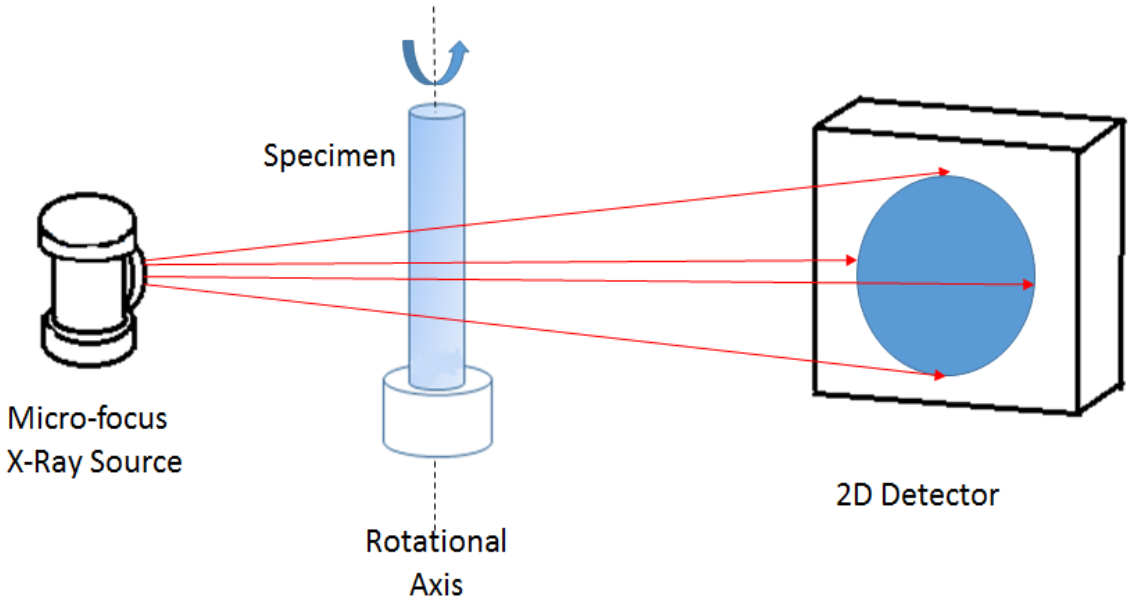

Figure 3.4. Schematic drawing of cone-beam X-ray Micro Computed Tomography system.

3.3 Results and Discussion

3.3.1 Effect of pH on Particle Interactions and Particle Structures

Figures 3.5 (A) and (B) show snapshots of 1000 kaolinite particles at pH 5 and pH 8 after 10 ns simulation time. A size distribution of the primary kaolinite particles was used in the simulations. The particle size is described by the number of spheres on the side of a hexagon layer, The ratio of the number of particles with size of 7, 6, 5, 4, 3 spheres is 1:2:4:2:1. The number of particles with their corresponding particle size is presented in Table 3.2. For the simulation at pH 5, the silica face surfaces and the edge surfaces of kaolinite are negatively charged; the alumina face surfaces are positively charged. The particles are stacked layer by layer with silica face surface attracted to the alumina face surface; after a certain thickness of stacking occurs, the edge surface starts to be attracted to the alumina face surface. In this way, more silica face surfaces are expected to be exposed to the environment when compared to the exposure of alumina face surfaces. The observed aggregated particle structure is close to that expected by O'Brien as shown in Figure 3.1 (O'Brien 1971). In contrast, at pH 8, all surfaces of kaolinite particles are negatively charged. The particles are well dispersed, and no obvious interactions are observed at pH 8, as shown in Figure 3.5 (B).

The surface area of the aggregated particle structure at pH 5 is calculated as 258,865 $Å^2$ by EDTsurf method, and the surface area at pH 8 is 804,950 $Å^2$, which is almost 4 times larger than that calculated at pH 5. Moreover, the volume of the aggregated particle structure is 928,776 $Å^3$ at pH 5 and the volume at pH 8 is 1,628,250 $Å^3$. Note the volume calculated from the software is always overestimated since the boundary of each aggregated structure or particle dispersed is overestimated by the analyzing probe. In any

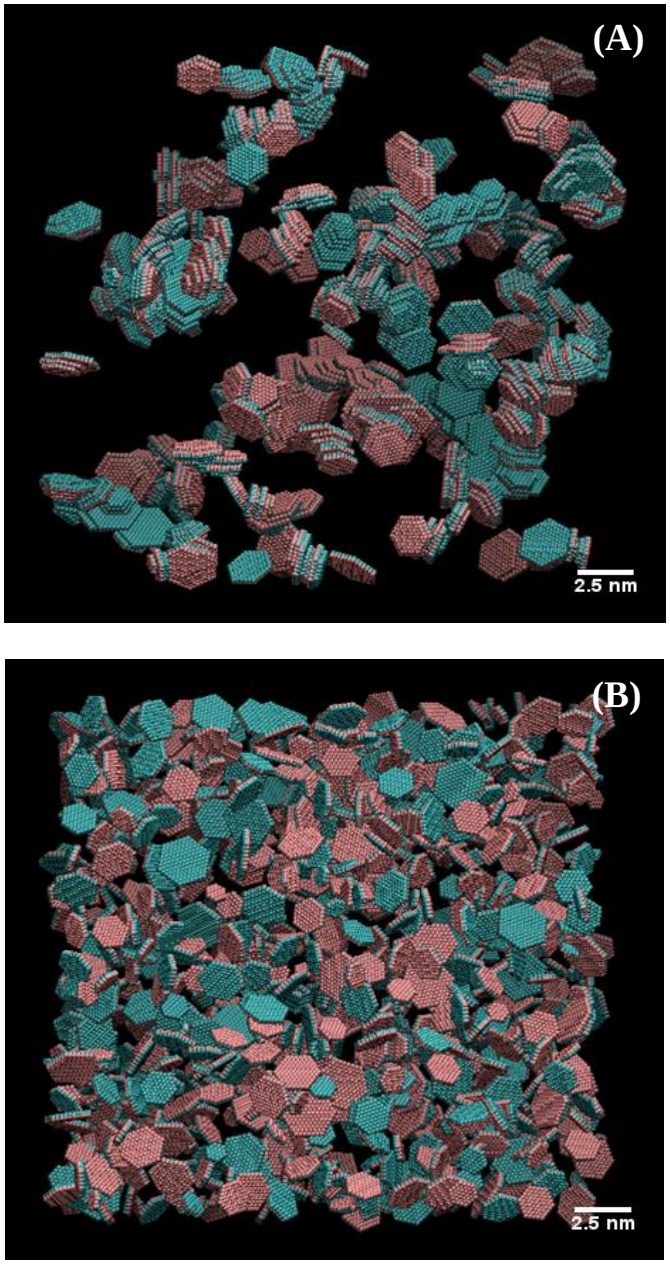

Figure 3.5. Brownian dynamics simulation snapshot of 1000 kaolinite particles after 10 ns simulation time at pH 5 (A) and at pH 8 (B). Pink spheres represent the silica face surfaces of kaolinite particles, and cyan spheres represent the alumina face surfaces of kaolinite particles.

Table 3.2. Number of primary kaolinite particles and their corresponding particle size for the simulation.

# of spheres on the side of a hexagon layer	7	6	5	4	3
# of spheres in one particle	254	182	122	74	20
# of particles in the simulation system	100	200	400	200	100

case, the results indicate the particles have significant aggregation and the particle structures are compacted at pH 5, which accounts for the smaller surface area and smaller volume; in contrast, the particles are well dispersed at pH 8, resulting in a larger surface area and larger volume.

Figure 3.6 (A) shows the center of mass (C.M.) for kaolinite particles and identification of particle structures at pH 5. Each dot represents the C.M. of one primary kaolinite particle. The particles belonging to one cluster are represented by one color. As mentioned before, many aggregated particle structures are formed at pH 5; however, at pH 8, most particles are well dispersed. See Figure 3.6 (B). The results indicate that at low pH, the alumina face to silica face interaction and the alumina face to edge surface interaction are dominant, mainly due to the electrostatic attraction. Note the equilibrium state has not yet been reached for pH 5; a more complicated aggregated particle structure may be expected with longer simulation times.

Typical aggregated particle structures from the simulation at pH 5 are shown individually in Figure 3.7, where the face to face interactions and face to edge interactions are observed. The total surface area of each aggregated particle structure and the surface area of the alumina face and the silica face were calculated and summarized in Table 3.3.

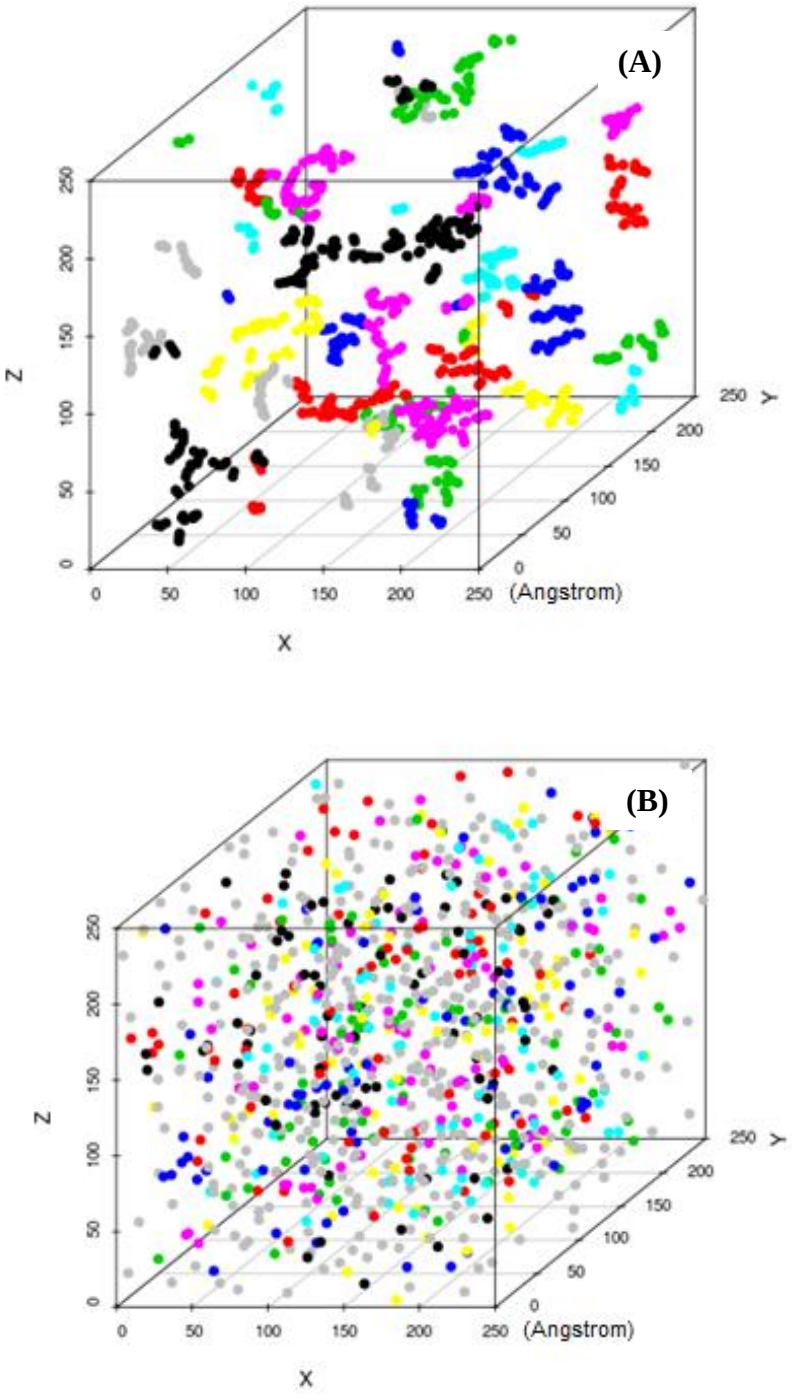

Figure 3.6. Representation of the center of mass (C.M.) of kaolinite particles and aggregated particle structure identification (by color) after 10 ns simulation time at pH 5 (A) and at pH 8 (B).

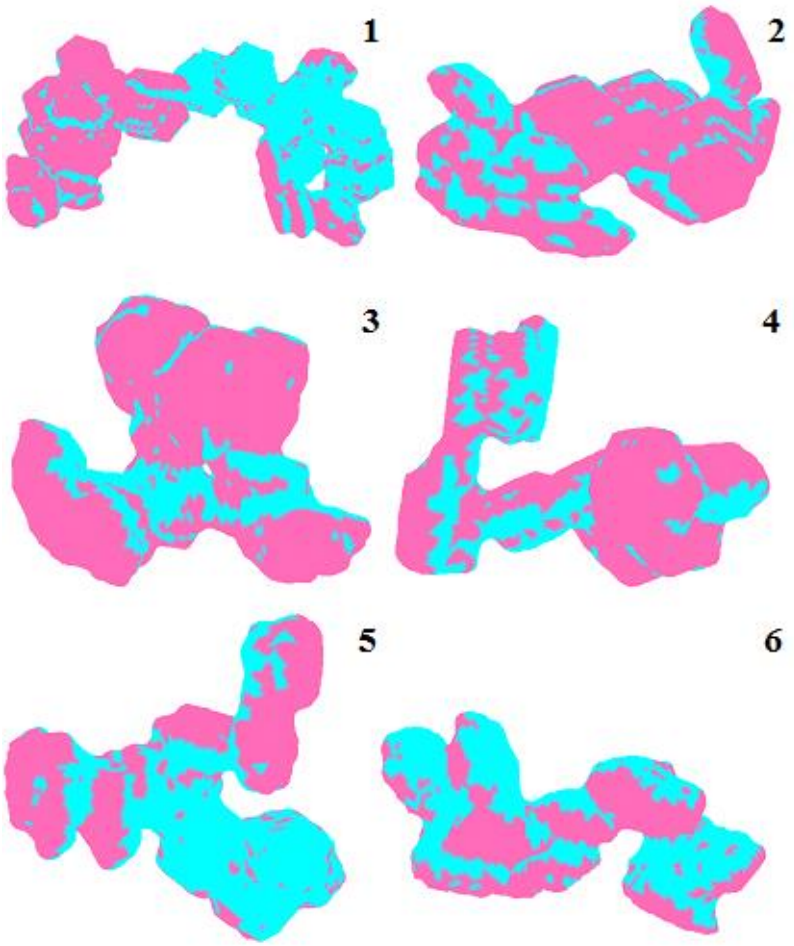

Figure 3.7. Representation of typical aggregated particle structures formed at pH 5 after 10 ns simulation time. The particle structures are filled with volumetric solids by EDTsurf method. The pink surfaces represent the silica face surfaces of kaolinite particles, and the cyan surfaces represent the alumina face surfaces of kaolinite particles.

Table 3.3. Surface area of typical aggregated particle structures after the simulation of 10 ns and areas of the silica and the alumina surfaces in each particle structure. The percent of each surface area (silica and alumina) for the particle structures is listed together with the average of the six particle structures. The particle structure number is corresponding to that labeled in Figure 3.7.

Particle Structure Number	Surface Area of the Particle Structure ($Å^2$)	Area of Silica Surface ($Å^2$)	Area of Alumina Surface ($Å^2$)	% of Silica Surface	% of Alumina Surface
1	22,377	12,408	9,969	55.4%	44.6%
2	14,258	7,716	6,541	54.1%	45.6%
3	10,900	5,965	4,935	54.7%	45.3%
4	10,671	5,917	4,755	55.4%	44.6%
5	10,446	5,775	4,672	55.3%	44.7%
6	9,304	5,060	4,244	54.4%	45.6%
Average	/	/	/	54.9%	45.1%

In Table 3.3, note the edge surface of the kaolinite particles accounts for the surface area of silica and alumina surfaces as well. The percent of the silica surface area or the alumina surface area over the total aggregated particle structure surface area is very close for individual aggregated particle structures and the average percent of the silica surface area and the alumina surface area for the 6 aggregated particle structures described in Table 3.3 were found to be 54.9% and 45.1%, respectively. About 10% higher surface area was found for the silica surface in the aggregated particle structure.

3.3.2 Ellipsoid Enveloped Clusters

The composition of the kaolinite clusters with respect to water content should be considered in order to explain flotation phenomena, sedimentation, consolidation, and

other mineral processing processes.

The water content in the cluster can be described using an ellipsoid model, in which an ellipsoid is fitted to envelope the aggregated particle structure. The same center of mass of the aggregated particle structure is used for ellipsoid fitting and definition of the cluster structure. The bounding box of each cluster is computed and the volume of the ellipsoid model is calculated. The original particle structure volume and the ellipsoid volume of the clusters are summarized in Table 3.4 (for the simulation of 1000 particles with a simulation time of 10 ns). The volume percent of kaolinite particles for clusters in the ellipsoid model is presented as well. The more complex the cluster structure, the lower the percent solids in the ellipsoid enveloped clusters. This indicates more water is included in the clusters having a more complex structure. In contrast, the results also suggest that the percent of particles in the cluster increases significantly as the cluster size decreases. In fact, previous studies have suggested that the porosity of the clusters increases with the growth of the clusters (Vold 1963; Klimpel and Hogg 1991; Hogg 2013). Note the percent solids and the cluster size are not linearly related; this is due to the fact that the amount of water included in the ellipsoid model is influenced by the aspect ratio of the clusters. Of course a bigger aspect ratio for a cluster will result in more water contained within cluster, although the cluster size and structure should be taken into consideration as well. For large clusters (cluster number 1–31), a sudden increase in the aspect ratio of the clusters generally accounts for a decrease in the percent solids. However, for small clusters (cluster number 32–47), similar phenomena are not observed due to the small number of particles being fitted by the ellipsoid model. The average volume percent solids was found to be 48.4%, which helps to describe the composition of kaolinite clusters.

Table 3.4. Volume of each aggregated structure, the cluster volume if the cluster is fitted by an ellipsoid model, and the percent solids in the cluster.

Cluster Number	Volume (Å^3)	Ellipsoid Volume (Å^3)	Aspect Ratio	% Solids
1	85,449	483,619	2.07	17.7%
2	54,961	163,708	1.59	33.6%
3	42,071	110,323	1.42	38.1%
4	37,669	143,116	1.16	26.3%
5	38,172	157,128	1.49	24.3%
6	35,261	109,395	1.47	32.2%
7	34,004	108,393	1.30	31.4%
8	32,780	125,736	1.44	26.1%
9	31,688	122,770	1.21	25.8%
10	31,001	74,272	1.53	41.7%
11	24,807	61,501	1.52	40.3%
12	24,607	56,260	1.33	43.7%
13	22,006	59,099	1.54	37.2%
14	20,985	55,427	1.68	37.9%
15	20,525	39,312	1.39	52.2%
16	22,511	43,056	1.15	52.3%
17	20,065	37,740	1.33	53.2%
18	16,639	36,691	2.14	45.3%
19	18,347	33,920	1.16	54.1%
20	13,446	28,956	1.23	46.4%
21	12,815	22,987	1.48	55.7%
22	13,520	28,454	1.11	47.5%
23	12,355	33,430	1.53	37.0%
24	12,459	27,846	1.32	44.7%
25	11,270	24,916	1.33	45.2%
26	11,081	28,654	1.31	38.7%
27	10,671	24,113	1.41	44.3%
28	10,720	18,316	1.32	58.5%
29	9,314	19,634	1.45	47.4%
30	11,387	21,902	1.17	52.0%
31	8,580	20,592	2.05	41.7%
32	9,116	17,846	1.82	51.1%
33	8,397	13,978	1.90	60.0%
34	7,890	15,007	1.42	52.6%
35	9,508	13,057	1.15	72.8%
36	7,815	14,443	1.14	54.1%
37	5,917	11,457	1.42	51.6%
38	6,413	10,025	1.62	64.0%
39	6,910	9,140	1.00	75.6%
40	5,287	6,523	2.29	81.1%
41	5,464	12,630	1.34	43.3%

Table 3.4. Continued

Cluster Number	Volume ($Å^3$)	Ellipsoid Volume ($Å^3$)	Aspect Ratio	% Solids
42	3,952	5,700	2.07	69.3%
43	4,488	6,490	1.30	69.2%
44	2,935	4,018	1.44	73.0%
45	2,543	4,210	1.44	60.4%
46	2,314	4,324	1.22	53.5%
47	419	598	1.16	70.2%
Average	/	/	1.45	48.4%

Some parameters (porosity, density, and relative particle area) indicating the composition of kaolinite clusters measured by experimental methods and reported in the literature are summarized in Table 3.5. At low pH (4–6), the porosity of clusters is significantly larger than that of the clusters at high pH (8). The large porosity and low density suggest the existence of water in large amount in the clusters. However, these experimental data are not suitable for quantitative comparison with the cluster simulation results reported in this chapter, because the experimental data are analyzed based on cryo-SEM images for which the original cluster structure is not preserved during the freezing process (Du et al. 2009).

3.3.3 Effect of Simulation Time—Aggregated Particle Size and Structure

As indicated in Section 3.3.1, the aggregated particle structures/clusters may continue to grow after 10 ns of simulation at pH 5. Thus, the effect of simulation time on the aggregated particle structures is reported in this section. Figure 3.8 (A) shows a snapshot of kaolinite particles at pH 5 after simulation for 20 ns and Figure 3.8 (B) represents the C.M. of kaolinite particles as well as aggregated particle structure identification (by color). If the simulation is extended further to 30 ns, a similar snapshot of the results and analysis are shown in Figure 3.9. As shown in Figure 3.8 and Figure 3.9, more complex aggregated particle structures, similar to the "card-house" structure, are developed with increasing simulation time. The results have confirmed that the aggregation of particles continues with increasing simulation time without reaching an equilibrium state.

The aggregated particle structure size distributions as represented by the number of particles per aggregate structure at pH 5 are presented in Figure 3.10 as a function of

Table 3.5. Experimental data for the relative particle area, porosity, and density of kaolinite clusters reported in the literature.

pH	Relative Particle Area (%)	Porosity (%)	Density (g/cm^3)	Reference
4	/	90	/	(Zbik et al. 2008)
8	/	30	/	(Zbik et al. 2008)
~6	8.64	/	2.0	(Du et al. 2009)
~6	/	90-95	1.05-1.10	(Likos and Lu 2001)

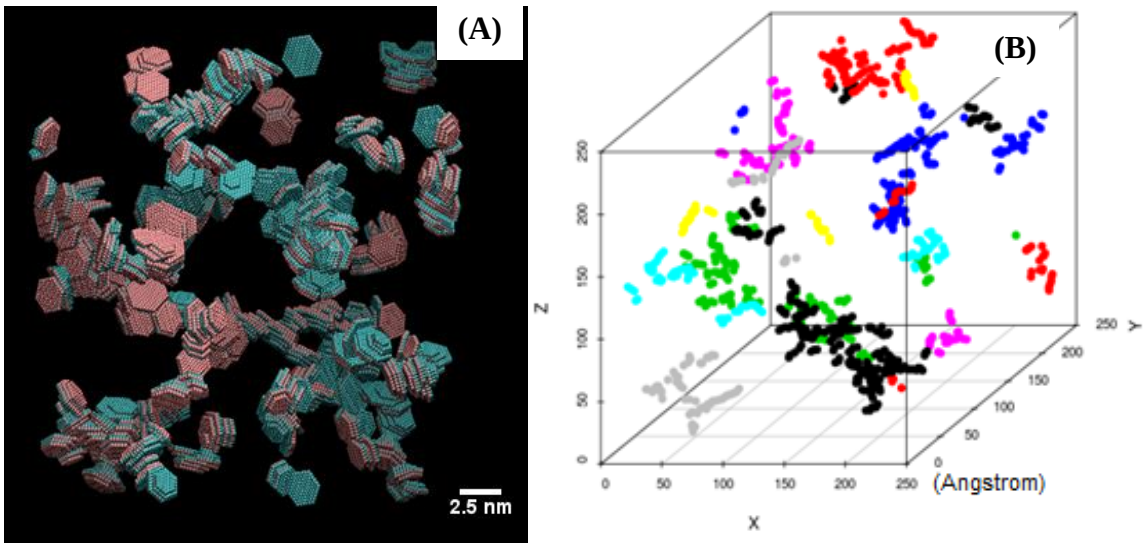

Figure 3.8. Brownian dynamics simulation of 1000 kaolinite particles at pH 5 after 20 ns simulation time: snapshot of the simulation results (A) and representation of the center of mass (C.M.) of kaolinite particles and aggregated particle structure identification (by color) (B).

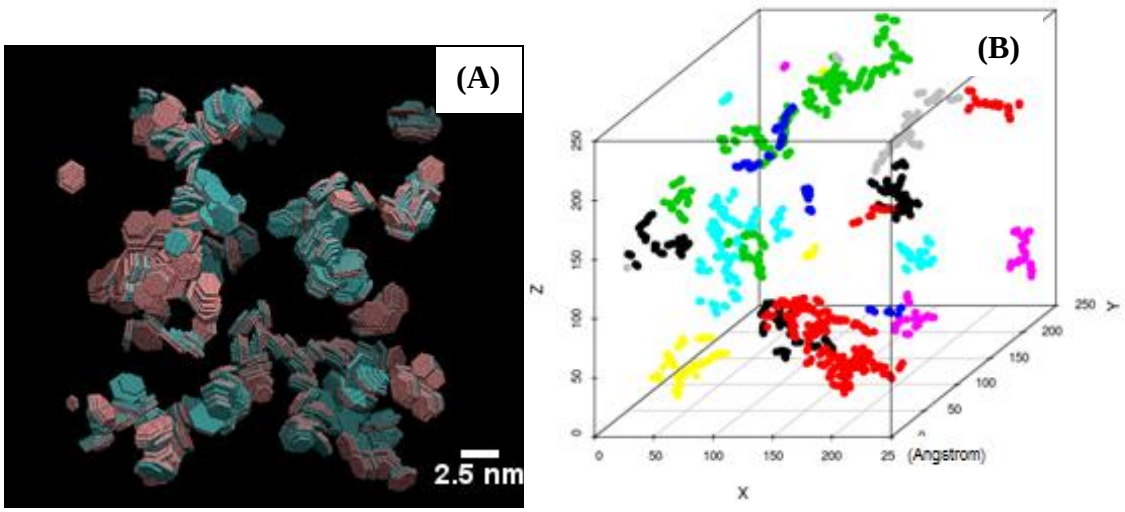

Figure 3.9. Brownian dynamics simulation of 1000 kaolinite particles at pH 5 after 30 ns simulation time: snapshot of the simulation results (A) and representation of the center of mass (C.M.) of kaolinite particles and aggregated particle structure identification (by color) (B).

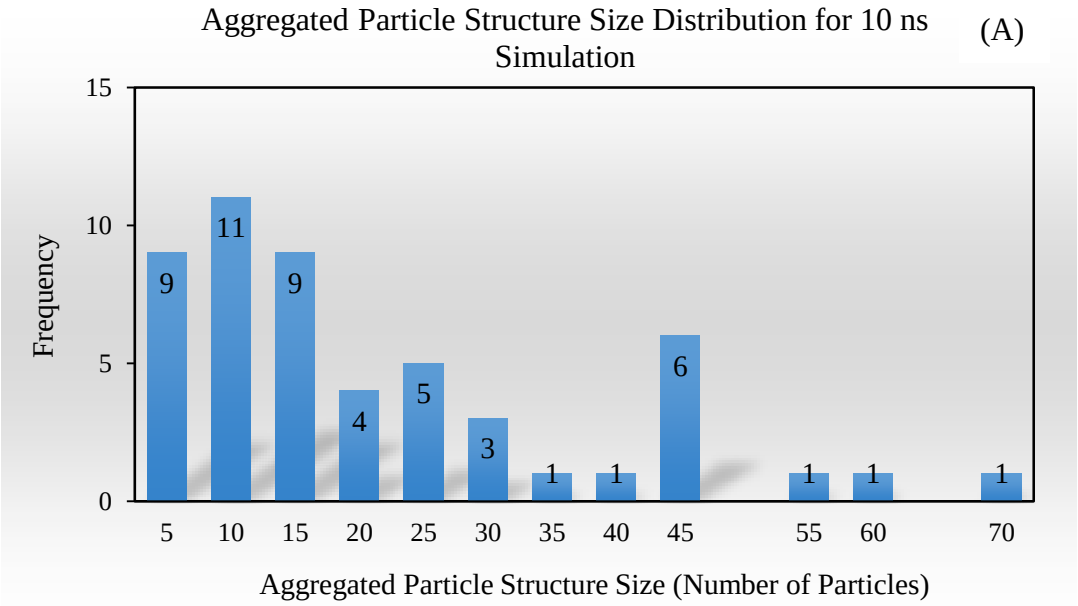

Figure 3.10. The aggregated particle structure size distribution for 10 ns simulation time (A), for 20 ns simulation time (B), and for 30 ns simulation time (C).

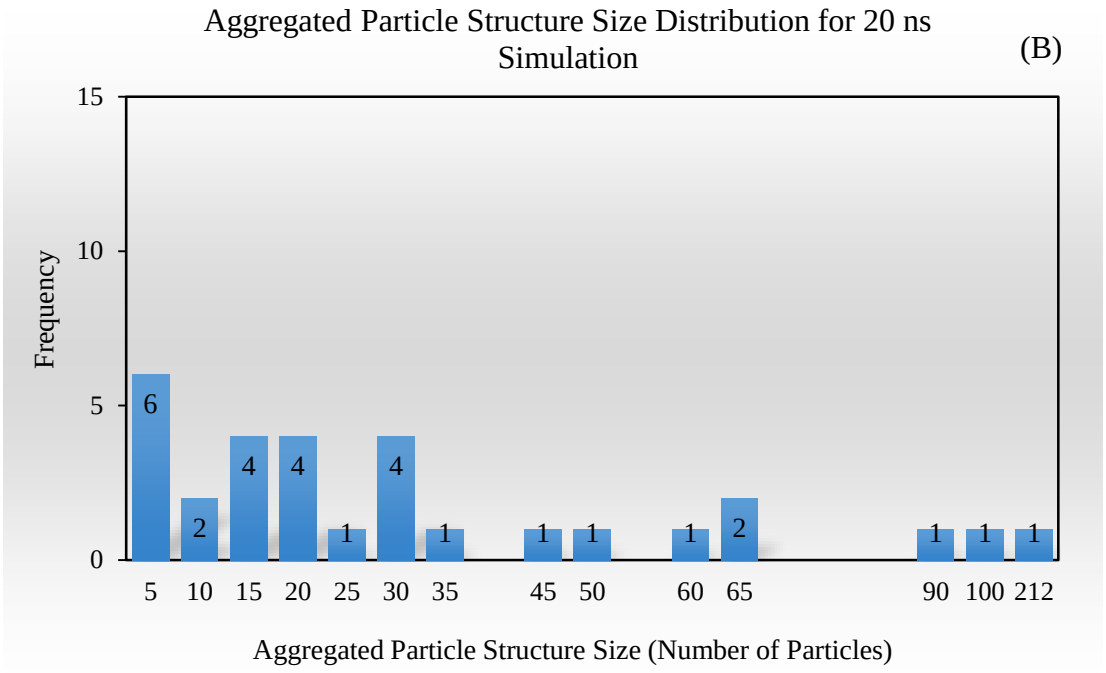

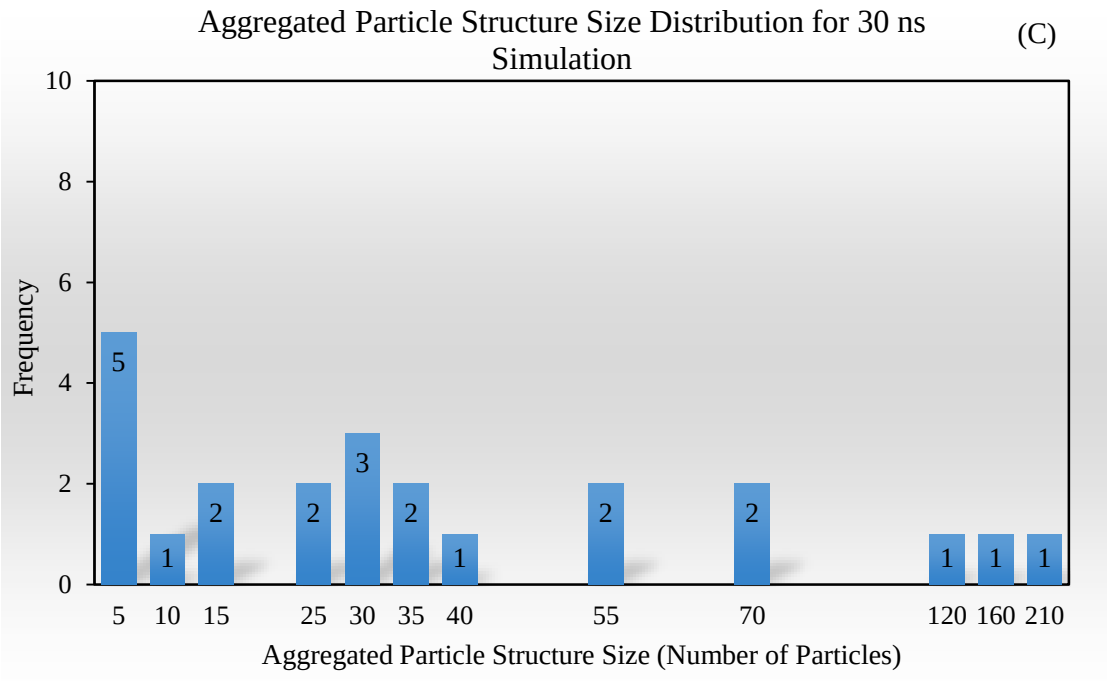

Figure 3.10. Continued

simulation time (10 ns, 20 ns, and 30 ns). A total of 47 aggregated particle structures is observed after 10 ns simulation time, and a total of 31 aggregated particle structures exist after 20 ns simulation time. The aggregated particle structures continue to coalesce and only 23 clusters remain after 30 ns simulation time. The surface areas of the aggregated kaolinite structures after 10 ns, 20 ns, and 30 ns simulation times are 258,865 $Å^2$, 236,674 $Å^2$, and 227,083 $Å^2$. The volumes of the aggregated particle structures are computed as 928,776 $Å^3$, 911,854 $Å^3$, and 897,382 $Å^3$. With increasing simulation time, both the surface area and the volume of the aggregated particle structures decrease slowly, which is another evidence indicating that the aggregated particle structures continue growing and compacting.

Representative aggregated particle structures after simulation of 10 ns, 20 ns, and 30 ns are shown in Figure 3.7, Figure 3.11, and Figure 3.12. The surface area of typical aggregated particle structures and the surface area of the silica surface and the alumina surface are presented in Table 3.3, Table 3.6, and Table 3.7. Although the growth of the aggregated particle structures results in larger surface area of individual particle structures with increasing simulation time, the percent of the silica surface and the alumina surface does not change with increasing simulation time. The constant percent of the silica/alumina surface area implies the interaction mode of kaolinite particles, namely alumina face to silica face interaction combined with alumina face to edge surface, is not a function of simulation time.

The above analysis of the simulation results indicates that the growth of the aggregated particle structures continues with increasing simulation time, although the growth rate decreases. Besides, the results also suggest that some of the small aggregated

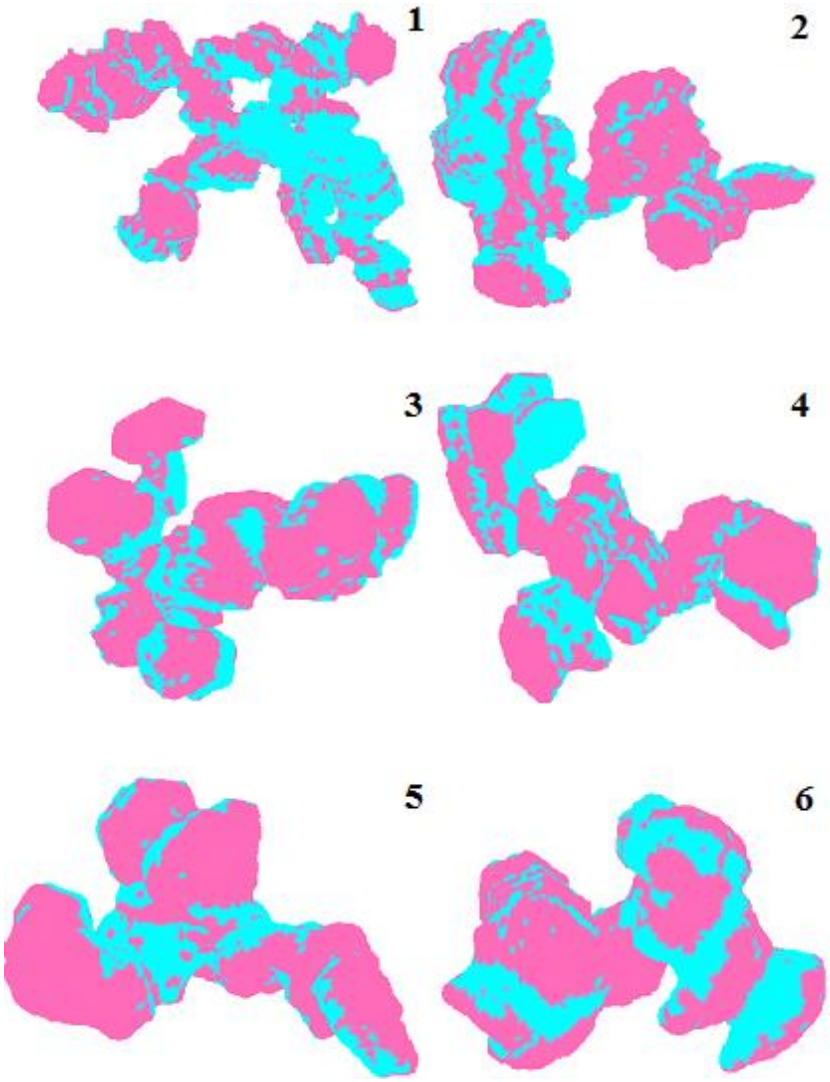

Figure 3.11. Representation of typical aggregated particle structures formed at pH 5 after 20 ns simulation time. The aggregated particle structures are filled with volumetric solids by EDTsurf method. The pink surfaces represent the silica face surfaces of kaolinite particles, and the cyan surfaces represent the alumina face surfaces of kaolinite particles.

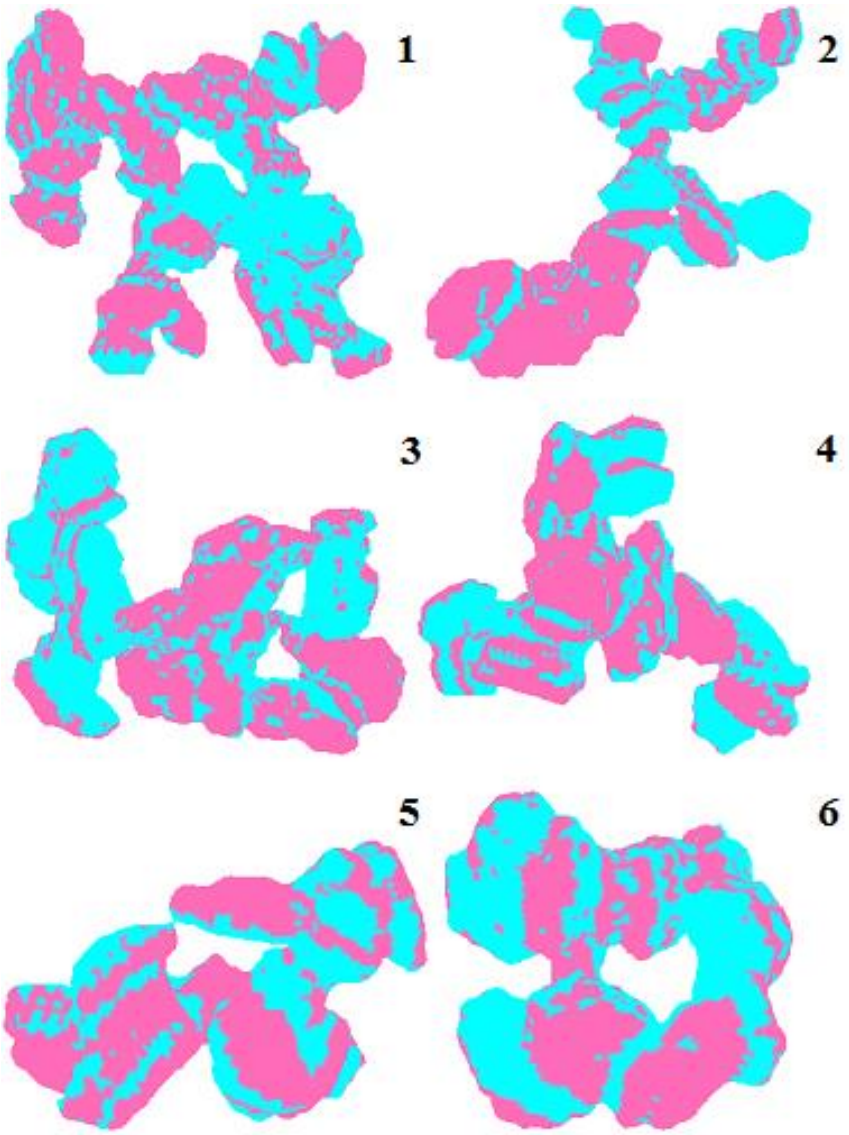

Figure 3.12. Representation of typical aggregated particle structures formed at pH 5 after 30 ns simulation time. The pink surfaces represent the silica face surfaces of kaolinite particles, and the cyan surfaces represent the alumina face surfaces of kaolinite particles.

Table 3.6. Surface area of typical aggregated particle structures after simulation for 20 ns and the surface area of the silica and alumina surfaces. The particle structure number corresponds to the number labeled in Figure 3.11.

Particle Structure Number	Surface Area of the Particle Structure ($Å^2$)	Surface Area of Silica Surface ($Å^2$)	Surface Area of Alumina Surface ($Å^2$)	% of Silica Surface	% of Alumina Surface
1	42552	23104	19449	54.3%	45.7%
2	20082	10983	9100	54.7%	45.3%
3	19501	10867	8635	55.7%	44.3%
4	18126	10052	8074	55.5%	44.5%
5	12687	6798	5890	53.6%	46.4%
6	12064	6676	5388	55.3%	44.7%
Average	/	/	/	54.9%	45.1%

Table 3.7. Surface area of typical aggregated particle structures after simulation for 30 ns and the surface area of the silica and alumina surfaces. The aggregated particle structure number corresponds to the number labeled in Figure 3.12.

Particle Structure Number	Surface Area of the Particle Structure ($Å^2$)	Surface Area of Silica Surface ($Å^2$)	Surface area of alumina surface ($Å^2$)	% of Silica Surface	% of Alumina Surface
1	39775	21507	18268	54.1%	45.9%
2	32718	17772	14946	54.3%	45.7%
3	30435	16758	13676	55.1%	44.9%
4	22612	12495	10116	55.3%	44.7%
5	12122	6631	5491	54.7%	45.3%
6	10780	6034	4745	56.0%	44.0%
Average	/	/	/	54.9%	45.1%

particle structures disappear; instead, they are combined or reorganized to larger aggregated particle structures. Generally speaking, 10 ns is long enough for traditional molecular dynamics simulation to reach an equilibrium state; however, the aggregated particle structures continuously grow and the equilibrium state has not been achieved in this study. In fact, a typical particle aggregation phenomena takes hours to reach a steady state, and in some circumstances, this steady state may not be able to be achieved in a reasonable time (days) (Likos and Lu 2001). To compute a simulation for hours would require a very powerful computer workstation and take months, even years, which is beyond the scope of this research.

3.3.4 Comparison of Simulated Viscosity with Experimental Results

Kaolinite suspensions at 1wt%, 3wt%, and 5wt% were prepared for simulation; the corresponding number of particles and volume percentages are presented in Table 3.8. Only one particle size with a total of 122 spheres per particle was used in this section in order to simplify the simulation.

The influence of particle size distribution on the aggregated particle structure was studied before simulations to determine the effect of suspension concentration on viscosity. The aggregated particle structure size distribution of 1000 mono-sized particles after simulation for 10 ns is shown in Figure 3.13. The size distribution of aggregated particle structures for mono-sized (122 spheres per particle) particles is similar to the size distribution simulated with primary kaolinite particles of 5 different sizes. The average aggregated particle structure size of mono-sized particles is slightly larger than that of particles with a size distribution as shown in Table 3.9. For mono-sized particles, the particles are easier to self-organized and form larger aggregated particle structures; in

Table 3.8. Kaolinite suspension concentration expressed both by weight, by volume, and by the number of particles for viscosity calculation by simulation. The kaolinite density is 2.6 g/cm^3.

Suspension concentration by weight	Suspension concentration by volume	Number of particles
1wt%	0.38vol%	128
3wt%	1.15vol%	384
5wt%	1.92vol%	640

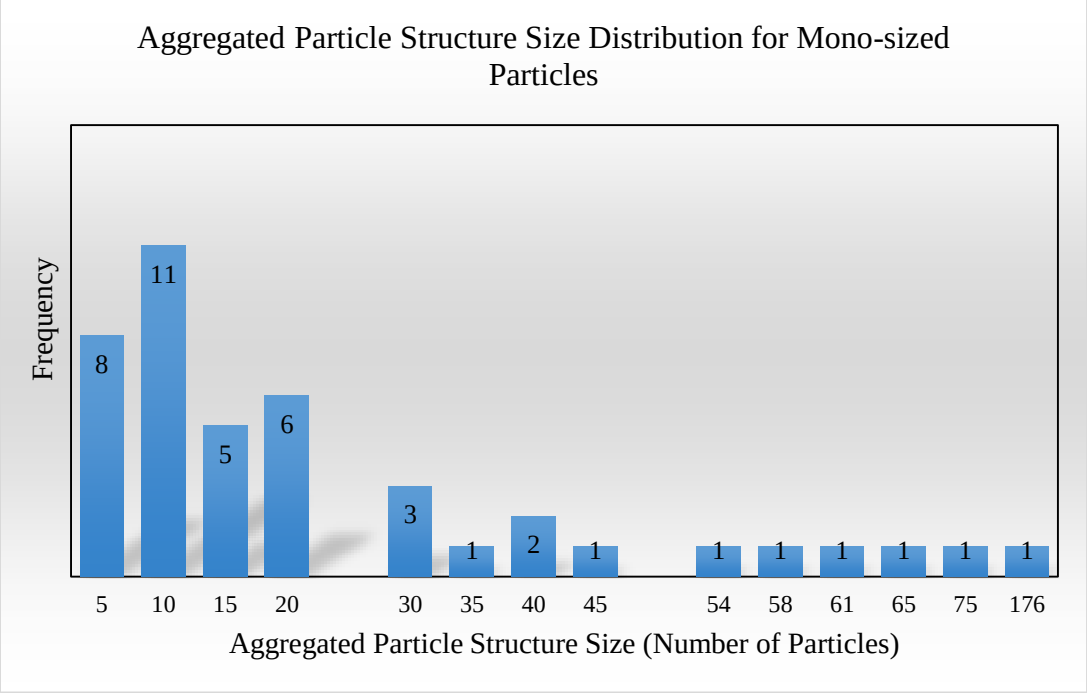

Figure 3.13. The aggregated particle structure size distribution of kaolinite suspension with 1000 mono-sized particles.

Table 3.9. Average aggregated particle structure size for the simulation with a standard particle size distribution and mono-sized particles. The mean particle size for both cases is a particle size with 122 spheres.

Primary Kaolinite Particle Size Distribution	Mean Aggregated Particle Structure (Particles/Cluster)
Standard Particle Size Distribution	19
Mono-sized Particles	23

contrast, the particles with a size distribution are misfit and less easy to form large aggregated particle structures. Overall, the aggregated particle structure formation is not significantly influenced by this variation in the primary kaolinite particle size distribution.

After 10 ns of Brownian dynamics simulation, the aggregated particle structure size was analyzed and the distributions of aggregated particle structure size for each solid concentration are presented in Figure 3.14. The results suggest that the aggregated particle structures grow larger and form more complex structure with increasing solid concentration.

An additional 1 ns was simulated for the viscosity calculation of the suspension by Green-Kubo method. The simulated results are compared with experimental data as shown in Table 3.10. A good agreement has been achieved between the simulated viscosity and the results measured by experiment, which confirms that the simulation technique can be a powerful tool to help in the analysis of experimental results for these complex suspensions.

The results also indicate that the viscosity of kaolinite suspensions at low pH is greater than the viscosity of the suspension at high pH, which is probably due to the fact that the transfer of fluid momentum at low pH is hindered by the formation of complex cluster structure. In contrast, the well-dispersed particles at high pH have a minimum contribution to flow resistance due to the free alignment of the particles in the flow (Michaels and Bolger 1964; Palomino and Santamarina 2005). As the suspension concentration increases, the viscosity of the suspension increases significantly, although the viscosity of the suspension at low pH increases faster than that at high pH. The suspension is well-dispersed at high pH, and the viscosity of the suspension increases slowly with increasing solid content. On the other hand, the more complex aggregated

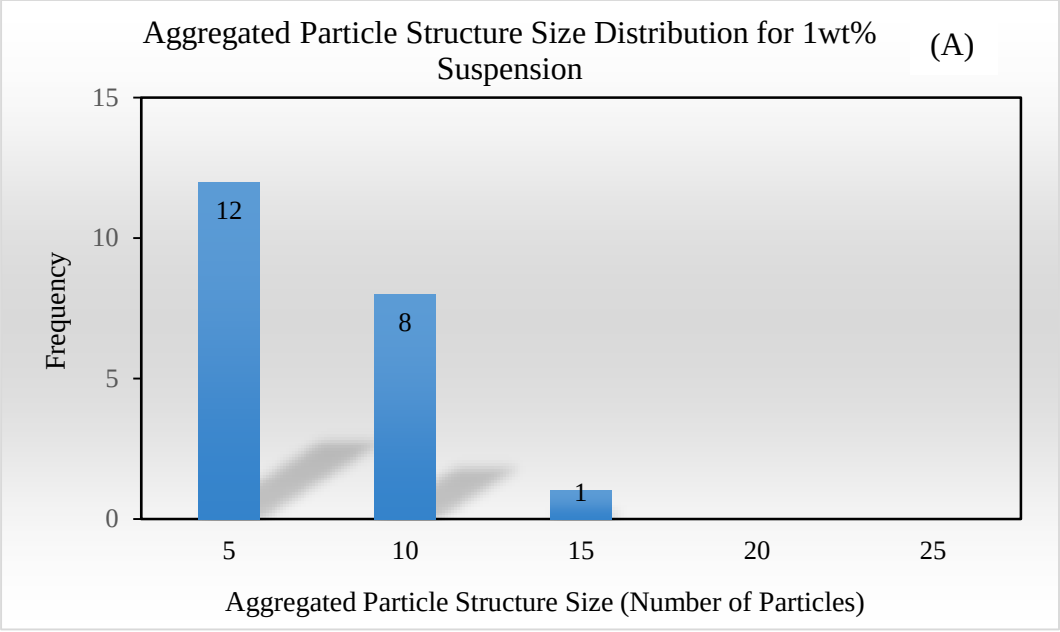

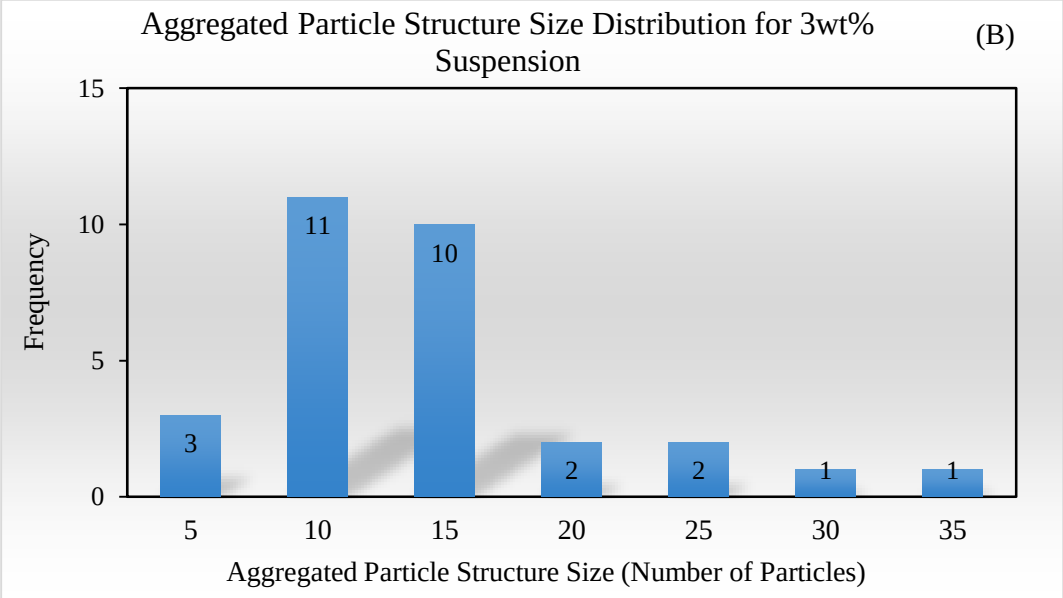

Figure 3.14. The aggregated particle structure size distribution of kaolinite suspension at pH 5 after 10 ns simulation for the following concentrations of the suspensions (A) 1wt% kaolinite suspension (B) 3wt% kaolinite suspension (C) 5wt% kaolinite suspension

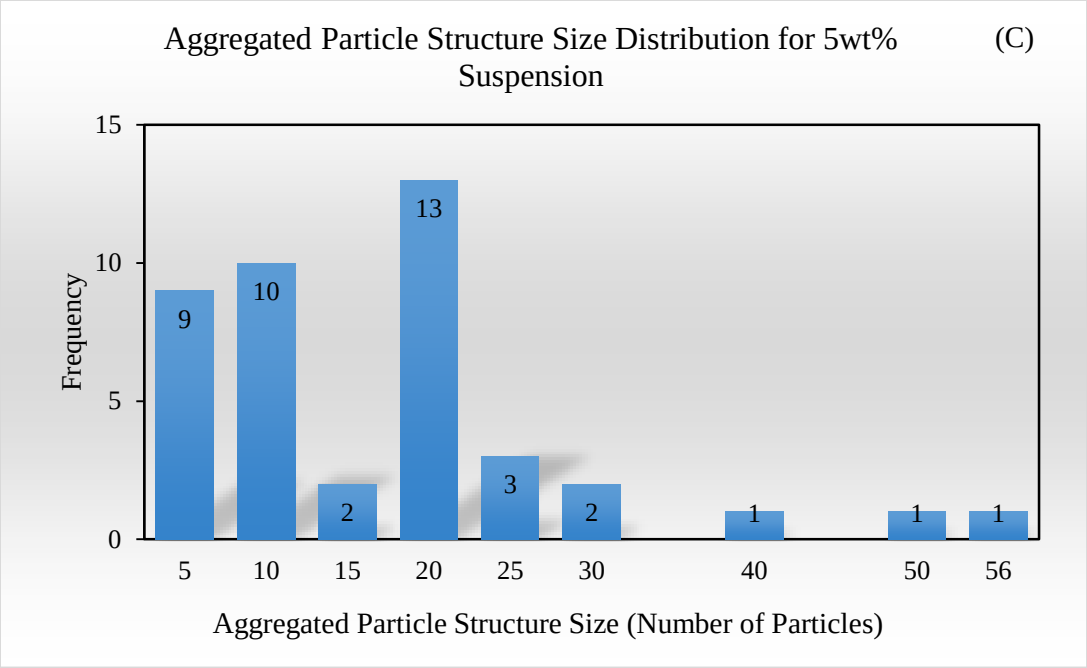

Figure 3.14. Continued

Table 3.10. Simulation results of the viscosity of kaolinite suspension as compared with experimental results.

Concentration (wt%)	pH 5 (mPa•S)		pH 8 (mPa•S)	
	Simulation	Experiment*	Simulation	Experiment*
1%	1.00	1.30	0.894	1.00
3%	3.75	2.64	2.58	1.07
5%	6.98	6.19	2.85	2.07

*(Gupta 2010)

particle structure with increasing concentration at low pH contributes to the more dramatic increase in suspension viscosity.

In addition, the particle shape effect on the viscosity has been considered by simulating spherical kaolinite particles of the same volume and the same charge properties as the hexagonal platy shape particles at pH 8. The 5% suspension with spherical particles has been simulated for 10 ns, and the viscosity was calculated using the same method (Green–Kubo) as shown in Table 3.11. The viscosity for the spherical particle suspension is much smaller than that simulated with hexagonal, platy shaped particles at pH 8. This study is consistent with that reported in the literature; the smaller the aspect ratio, the lower the viscosity of the suspension (Mueller et al. 2011).

3.3.5 Effect of Ionic Strength on Particle Interactions

The surface charge of kaolinite surfaces as a function of ionic strength (1 mM, 10 mM, and 100 mM) was modified based on the calculations from AFM surface force measurements and the results together with debye length of the electric double layer are shown in Table 3.12. The 20 ns simulation results for kaolinite suspensions at different ionic strengths are shown in Figure 3.15. The aggregated particle structure size analysis is presented in Figure 3.16. The average aggregated particle structure size (number of particles per aggregated particle structure) for suspensions with ionic strength of 1 mM, 10 mM, and 100 mM is presented in Table 3.12. The aggregated particle structure size increases with increasing ionic strength as expected due to increased surface charge density. However, the largest aggregated particle structure at 10 mM has 144 particles; in contrast, the largest aggregated particle structure at 1 mM contains 212 particles. When the ionic strength of the suspension increases to 10 mM, the repulsive and attractive electrostatic

Table 3.11. Effect of particle shape on the viscosity for 5wt% suspensions.

Particle Shape	Viscosity (mPa•S)
Hexagonal Plates	2.85
Spheres	0.109

Table 3.12. The parameters used for simulations at different ionic strength as well as the average aggregated particle structure size (number of particles) for each ionic strength.

Ionic Strength (mM)	Debye Length (Å)	Surfaces	Charge Density	Average Aggregated Particle Structure Size (Number of Particles)
1	98	Si surface	-2.0 e/sphere	33
		Al surface	0.5 e/sphere	
10	30.4	Si surface	-2.0 e/sphere	41
		Al surface	1.15 e/sphere	
100	9.6	Si surface	-4.0 e/sphere	41
		Al surface	1.2 e/sphere	

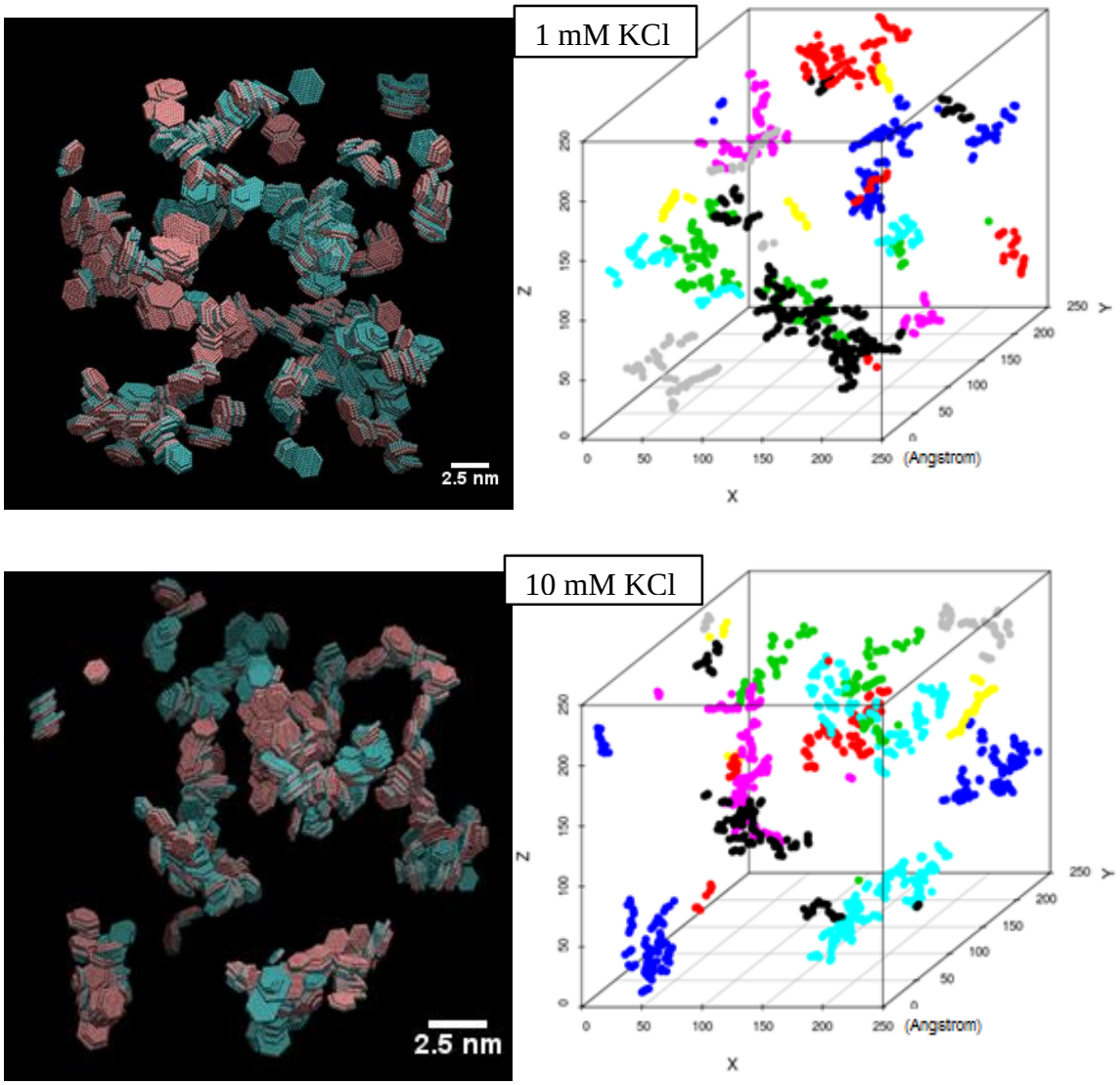

Figure 3.15. Brownian dynamics simulation snapshots of 1000 kaolinite particles as a function of ionic strength (1 mM KCl, 10 mM KCl, 100 mM KCl) at pH 5 after 20 ns simulation time (on the left); Representation of the center of mass (C.M.) of kaolinite particles and aggregated particle structure identification (by color) as a function of ionic strength (1 mM KCl, 10 mM KCl, 100 mM KCl) at pH 5 after 20 ns simulation time (on the right).

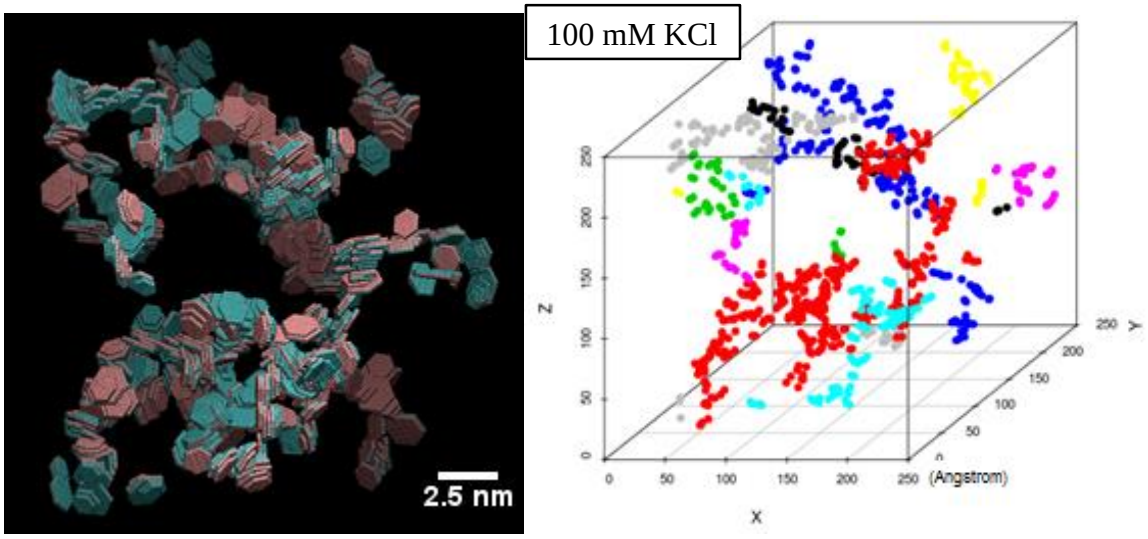

Figure 3.15. Continued

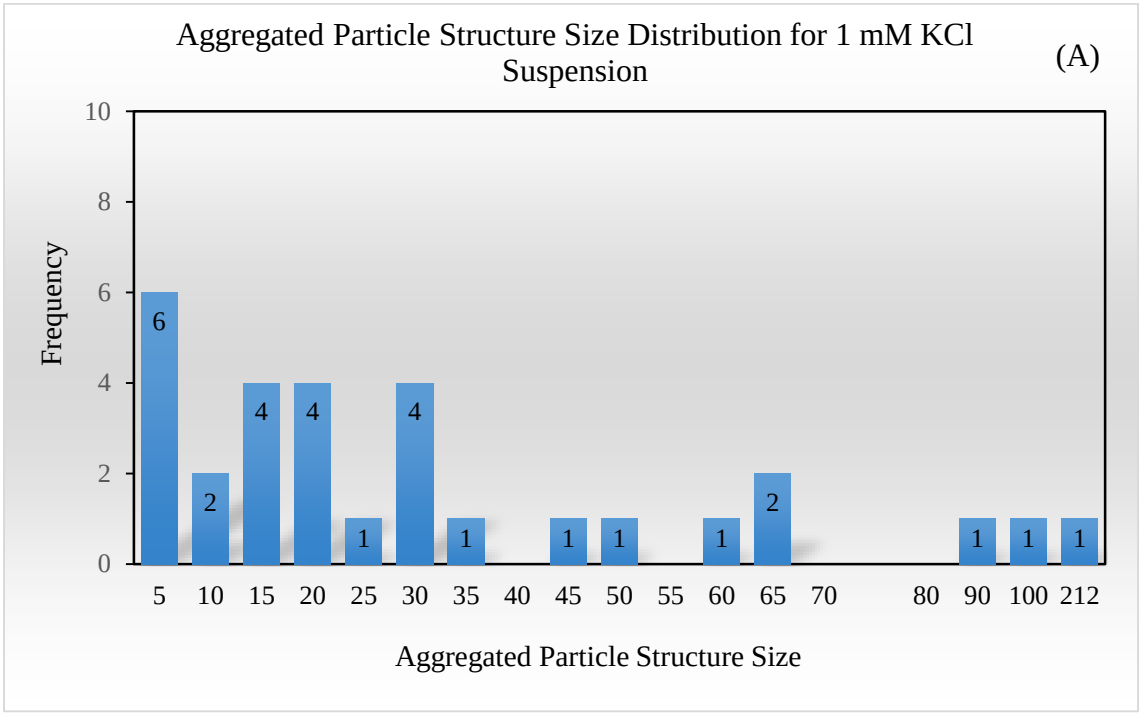

Figure 3.16. Aggregated particle structure size distributions for kaolinite suspensions with ionic strengths of 1 mM KCl, 10 mM KCl, and 100 mM KCl.

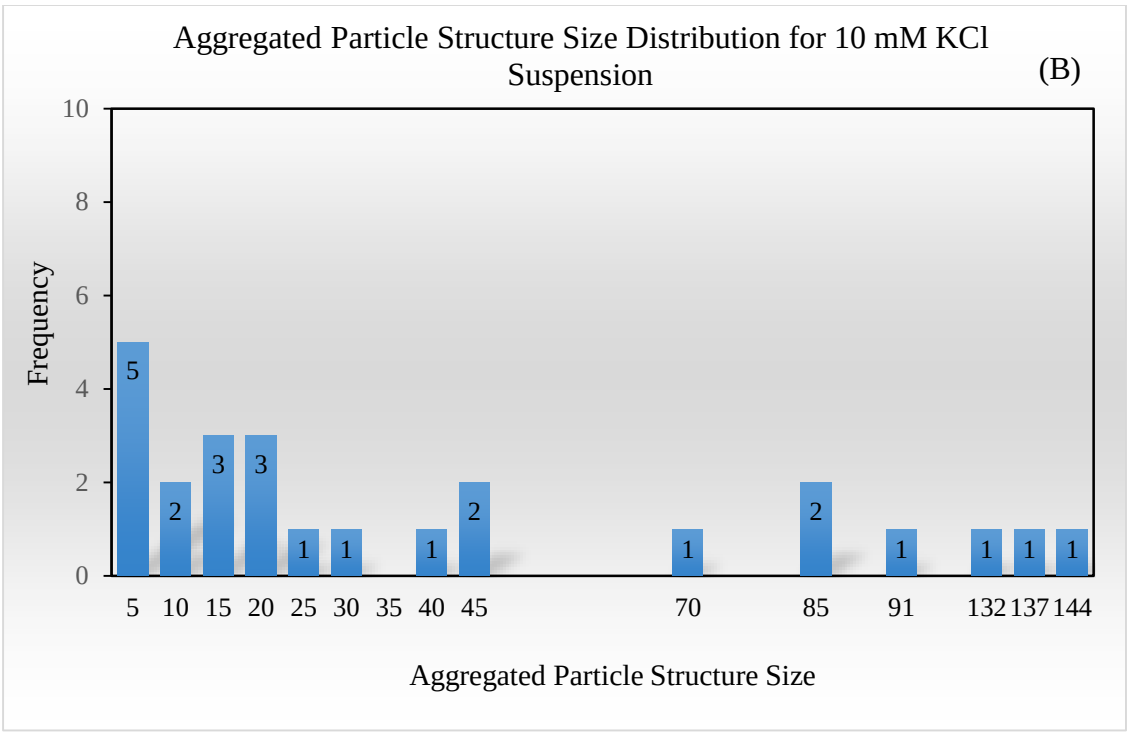

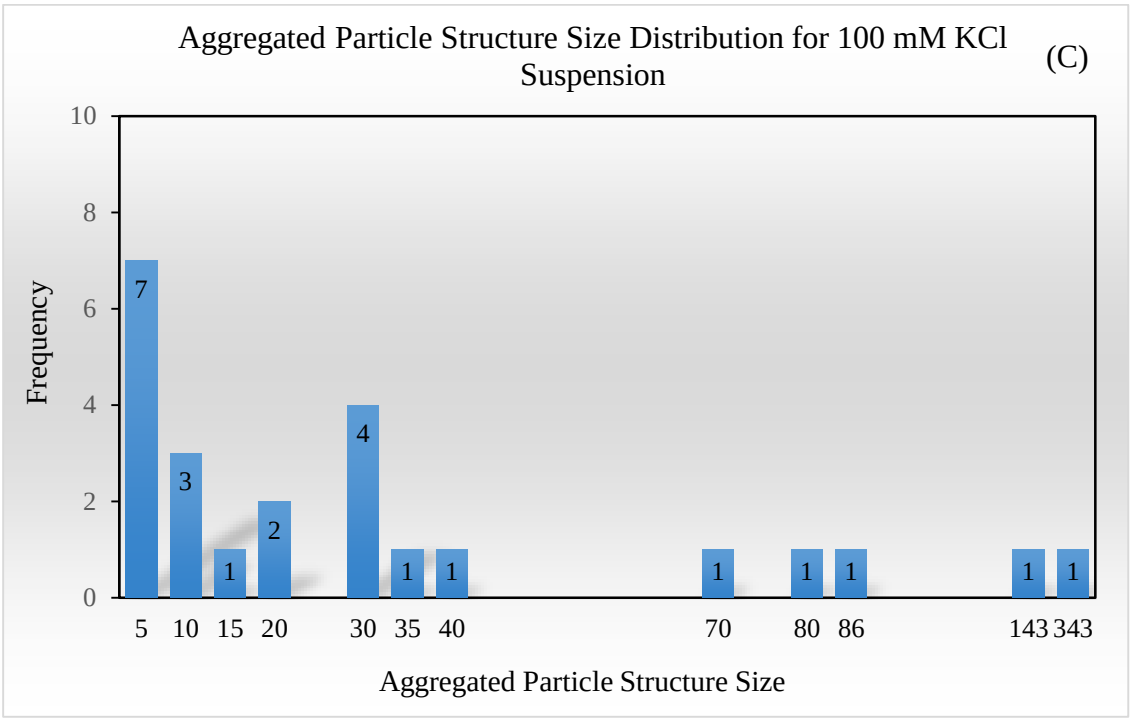

Figure 3.16. Continued

forces increase at the same time, which may account for the limitation to growth for large aggregated particle structure at 10 mM suspension.

For the 100 mM suspension, the surface charge density of the alumina face suddenly decreases, as reported in Chapter 2, which accounts for a lower attractive electrostatic force. However, because the electric double layer has been highly screened at high ionic strength, the attractive van der Waals force can be more dominant. The particles form small aggregated particle structures due to van der Waals attraction; however, after a long time (20 ns), the aggregated particle structures continue to grow slowly and occasionally can form very large aggregated particle structures (343 particles in one particle structure). In the meantime, strong repulsive electrostatic force may limit the growth of the aggregated particle structures. The competition of the electrostatic force and van der Waals force may have caused the average aggregated particle structure size to plateau for the 100 mM suspension.

3.3.6 Validation of Cluster Structure

Direct examination of clusters was done using environmental scanning electron microscopy and scanning electron spectroscopy with a WETSEM capsule, as well as examination by X-ray Micro Computed tomography.

3.3.6.1 Environmental Scanning Electron Microscopy (ESEM)

Figure 3.17 shows an ESEM image of kaolinite particles at pH 4 revealing the open structure of the cluster organization. The card-house structure, with voids of air or water with a size of about 300 nm–600 nm, is found in the image. The cluster structure is mainly formed by the stacking of layer by layer and may have some face to edge interactions as

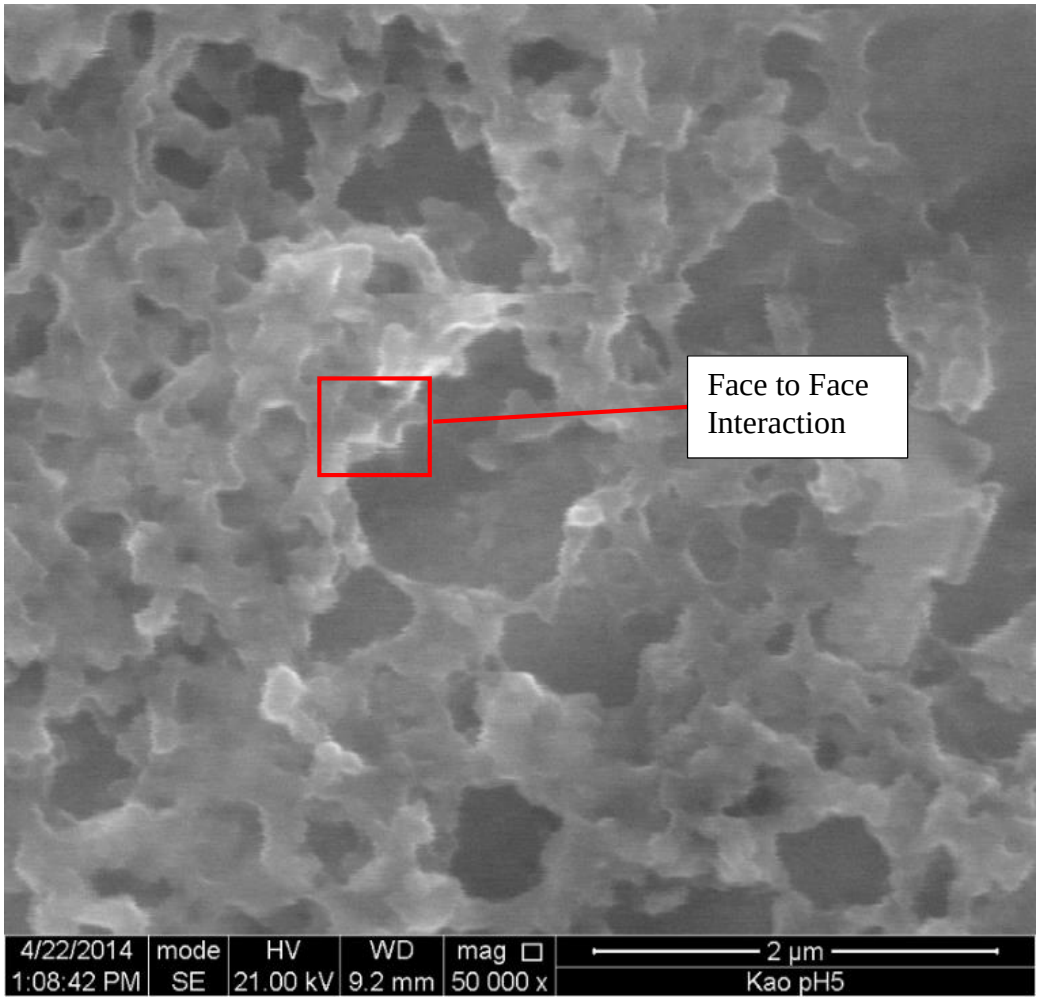

Figure 3.17. ESEM image of kaolinite particles at pH 5 revealing the open structure of clusters and surface interactions.

well. The primary particles are not so easy to be identified due to the limitation of ESEM resolution, but the cluster structure shows good consistency with the simulation results. Typical face to face interactions are marked in Figure 3.17; however, the face to edge interactions have not been identified due to the low resolution. However, a highly concentrated suspension (~50wt%) was exposed to the SEM chamber directly during the ESEM imaging, and there are concerns that the suspension may have dehydrated when taking the images.

3.3.6.2 SEM Imaging with WETSEM Capsules

A small amount (~15μl) of kaolinite suspension (~50wt%) was injected to WETSEM capsules for SEM imaging at high vacuum. The electrons penetrate the specially designed membrane of the WETSEM capsule and the image of the wet kaolinite clusters underneath the membrane is acquired. The kaolinite face to face interaction and face to edge interaction are observed in Figure 3.18 (A), forming complex clusters in the suspension at low pH (pH 4.3).

Note that the gray-level variation in contrast which is attributed to the energy decay when the electrons penetrate the water suspension, although the bright white section of the suspension may have dehydrated. The primary particles of kaolinite are better defined when compared to the ESEM image presented in Section 3.3.6.1; however, an image with higher magnification cannot be achieved due to the difficulty of imaging in water with SEM. In spite of frustration with these experiments, the complex cluster structure is observed at low pH and open water regions in the cluster structures are evident. The SEM cluster size varies from 1.5 μm to 10 μm. The average cluster size measured by photon correlation spectroscopy (PCS) is about 1.5 μm to 2 μm at pH 4–5, as reported in Chapter

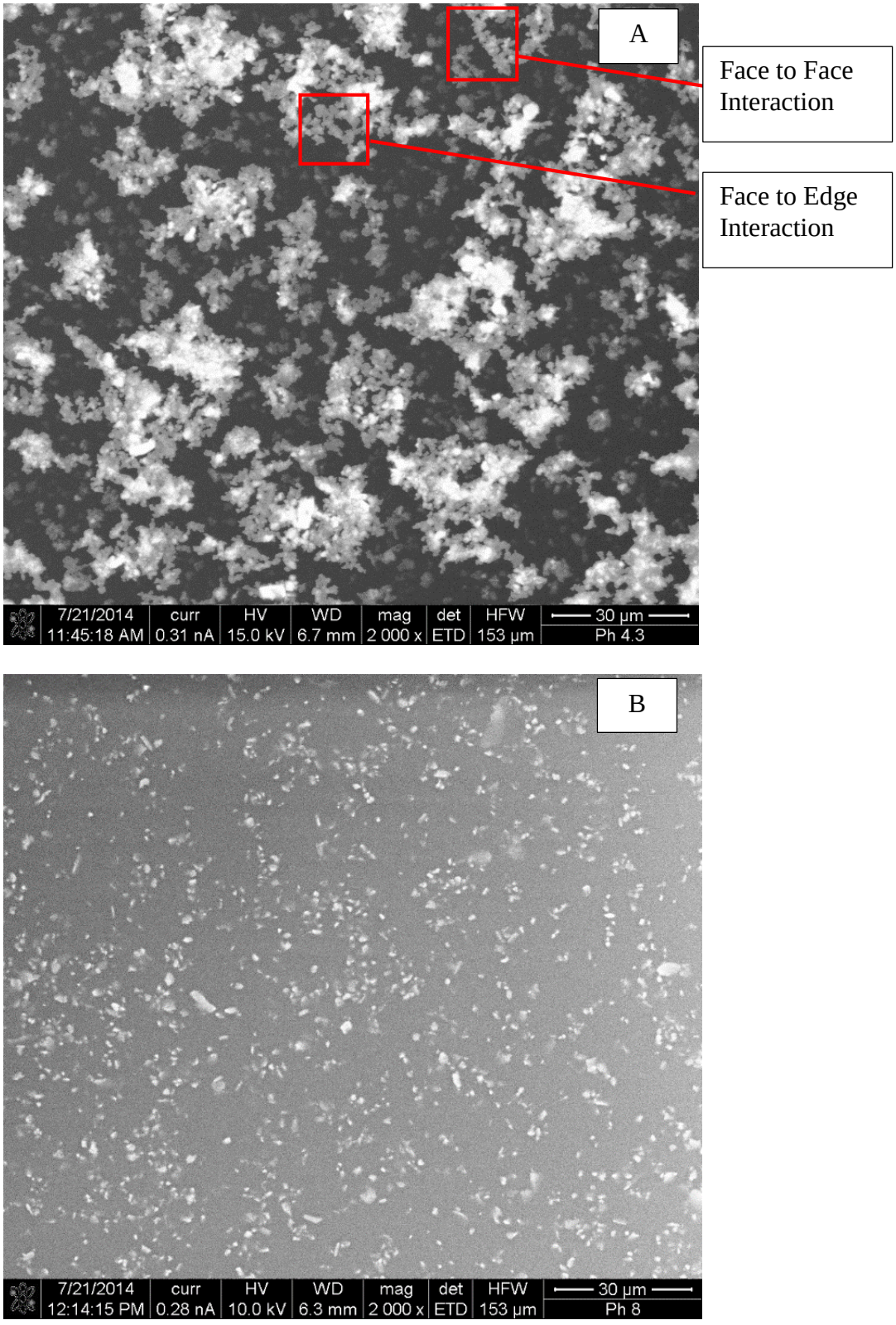

Figure 3.18. SEM images of kaolinite suspension in WETSEM cells at pH 4.3 (A) and pH 8.1 (B).

2 as well as in the literature (Gupta et al. 2011). In fact, attention should be paid that the formation of clusters is dynamic and the positions of particles/clusters are time-dependent. For example, two closely packed clusters can be counted as one cluster during one time frame, but the two clusters will separate and be counted as two in the next time frame. In this case, the determination of nonspherical cluster size relying on one snapshot is difficult and arbitrary. The dynamic motion and miscounting of close clusters may account for the large variation of the results acquired by SEM imaging. In contrast to the results at pH 5, the particles are well-dispersed and suspended at pH 8, as shown in Figure 3.18 (B). In summary, the experimental results reach good agreement with the simulation results.

3.3.6.3 X-ray Micro Computed Tomography

At pH 4, the sediment of a kaolinite suspension was scanned by X-ray micro CT, and the reconstructed image is shown in Figure 3.19. Chains composed of clusters about 2–5 microns in size are observed in the image. The chains are worm-like structures with surrounding water. In addition, the solids percent of this sediment is estimated to be 48.2% using the ImageJ software, highly consistent with what was observed from the simulation results (48.4%).

It is believed that initially, elementary clusters are formed from a suspension of primary kaolinite particles ~0.5 microns in size. The clusters have a size of 2–5 microns, which has been measured by photon correlation spectroscopy (see Figure 2.18) and confirmed from the X-ray micro CT image (Figure 3.19). Most interesting is that on sedimentation, the clusters string together to form chain structures with a length that varies from 10 to 50 microns. Some further evidence of chain formation is seen from close examination of the SEM image presented in Figure 3.18 (A). It is expected that the chains

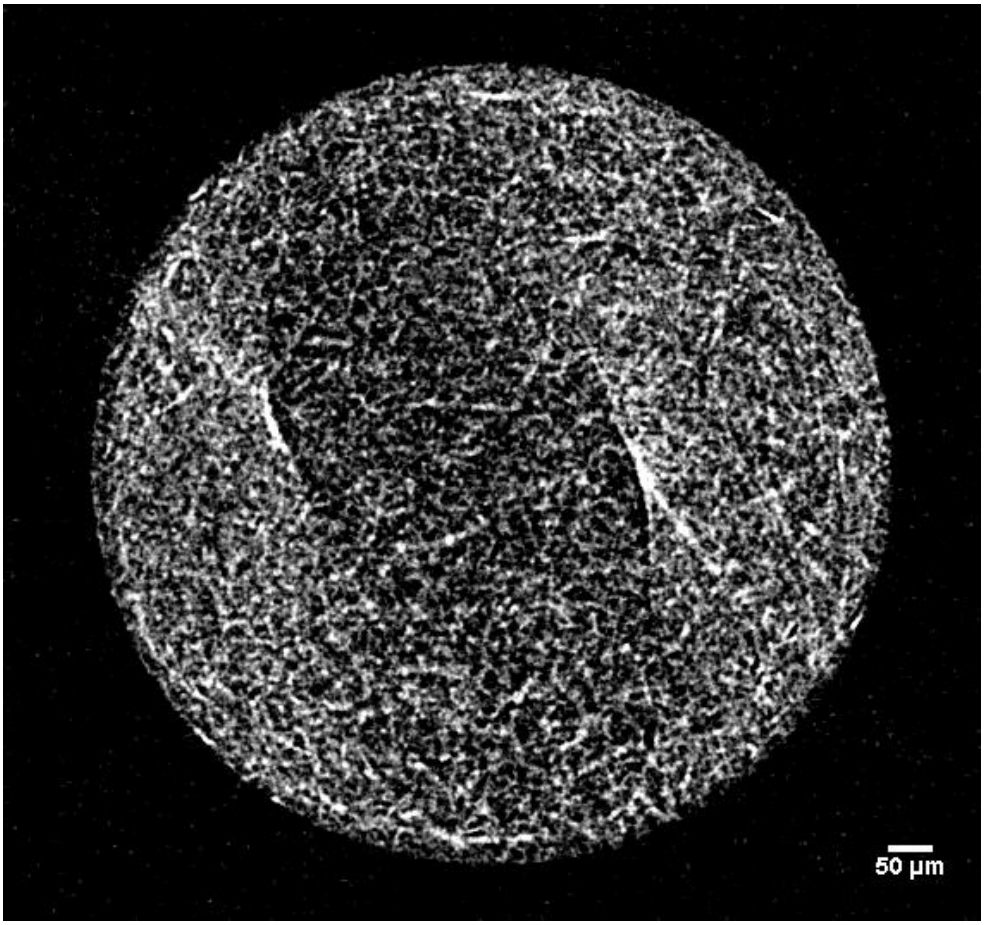

Figure 3.19. Thin section (1.85 µm) of sedimented kaolinite clusters (white structure) at pH 4 as revealed from 3D X-ray Micro Computed Tomography image.

are formed by weak interaction between those elementary clusters. The reason that photon correlation spectroscopy (PCS) failed to detect these kaolinite chain structures is probably due to the limitation of the instrumentation as well as the fact that the chain structures are most likely formed during the consolidation of kaolinite suspension, and are not stable in suspension, which is the case for the measurements by PCS. Unfortunately, XMT with a resolution of 2 microns is not sufficient to observe more detail of the elementary clusters and the chain structures. Further research using nano CT with a resolution ~50 nm should be able to improve the image detail and help to further describe the elementary clusters and the chain structures.

It is recognized that images acquired by either ESEM imaging or SEM imaging with a WETSEM cell provide good validation of the cluster structures for the simulation, as discussed in Section 3.3.6.1 and 3.3.6.2. However, the image analysis is limited by the 2D projection of SEM images, which suggests that the overlaid cluster structures can be misleading in terms of their overall geometry; more importantly, it is unable to describe chain structures as observed by X-ray Micro Computed Tomography. In XMT, three-dimensional images are taken and a thin section of the reconstructed images is shown in Figure 3.19. In this case, X-ray CT is better able to describe the geometry and orientation of the chain structures.

3.4 Summary

A new coarse-grained model was developed for the simulation of anisotropic kaolinite particle interactions. Based on AFM experimental results, electrostatic and van der Waals forces acting on kaolinite particle surfaces were considered for simulation using the coarse-grained model. Results have shown that at low pH (pH 5), aggregated particle

structures of large size are formed by particle stacking due to alumina face to silica face interaction and due to alumina face to edge surface interaction. As a result, 10% more silica face surfaces are exposed at the aggregated particle structure surface. In this regard, the exposed surfaces of the aggregated particle structures are more negatively charged. This finding will be an important consideration in discussion of kaolinite flotation given in Chapter 4. The cluster structure was analyzed and found to contain 48.4% solids on average, which was verified by X-ray Micro Computed Tomography images.

The simulation time has been found to be an important factor which influences the aggregated particle structure/cluster structure. The aggregation of kaolinite particles continued with increasing simulation time, but the growth rate of the aggregated particle structures decreased with the time of simulation.

The effect of ionic strength on particle interactions was studied and the results indicate that the aggregated particle structure size increased with increasing ionic strength, and reached a plateau at 100 mM suspension due to the competition between electrostatic forces and van der Waals forces.

The simulated viscosity of kaolinite suspensions at 1%wt, 3wt%, and 5wt% solids was calculated by the Green-Kubo model and the results were consistent with experimental data reported in the literature. Larger and more complex aggregated particle structures formed with increasing particle concentration which accounted for the significant increase in the suspension viscosity at low pH.

Finally, experimental validation of the cluster structure was accomplished with ESEM imaging as well as SEM imaging with a WETSEM capsule. Both techniques revealed an open structure of the clusters at low pH. Face to face stacking and face to edge

interactions were observed in the case of SEM imaging. The dispersed state of kaolinite suspension at high pH was verified by SEM imaging as well. The experimental results confirm the results obtained by simulation. In addition, the formation of elementary cluster structures was revealed from X-ray Micro Computed Tomography images. Finally, the aggregation of clusters into linear (chains) structures was found to occur in the kaolinite sediment.

CHAPTER 4

ANALYSIS OF THE REVERSE FLOTATION OF KAOLINITE FROM BAUXITE WITH DODECYL AMINE COLLECTOR

4.1 Introduction

Froth flotation has been considered as one of the most widely applied and efficient technologies for the recovery of mineral resources. Kaolinite exists as a common gangue mineral in many valuable ore deposits, including bauxite, potash ore, iron ore, sulfide ores, oil sands, phosphate, and rare earth ores. In some cases, it is desired to depress kaolinite during flotation while in other cases, the kaolinite is removed by reverse flotation. Of particular interest is the development of flotation for the removal of kaolinite from low-grade bauxite ores. The key result of the bauxite research was the opening of the first bauxite mineral processing plant in China (and in the world) in 2002 which uses direct flotation to prepare bauxite for the Bayer process (Zhao et al. 2010). One million tons/yr of bauxite ore can be treated at this plant. Now more than 80% of the two billion tons of low grade diasporic bauxite in China can be used instead of being discarded, extending the usable amount of bauxite resources for the China aluminum industry from only about 10 years to more than 50 years. Another significant bauxite reserve (~10%) is located in Brazil (Bray 2014). Although extensive research has been done for the flotation of Brazilian bauxite, the flotation practice is still new and not yet practiced in the Brazilian bauxite

industry (Bittencourt et al. 1990; Massola et al. 2007). To understand and develop the future industrial practice of bauxite flotation, the nature of kaolinite flotation is discussed based on surface/colloid chemistry results reported in previous chapters.

In spite of the difficulty in the development of technology for the flotation of fine particles, such as kaolinite, some success has been achieved. Both direct flotation and reverse flotation processes have been developed for bauxite flotation (Marino 2012). For direct flotation of low grade bauxite ore, gibbsite or diaspore is floated with the hydroxamate collector at high pH (pH 9–10); in the meantime, the silicate minerals (kaolinite) are depressed by sodium silicate and iron oxide minerals are depressed by starch. On the other hand, in the case of the reverse flotation process for low grade bauxite ore, the silicate minerals (kaolinite) are floated with amine and the bauxite minerals gibbsite and/or diaspore are depressed with starch at low pH (pH 4–5). Recent studies have suggested that reverse flotation is economically favored over the direct flotation process (Xu et al. 2004; Zhao et al. 2010), due to the fact that 1) clays (kaolinite) are easier to be liberated than bauxite, thus significant energy for the grinding process is expected to be saved in reverse flotation and 2) hydroxamate collectors used for direct flotation are much more expensive than the amine collector used for reverse flotation. In addition, the hydroxamate collector consumption is greater due to the greater amount of gibbsite/diaspore when compared to the clay minerals in the bauxite ore.

Extensive research has been conducted to improve the flotation of kaolinite from bauxite, including the development of new collectors, adjustment of pH and ionic strength, and design of the flocculation–flotation process (Bittencourt et al. 1990; Hu et al. 2004; Hu et al. 2005; Zhong et al. 2008; Ma et al. 2009; Marino 2012). Yuehua Hu has led his team

and made significant contribution to the study of reverse flotation of low-grade bauxite, efforts including the development of new collectors as well as the study of kaolinite reverse flotation mechanism (Hu et al. 2001; Hu et al. 2003; Hu et al. 2004; Hu et al. 2005; Zhong et al. 2008; Liu et al. 2009). Recently, many researchers are dedicated to developing new cationic collectors which can improve the flotation behavior of kaolinite from bauxite, and a large variety of the collector types have been investigated, such as primary amine (dodecyl amine), tertiary amine (DEN, DPN, DBN), quaternary amine (CTAB, DTAC, CTAC), n-(2-aminoethyl)-dodecanamide, n-(3-aminoprpyl)-dodecanamide, and N,N-dipropyl dodecyl amine (PN) (Hu et al. 2003; Zhao 2003; Zhao et al. 2003; Liu et al. 2009; Xia et al. 2009; Jiang et al. 2011; Liu et al. 2011). Primary amine is one of the most common collectors used in reverse flotation, and the recovery of kaolinite from bauxite is ~70%. Newly developed collectors mentioned earlier can improve the recovery to as high as 80–90%. Additionally, it has been demonstrated that the flotation recovery of kaolinite is significantly increased by decreasing the pH of the slurry flotation (Bittencourt et al. 1990; Hu et al. 2003; Hu et al. 2005).

However, the nature of kaolinite flotation using cationic collectors (alkyl amines) is not well understood. The mystery lies in the fact that half of the particles surfaces (alumina surfaces) of kaolinite particles are exactly the same as gibbsite surfaces in crystal structure and surface properties. Nevertheless, kaolinite particles are able to be separated from gibbsite particles by amine flotation at low pH (pH <5). Simulation results have suggested that dodecyl amine prefers adsorption at the silica face surface of kaolinite over the alumina face surface (Hu et al. 2005). However, a reasonable explanation for the better flotation recovery of kaolinite in acidic solution has not been reported in the literature.

Only recently has the detailed surface chemistry of kaolinite particles been established. As discussed in Chapters 2 and 3, the alumina face surfaces of kaolinite particles are positively charged, and the silica face surface and the edge surface are negatively charged even in acidic solution, as discussed in Chapter 2 (Gupta and Miller 2010; Liu et al. 2014). In addition, the kaolinite particle interaction has been studied in Chapter 3. These current and previous surface chemistry studies of kaolinite particles provide fundamental knowledge for the analysis of the flotation behavior of kaolinite particles with the dodecyl amine collector.

The interaction between two basal plane surfaces of kaolinite particles and dodecyl amine is investigated in this chapter. Due to difficulty in the study of fine kaolinite particles (~500 nm), model surfaces with similar properties to the two face surfaces of kaolinite have been used to describe the flotation behavior of kaolinite. The basal plane surface of pyrophyllite, a trilayer phyllosilicate, was selected to represent the silica face surface of kaolinite; gibbsite, an aluminum hydroxide mineral with octahedral structure, was used to represent of the alumina face surfaces of kaolinite particles. The pyrophyllite basal plane surface and the gibbsite octahedral surface are good candidates as model surfaces for the silica surface and alumina surface of kaolinite because of their structures. In addition, the surface charge and wettability of the pyrophyllite basal plane surface and gibbsite surface compare favorably to the properties of the silica face surface and the alumina face surface for kaolinite and are summarized in Table 4.1. It is evident that good agreement is found between the model surfaces and kaolinite face surfaces. On this basis, the pyrophyllite basal plane surface and the gibbsite surface were selected to be the model surfaces for the silica face surface and alumina face surface of kaolinite.

Table 4.1. Surface charge and wettability of pyrophyllite and gibbsite in comparison with the silica face surface and alumina face surface of kaolinite.

Surfaces	Point of Zero Charge	Wetting Characteristics
Pyrophyllite Basal Plane Surface	<pH 3 (Hu et al. 2003)	Surface, 40-50 °(Hu et al. 2003) Powder, 79.2 °(Giese et al. 1991)
Silica Face of Kaolinite	<pH 4 (Gupta and Miller 2010)	Relatively hydrophobic (Yin et al. 2012)
Gibbsite Surface	pH 7.5-11.3 (Jodin et al. 2005; Kosmulski 2009; Adekola et al. 2011)	Hydrophilic (this study)
Alumina Face of Kaolinite	pH 6-8 (Gupta and Miller 2010)	Hydrophilic (Yin et al. 2012)

Dodecyl amine, one of the most common amines used for the flotation of kaolinite from bauxite, has been chosen as the collector for this flotation study. The interactions between the model surfaces and dodecyl amine collector are studied and based on these results, the interaction of dodecyl amine with kaolinite surfaces is suggested. In addition, the flotation mechanism of kaolinite from bauxite is analyzed and clarified based on the kaolinite surface properties, particle interaction, and the interaction between kaolinite surfaces and dodecyl amine. These results should provide a fundamental foundation for the future development of new flotation technology, including flotation conditions, control,

and evolving new chemicals for the reverse flotation of kaolinite from low grade bauxite ores.

4.2 Materials and Methods

4.2.1 Materials

A pure and white gibbsite specimen was purchased from Ward's science. The sample was polished to a very smooth surface. The gibbsite sample was cleaned with ethanol alcohol and high purity Milli-Q water (Millipore Inc.), followed by plasma cleaning for 20 minutes.

The pyrophyllite sample was obtained from a collection in the Department of Geology, University of Utah. The basal plane of pyrophyllite was polished to a flat surface and then, a fresh surface was acquired by peeling off several layers of pyrophyllite using adhesive tape.

The collector, dodecyl amine hydrochloride, was purchased from Sigma Aldrich, with a purity of 99.5%. The following concentrations of the dodecyl amine collector were prepared for contact angle measurements, 1×10^{-5} M, 5×10^{-5} M, 1×10^{-4} M, and 2×10^{-4} M. The pH was varied from pH 3 to pH 10. The fresh surface of gibbsite or pyrophyllite was conditioned in the collector solution at the desired concentration for 30 minutes before contact angle measurements were made. The captive bubble contact angles for gibbsite and pyrophyllite were measured at each condition.

4.2.2 X-ray Diffraction

The mineralogy of the two samples was verified by X-ray diffraction (XRD). XRD is a technique used to identify the crystal structure. An incident X-ray will be diffracted by

atoms in the crystal lattice. By measuring the scattered angle and intensity of the X-ray beam, the mean position of particular atomic planes in the crystal can be determined by Bragg's law as described in the following equation (Bragg and Bragg 1913).

$$n\lambda = 2d\sin\theta \tag{4-1}$$

Where n is an integer, λ is the wavelength of incident beam, d is the spacing between the planes in the atomic lattice, and θ is the angle between the incident ray and the scattering planes.

A piece of the gibbsite sample was used for XRD analysis of the mineral surface. For the case of pyrophyllite, the sample was treated as follows. A small amount of pyrophyllite powder was acquired by grinding the sample with an agate mortar and a pestle. Two XRD experiments were used for analysis of the pyrophyllite sample. First, XRD was conducted with the pyrophyllite powder, smeared on a glass slide by ethanol alcohol. Second, a portion of the pyrophyllite sample was exposed to ethylene glycol at 60 ℃ for 24 hours and then analyzed by XRD. The purpose of the second treatment is to determine if any swelling clay is in the pyrophyllite sample.

4.2.3 Zeta Potential Measurements

The zeta potential of the gibbsite sample was measured by electrophoresis (ZetaPALS, Brookhaven Instrument Corp.). The particle suspension was prepared at the desired solution concentration (0.05% by weight), and placed in between the two electrodes. The particle mobility was measured when the electric field was applied and converted to zeta-potential (ξ) using Smoluchowski's equation as follows:

$$U = \frac{\varepsilon\xi}{4\pi\eta}E_{\infty} \tag{4-2}$$

Where E_∞ is the applied electric field, and U is the particle velocity in a fluid with dielectric constant ε and viscosity η.

4.2.4 Contact Angle Measurements

The equilibrium contact angles for gibbsite and pyrophyllite surfaces were measured as a function of pH and the dodecyl amine collector concentration using the captive bubble method. The contact angle goniometer was used and the results of at least 5 individual bubbles were recorded for each measurement. The average of multiple measurements was calculated.

It is usually expected that the captive bubble method achieves better approximation for the surface hydrophobicity of mineral surfaces in flotation compared to the sessile drop method. In addition, the equilibrium contact angles, which are measured to describe the hydrophobicity of model surfaces, are expected to be between the corresponding advancing and receding contact angles.

4.3 Results and Discussion

4.3.1 Characterization of Gibbsite and Pyrophyllite Samples

The mineralogy of the two samples was confirmed to be gibbsite and pyrophyllite by XRD (see Figure 4.1 and Figure 4.2). The intensity peaks of gibbsite were an excellent match of the intensity peaks acquired from the database. Silver powder was introduced during preparation of the gibbsite sample in order to isolate surface areas of interest. It was found that the mineralogy of gibbsite sample from different areas remains the same.

For the case of pyrophyllite, consistent XRD results were observed between the ethanol alcohol smeared sample and the ethylene glycol smeared sample. These results

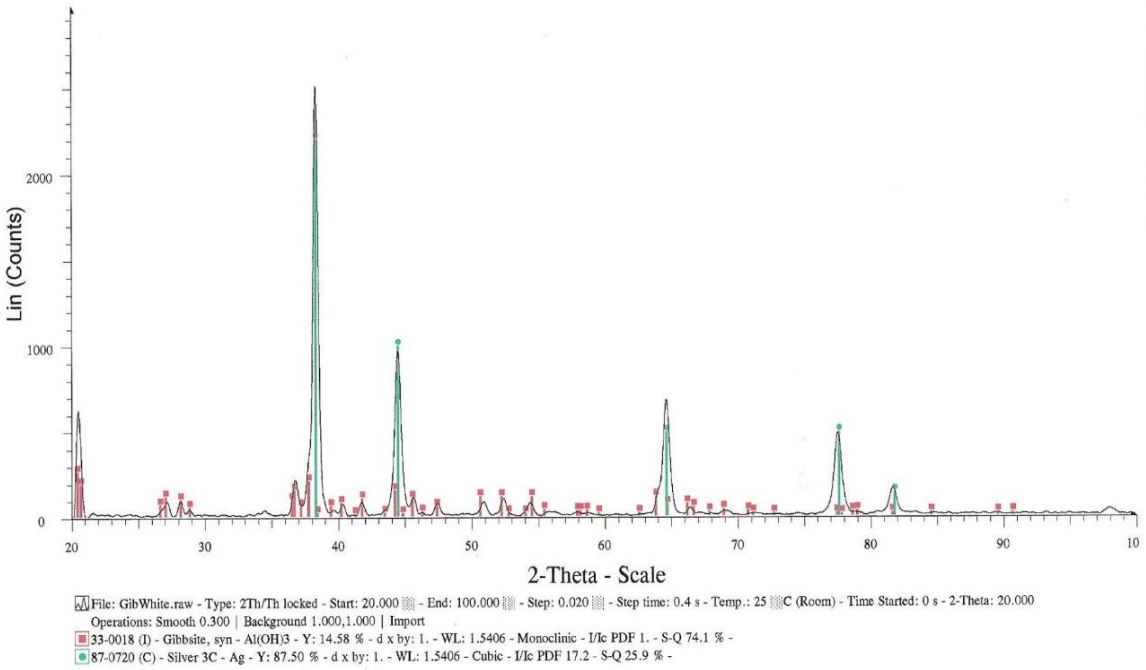

Figure 4.1. XRD spectra of gibbsite sample.

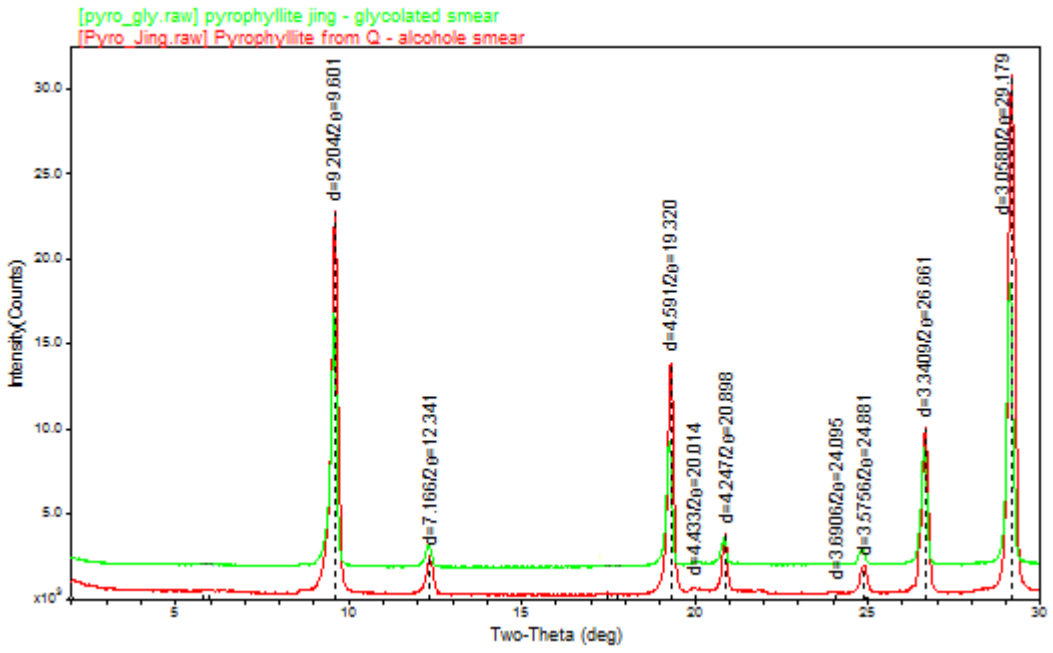

Figure 4.2. XRD spectra of pyrophyllite sample with the glass slide preparation smeared by both ethanol alcohol (red line) and ethylene glycol (green line).

indicate that there is no swelling clay in the pyrophyllite sample. The intensity peak at 2θ of 9.6 °with a c-spacing of 9.2 Å is indicative of the 001 basal plane of pyrophyllite. Other minerals present in small amounts may include kaolinite and quartz.

The zeta potential of gibbsite was measured by electrophoresis and the point of zero charge (PZC) of the gibbsite sample was found to be pH ~8.5, as shown in Figure 4.3. The PZC of the gibbsite sample in this study is close to that reported in the literature with a range of pH 7.5–11.3 (Kosmulski 2009; Adekola et al. 2011). The characterization of these model surfaces provides confidence for the further analysis of kaolinite flotation chemistry.

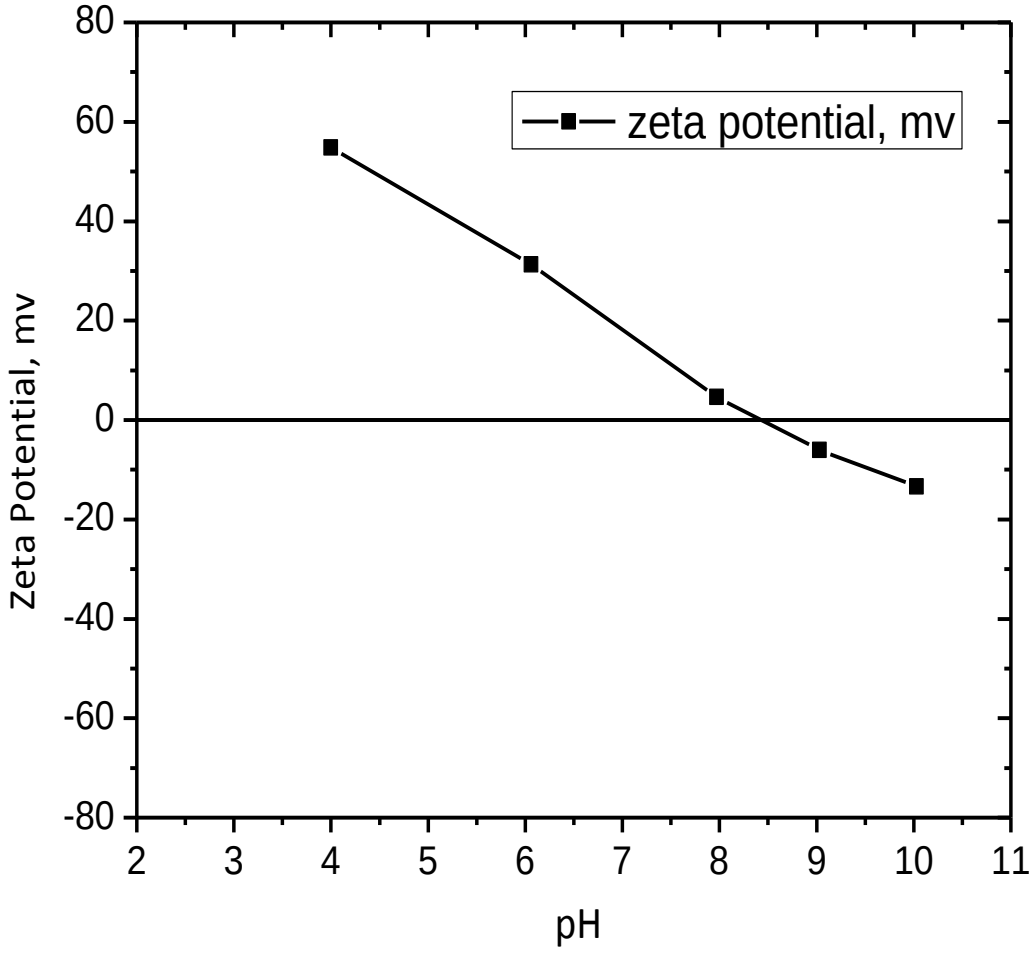

Figure 4.3. Zeta potential of gibbsite sample as a function of pH.

4.3.2 Effect of pH on the Contact Angle of Kaolinite Model Surfaces

The contact angle results for the gibbsite surface with/without the dodecyl amine hydrochloride collector are summarized in Table 4.2. Without the collector, the water film between the bubble and gibbsite surface does not rupture, which indicates the gibbsite surface is very hydrophilic in nature. With the addition of the collector, the gibbsite surface remains hydrophilic in acidic solution, suggesting no adsorption of the collector. In fact, the adsorption of the collector at the gibbsite surface is not expected to happen since both the gibbsite surface and the amine are positively charged in acidic solution resulting in repulsion due to electrostatic interaction.

Table 4.2. Contact angle results for gibbsite surface in dodecyl amine hydrochloride solution using captive bubble method.

Collector Concentration	Contact Angle*				
	pH 3	pH 4	pH 6	pH 8	pH 10
None	NA	NA	NA	NA	NA
1×10^{-5} M	NA	NA	NA	NA	20.1
5×10^{-5} M	NA	NA	NA	17.0	25.0
1×10^{-4} M	NA	NA	NA	16.6	30.3
2×10^{-4} M	NA	NA	NA	16.3	39.0

*NA stands for no attachment.

At high pH (pH 8–10), the contact angle of the gibbsite surface increases and the gibbsite surface becomes somewhat hydrophobic. The change of the wettability of gibbsite surface suggests the adsorption of dodecyl amine hydrochloride on the gibbsite surface. At pH 10, the gibbsite surface is negatively charged and the amine collector is positively charged. In this way, the amine molecules adsorb at the gibbsite surface by electrostatic attraction, stabilized by hydrophobic interaction of the hydrocarbon chains of amine molecules. The interaction between the alumina face surface of kaolinite particles and the dodecyl amine collector is anticipated to be similar to that observed between the gibbsite surface and the amine collector. In this regard, the alumina face surface of kaolinite particles is expected to remain hydrophilic at low pH, but to adsorb the amine collector at high pH and become somewhat hydrophobic with a contact angle of about 20–40 ° at pH 10, as shown in Table 4.2.

The contact angle measurements at the pyrophyllite basal plane surface with and without dodecyl amine hydrochloride are revealed in Table 4.3. The results illustrate that the pyrophyllite basal plane surface is naturally hydrophobic, with a contact angle of 45–50 °. The point of zero charge of pyrophyllite is believed to be below pH 3. With the addition of the amine collector, the pyrophyllite surface becomes more hydrophobic due to the attractive electrostatic interaction between the negatively charged pyrophyllite basal plane surface and positively charged amine. However, like other phyllosilicate minerals, the pyrophyllite basal plane surface (silica surface) carries a permanent negative charge due to isomorphous substitution in the crystal and is not so dependent on pH (Yin et al. 2012). The increase in the water contact angle of the pyrophyllite surface from pH 8 to pH 10 at collector concentration of 1×10^{-5} M and 5×10^{-5} M is expected to be related to the

Table 4.3. Contact angle results for pyrophyllite basal plane surface in dodecyl amine hydrochloride solution using captive bubble method.

Collector Concentration	Contact Angle				
	pH 3	pH 4	pH 6	pH 8	pH 10
None	46.8	49.9	48.4	50.9	36.7
1×10^{-5} M	52.2	49.7	55.4	55.7	70.0
5×10^{-5} M	56.5	57.6	64.0	57.8	81.5
1×10^{-4} M	60.4	57.3	62.4	63.8	58.1
2×10^{-4} M	56.8	60.8	56.9	54.8	48.0

solution chemistry of dodecyl amine as described in Equation (4-3) and (4-4). At pH 10, dodecyl amine molecule and dodecyl amine colloid is favored compared to the solution at pH 8. Slight precipitation of dodecyl amine may account for the increase of the contact angles. Note the sudden decrease of the contact angles at pH 10 and collector concentration greater than 1×10^{-4} M, which is discussed in Section 4.3.3. Similarly, the silica face surface of kaolinite particles is anticipated to be slightly more hydrophobic with the addition of the collector as well as with increasing pH.

Hydrolysis of dodecyl amine:

$$RNH_{2(aq)} + H_2O \leftrightarrows RNH_3^+ + OH^- \qquad K = 4.3\times10^{-4} \tag{4-3}$$

In saturated system,

$$RNH_{2(s)} \leftrightarrows RNH_{2(aq)} \qquad K = 2\times10^{-5} \tag{4-4}$$

4.3.3 Effect of Dodecyl Amine Concentration on the Contact Angle of Kaolinite Model Surfaces

The impact of dodecyl amine concentration on the wettability of kaolinite model surfaces, namely the gibbsite surface and the pyrophyllite basal plane surface, is presented in Table 4.2 and Table 4.3 along with the effect of pH. At pH 4, the hydrophobicity of pyrophyllite surface increases with increasing concentration of amine collector, suggesting that the coverage of the amine molecules on the pyrophyllite surface is below the monolayer; in contrast, the wettability of the gibbsite surface does not change much with the addition of the collector, as shown in Figure 4.4. It is believed that the electrostatic repulsion accounts for the lack of amine adsorption at the gibbsite surface in acidic solution, whereas electrostatic attraction accounts for adsorption of the amine collector at the pyrophyllite surface.

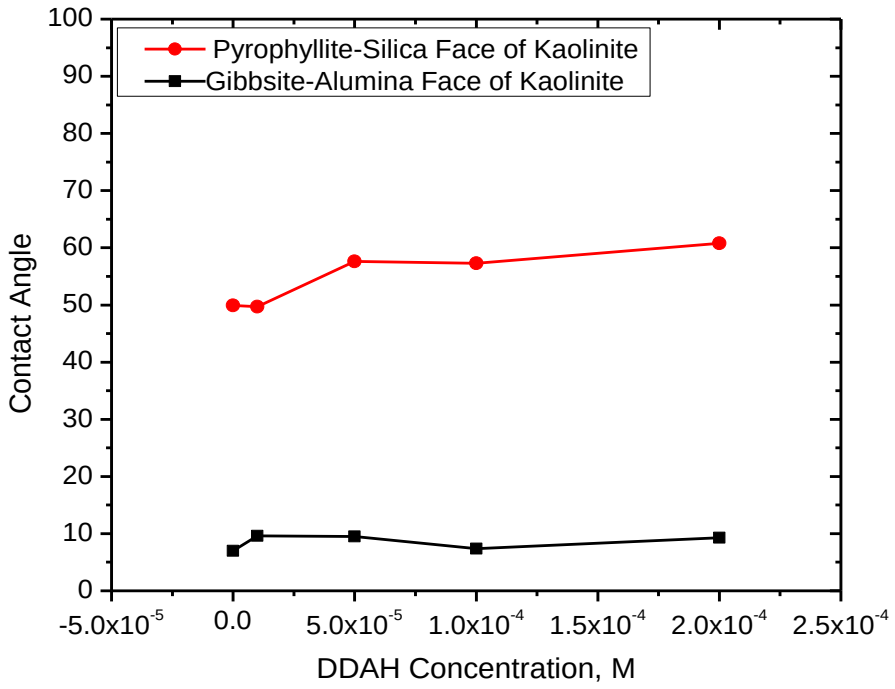

Figure 4.4. The comparison of the contact angle results for gibbsite and pyrophyllite surfaces after the adsorption of the dodecyl amine hydrochloride (DDAH) at pH 4.

At high pH (pH 8–10), the hydrophobicity of the gibbsite surface increases slightly with increasing collector concentration due to the electrostatic attraction between gibbsite and amine. In contrast, the impact of the collector addition on the hydrophobicity of pyrophyllite surface is significant especially at pH 10, where the contact angle of pyrophyllite surface increases from ~40 ° to 70–80 °. The hydrophobicity of pyrophyllite increases slightly with increasing collector concentration but decreases with collector concentrations greater than 1×10^{-4} M at pH 10.

According to Laskowski's thermodynamic equilibrium diagram for dodecyl amine solution (Laskowski 1989), the solubility limit of dodecyl amine solution is reached with a concentration of 1×10^{-4} M at pH 10. During the experiment, precipitation of the dodecyl amine collector was observed for an amine concentration of 1×10^{-4} M and 2×10^{-4} M at pH 10. For the case of precipitated amine, interesting phenomena occur, which is the contact angle of pyrophyllite surface changes with time. The contact angle is large (~90°) when the bubble first attaches at the pyrophyllite surface, but immediately the contact angle decreases until ~50° within several seconds. Note the results presented in Table 4.2 and Table 4.3 are recorded after 30s, when the bubble is relatively stable on the pyrophyllite surface. Similar phenomena of dynamic contact angle for dodecyl amine solution has been reported in the literature (Smith 1963; Finch and Smith 1979; Smith and Scott 1990). It is reported that the contact angle for quartz surface in dodecyl amine solution can vanish from 80–86° to nil in the end. In our experiments, the contact angle does not totally vanish; instead it is stabilized at ~40–45° after several minutes even hours. Of course, the final equilibrium contact angle is expected to rely on the features of the mineral surface. It is known that quartz is very hydrophilic without the collector, while the pyrophyllite surface

is naturally hydrophobic, which may account for the observed equilibrium contact angle to some extent. It appears that the dynamic contact angle is related to the precipitation of dodecyl amine on the mineral surface, which may result in multilayer coverage. Unfortunately, a complete understanding of the dynamic contact angle phenomenon has not yet been achieved.

4.3.4 Discussion of Reverse Flotation

The reverse flotation of kaolinite from bauxite using amine is achieved at pH 4–5, as shown in Figure 4.5 (Hu et al. 2005; Marino 2012). Unfortunately, the nature of the reverse flotation of kaolinite is not well understood. Only recently have details of the kaolinite surface been established. As described in Chapter 2, kaolinite has three different surfaces: the silica face surface, the alumina face surface, and the edge surface. The silica face surface and edge surface are negatively charged above pH 4; however, the alumina face surface is positively charged below pH 6 and negatively charged above pH 8. At low pH (~pH 4), the layer to layer interaction between the alumina face surface and silica face surface is significant, as well as the interaction between the alumina face surface and the edge surface. At high pH (pH 8–10), the kaolinite suspension is well dispersed; maybe occasionally self-aggregation occurs due to weak van der Waals interaction.

Based on the study of kaolinite particle interaction in Chapter 3, about 10% more of the silica face surfaces are displayed by the kaolinite clusters compared to the alumina face surfaces at low pH (pH 4–5). The silica surfaces are negatively charged and relatively hydrophobic. The charge of dodecyl amine is positive below pH 11 (Laskowski 1989). The resulting clusters promote dodecyl amine collector adsorption at the silica surfaces, giving rise to clusters with hydrophobic character ready for flotation. A simple drawing in Figure

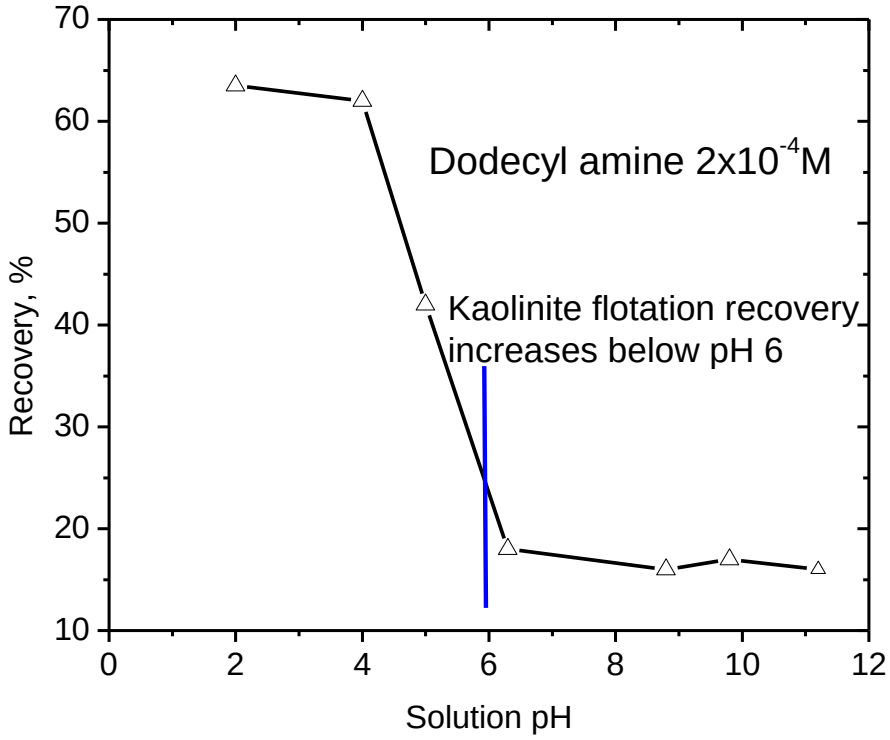

Figure 4.5. The flotation recovery of kaolinite with 2×10^{-4} M dodecyl amine (Data source: Hu et al. 2005).

4.6 illustrates an ideal situation of the kaolinite cluster interaction with the dodecyl amine collector at low pH (~pH 4), forming a hydrophobic structure. In addition, the particle size of kaolinite is significantly increased by forming the cluster structure, much larger in size compared to the size of the primary kaolinite particle. It is reported that the collision efficiency (defined as the probability of collision) between the particles and bubbles is positively correlated with the particle size when the particle size is much smaller than the bubble size (Gaudin 1957; Jameson et al. 2007). The cluster formation with larger size significantly increases the possibility of the bubble attachment at cluster surfaces, thus resulting in greater flotation recovery. In contrast, the gibbsite and the alumina face surfaces of kaolinite particle do not appear to adsorb the dodecyl amine collector and such surfaces remain hydrophilic. In this way, kaolinite particles/clusters are floated with

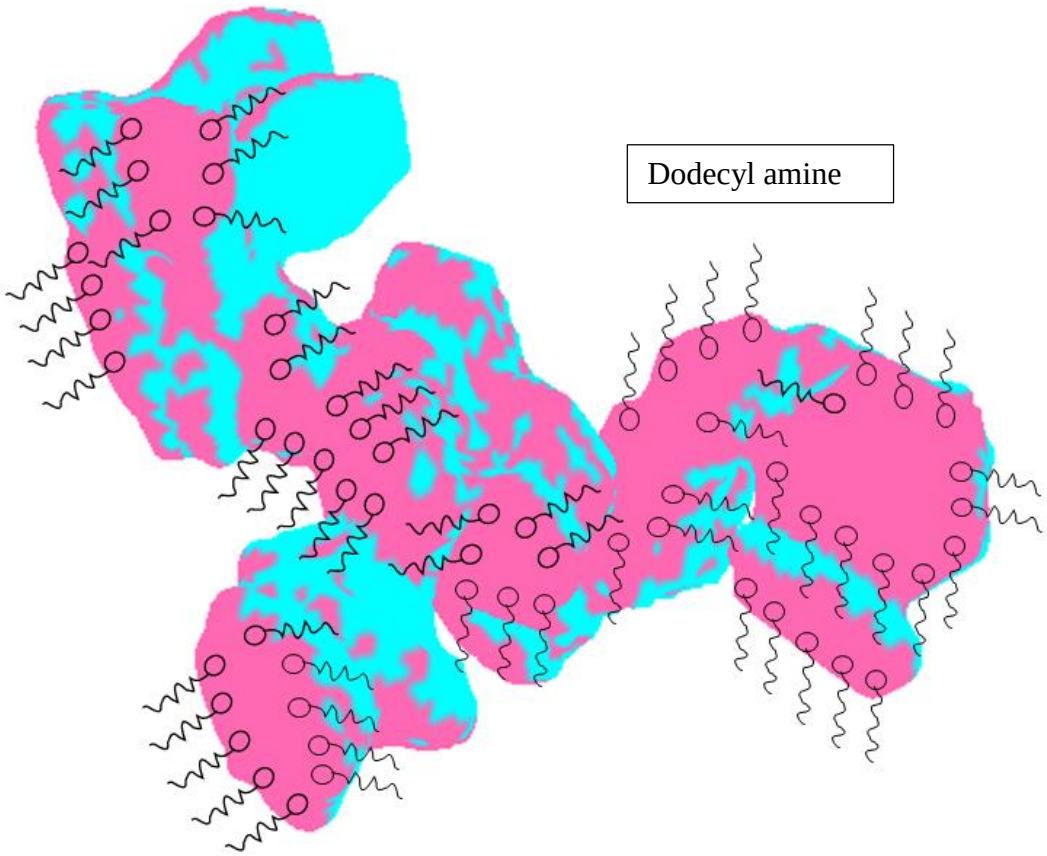

Figure 4.6. Kaolinite cluster interaction with dodecyl amine collector at low pH (~pH 4). Pink surfaces represent the silica face surface of a kaolinite particle, and blue surfaces represent the alumina face surface of a kaolinite particle.

dodecyl amine and separated from gibbsite.

At high pH (pH 8–10), all the surfaces of kaolinite particles as well as gibbsite are able to adsorb dodecyl amine by electrostatic attraction. In this case, a good separation efficiency cannot be achieved. It is expected that cluster formation will reduce collector consumption because of the reduction in surface available for adsorption.

4.4 Summary

Gibbsite and pyrophyllite basal plane surfaces have been used as model surfaces to simulate the interaction of the two face surfaces of kaolinite and the dodecyl amine collector. The effect of pH and the collector concentration on the hydrophobicity of the model surfaces has been investigated based on contact angle measurements. With the addition of dodecyl amine, the gibbsite surface (or alumina face surface of kaolinite) remains hydrophilic at low pH (pH 3–6), but becomes somewhat hydrophobic at high pH (pH 8–10), indicating that amine adsorption only occurs at high pH.

In contrast, the pyrophyllite basal plane surface (the silica face surface of kaolinite) becomes more hydrophobic with the addition of dodecyl amine for the whole pH range studied, indicating the adsorption of the collector occurs in both acidic solution and alkaline solution. Interesting phenomena have been observed beyond the solubility limit of dodecyl amine (a concentration of 1×10^{-4} M at pH 10), in that the initial high contact angle (~90 °) of the pyrophyllite surface decreases rapidly after bubble attachment, reaching an equilibrium contact angle of ~50 ° after several seconds.

The mechanism of kaolinite flotation from gibbsite is discussed based on the surface properties of kaolinite particles, cluster structure, and particle–collector interaction. A reasonable explanation for kaolinite flotation process is now available. The efficient

flotation of kaolinite at low pH is caused by the fact that large clusters of kaolinite particles are formed. The increased size of the clusters and collector adsorption at exposed silica face surfaces account for the effective reverse flotation of kaolinite from bauxite ores.

CHAPTER 5

SUMMARY, CONCLUSION, AND RESEARCH RECOMMENDATIONS

The major objectives of this dissertation were to investigate the surface charging properties of kaolinite particles, including kaolinite particle interactions, and to examine the nature of the reverse flotation of kaolinite particles from bauxite ore. In particular, kaolinite edge surfaces were prepared and their surface charge was determined for the first time. In addition, the kaolinite particle interactions, specifically the formation of aggregated particle structures/clusters, were established by both simulation and experimental techniques. In this regard, the research objectives have been achieved, and the major accomplishments and contributions are summarized as follows.

A novel protocol was developed to prepare ordered edge surfaces of kaolinite particles (~500 nm). A sandwich sample with kaolinite particles in between two resin substrates was prepared and a smooth edge surface of the sandwich sample was prepared by ultra-microtome. The exposed kaolinite edge surfaces were imaged by AFM with a very sharp tip (tip radius is estimated to be 3–4 nm). The thicknesses of kaolinite edges were evaluated and the average thickness was found to be 38.3 nm $\pm$ 11.7 nm in this study. The charge of the edge surface was determined to be negative above pH 4 and the magnitude of the surface charge was found to be dependent on pH. Molecular dynamics simulation

(MDS) results suggest that the kaolinite edge surface is very hydrophilic. With the results from this dissertation research and the results from previous research (Gupta and Miller 2010; Yin et al. 2012), the charge and wettability of each of the three surfaces of kaolinite particles have now been established.

The influence of ionic strength on the surface charge of selected phyllosilicates was studied by AFM. It was established that the magnitude of the charge for the silica face surface of the phyllosilicates is dependent on the degree of isomorphous substitution. The muscovite basal plane surface shows greatest surface charge density, followed by the kaolinite silica face surface, while the talc basal plane surface carries the least surface charge density. In addition, the surface charge densities of the basal plane surfaces of phyllosilicates were found to be constant with increasing ionic strength, except for a slight increase at high ionic strength (100 mM). Both the alumina face surface charge and the edge surface charge of kaolinite particles increase with increasing ionic strength. Only at 100 mM ionic strength does the surface charge density of the alumina face surface slightly decrease. Moreover, the cluster size of kaolinite particles was found to increase with increasing ionic strength as determined by photon correlation spectroscopy (PCS). A plateau for the cluster size is reached at 500 mM ionic strength. It is expected that the competition between electrostatic force and van der Waals force accounts for the cluster formation and van der Waals force plays a greater role at higher ionic strength. It is expected that these fundamental results will provide a basis for the understanding of kaolinite suspensions in saline water.

With the surface properties of kaolinite particles established, kaolinite particle interactions were investigated as a function of pH and ionic strength using Brownian

dynamics simulation. To facilitate computation, a coarse-grained model for kaolinite particles was developed. At low pH (pH 5), aggregated kaolinite particle structures with silica face to alumina face interaction and alumina face to edge surface interaction are formed. In contrast, particles are well dispersed at pH 8 and no obvious clusters or aggregated particle structures are observed. The aggregated particle structures at pH 5 were analyzed in terms of the aggregate size (expressed as number of particles per structure/cluster), the surface area, and the exposure of silica and alumina faces. It was determined at pH 5 that the silica surface of kaolinite particles is ~10% more exposed than the alumina surface. Additionally, an ellipsoid enveloped model was used to study the composition of the cluster considering associated water. The clusters were found to contain about 50% solids. The simulation results also reveal that ionic strength promotes the aggregation and formation of particle structures. In addition, the effect of simulation time on the aggregated particle structures/clusters was studied, and the results suggest that equilibrium is not achieved in this study. The particle structures continue to aggregate with increasing simulation time, even after a simulation time of 30 ns. Experimental techniques including SEM (ESEM, SEM with WETSEM capsule) and Micro CT have confirmed the cluster structures and the composition of clusters obtained by simulation. In this way, coarse-grained simulation has been shown to be a useful technique for the analysis of particle interactions.

Based on previous fundamental studies on the surface properties and interaction of kaolinite particles, the nature of reverse flotation of kaolinite from bauxite ore was established. Gibbsite and pyrophyllite basal plane surfaces were selected to be model surfaces and to represent the alumina face surface and the silica face surface of kaolinite

particles. The interactions of the model surfaces with the dodecyl amine collector were studied. The adsorption of dodecyl amine and the hydrophobicity of the two basal plane surfaces of kaolinite particles in terms of pH and collector concentration were discussed. Interesting phenomena were observed in these experiments; a large initial contact angle (~90 °) for the pyrophyllite basal plane surface decreases to a small contact angle (~40–45 °) beyond the solubility limit of dodecyl amine at pH 10. The hydrophobic nature of kaolinite surfaces does not change significantly with the addition of the collector, in spite of the fact that the alumina surface is hydrophilic and the silica surface is hydrophobic. It was concluded that particle aggregation resulting in large clusters accounts for the improved flotation recovery of kaolinite at low pH (pH 4–5). It is expected that collector consumption might be reduced with the formation of aggregated kaolinite structures since all kaolinite surfaces in the cluster may not be available for collector adsorption. In addition, the 10% more exposure of negatively charged silica faces in kaolinite clusters facilitates the adsorption of amine collectors by electrostatic interaction.

Regarding future research, the following areas can be considered: 1) Study of the surface properties of other phyllosilicates. The protocol developed to prepare the edge surfaces of kaolinite particles in this study is expected to be applied to the study of other phyllosilicates, for example pyrophyllite, illite, and smectite, etc. A comparison of the surface charge of the edge surfaces of different phyllosilicates with respect to the degree of isomorphous substitution can be very interesting and useful. 2) Applications of kaolinite particle interactions. Based on the achievements accomplished in this dissertation, further investigation on the impact of kaolinite particle interactions on mineral processing operations, including flocculation, sedimentation, and flotation, can be studied both by

simulation and experimental techniques. Moreover, new chemicals for flocculation and for the flotation of kaolinite may be possible based on the fundamental understanding that has been developed.

REFERENCES

Adekola, F., Fédoroff, M., Geckeis, H., Kupcik, T., Lefèvre, G., Lützenkirchen, J., Plaschke, M., Preocanin, T., Rabung, T., and Schild, D. 2011. Characterization of acid–base properties of two gibbsite samples in the context of literature results. *J. Colloid Interface Sci.* 354 (1):306-317.

Anderson, K.L., Sinsawat, A., Vaia, R.A., and Farmer, B. 2005. Control of silicate nanocomposite morphology in binary fluids: Coarse-grained molecular dynamics simulations. *J. Polym. Sci. Part B Polym. Phys.* 43 (8):1014-1024.

Assemi, S., Nguyen, A.V., and Miller, J.D. 2008. Direct measurement of particle–bubble interaction forces using atomic force microscopy. *Int. J. Miner. Process.* 89 (1):65-70.

Avena, M.J., Mariscal, M.M., and De Pauli, C.P. 2003. Proton binding at clay surfaces in water. *Appl. Clay Sci.* 24 (1–2):3-9.

Bailey, S. 1980. Summary of recommendations of AIPEA nomenclature committee. *Clay Miner.* 15 (1):85-93.

Barshack, I., Kopolovic, J., Chowers, Y., Gileadi, O., Vainshtein, A., Zik, O., and Behar, V. 2004. A novel method for "wet" SEM. *Ultrastructural pathology* 28 (1):29-31.

Berendsen, H.J., Postma, J., Van Gunsteren, W., and Hermans, J. 1981. Interaction models for water in relation to protein hydration. *Intermolecular forces*: Springer.

Bergaya, F., Theng, B.K., and Lagaly, G. 2011. *Handbook of clay science*. Vol. 1: Elsevier.

Bish, D.L. 1993. Rietveld refinement of the kaolinite structure at 1.5 K. *Clays Clay Miner.* 41 (6):738-744.

Bittencourt, L.R., Lin, C.L., and Miller, J.D. 1990. Flotation recovery of high-purity gibbsite concentrates from a Brazilian bauxite ore. *Advanced Materials-Application of Mineral and Metallurgical Processing Principles*:77-85.

Boulet, P., Coveney, P.V., and Stackhouse, S. 2004. Simulation of hydrated Li+-, Na+- and K+-montmorillonite/polymer nanocomposites using large-scale molecular dynamics. *Chem. Phys. Lett.* 389 (4–6):261-267.

Brady, P.V., Cygan, R.T., and Nagy, K.L. 1996. Molecular controls on kaolinite surface charge. *J. Colloid Interface Sci.* 183 (2):356-64.

Bragg, W.H.; Bragg, W.L. 1913. The reflexion of x-rays by crystals. *Proc. R. Soc. A* 88 (605): 428–38.

Bray, E.L. 2014. Bauxite and Alumina Statistics and Information. *USGS Mineral Industry Surveys.*

Brogoitti, W.B. 1974. Selective flocculation and flotation of slimes from sylvinite ores. U.S.: U.S. Patents.

Call, R.D. 1992. Slope stability. *SME mining engineering handbook* 1:881-96.

Castro, S. 2012. Challenges in flotation of Cu-Mo sulfide ores in sea water. *Water in Mineral Processing: Proceedings of the First International Symposium, SME*:29-40.

Chang, F.-R.C., and Sposito, G. 1996. The electrical double layer of a disk-shaped clay mineral particle: Effects of electrolyte properties and surface charge density. *J. Colloid Interface Sci.* 178 (2):555-564.

Chassagne, C., Mietta, F., and Winterwerp, J.C. 2009. Electrokinetic study of kaolinite suspensions. *J. Colloid Interface Sci.* 336 (1):352-9.

Cignoni, P., Corsini, M., and Ranzuglia, G. 2008. Meshlab: an open-source 3d mesh processing system. *Ercim news* 73:45-46.

Cygan, R.T., Liang, J.-J., and Kalinichev, A.G. 2004. Molecular models of hydroxide, oxyhydroxide, and clay phases and the development of a general force field. *J. Phys. Chem. B* 108 (4):1255-1266.

de Almeida Gomes, G., and Boodts, J.F.C. 1999. Investigation of the surface properties of an oxide of interest in the field of a conductive oxide system: Influence of precursor and purification. *J. Braz. Chem. Soc.* 10 (2):92-96.

Delhorme, M., Jönsson, B., and Labbez, C. 2012. Monte Carlo simulations of a clay inspired model suspension: the role of rim charge. *Soft Matter* 8 (37):9691-9704.

Drelich, J., Long, J., and Yeung, A. 2007. Determining Surface Potential of the Bitumen-Water Interface at Nanoscale Resolution using Atomic Force Microscopy. *Can. J. Chem. Eng.* 85 (5):625-634.

Repeated Author. 2007. Determining Surface Potential of the Bitumen-Water Interface at Nanoscale Resolution using Atomic Force Microscopy. *Can. J. Chem. Eng.* 85 (5):625-634.

Drelich, J., and Miller, J.D. 2012. Induction Time Measurements for Air bubbles on Chalcopyrite, Bornite, and Gold in Seawater. *Water in Mineral Processing: Proceedings of the First International Water Symposium, SME*:73-85.

Du, H., and Miller, J. 2007. A molecular dynamics simulation study of water structure and adsorption states at talc surfaces. *Int. J. Miner. Process.* 84 (1):172-184.

Du, H., and Miller, J.D. 2007. Adsorption states of amphipatic solutes at the surface of naturally hydrophobic minerals: a molecular dynamics simulation study. *Langmuir* 23 (23):11587-96.

Du, J., Pushkarova, R.A., and Smart, R.S.C. 2009. A cryo-SEM study of aggregate and floc structure changes during clay settling and raking processes. *Int. J. Miner. Process.* 93 (1):66-72.

Everaers, R., and Ejtehadi, M. 2003. Interaction potentials for soft and hard ellipsoids. *Phys. Rev. E* 67 (4):041710.

Finch, J.A., and Smith, G.W. 1979. Contact-angle and wetting. *Miner. Sci. Eng.* 11 (1):36-63.

Flegmann, A., Goodwin, J., and Ottewill, R. 1969. Rheological studies on kaolinite suspensions. Paper read at Proc. Br. Ceram. Soc.

Fuerstenau, D. 1980. Fine particle flotation. *Fine particles processing* 1:669-705.

Gaudin, A.M. 1957. *Flotation*: McGraw-Hill New York.

Giese, R., Costanzo, P., and Van Oss, C. 1991. The surface free energies of talc and pyrophyllite. *Phys. Chem. Miner.* 17 (7):611-616.

Green, M.S. 1954. Markoff random processes and the statistical mechanics of time-dependent phenomena. II. Irreversible processes in fluids. *J. Chem. Phys.* 22 (3):398-413.

Greenwell, H.C., Harvey, M.J., Boulet, P., Bowden, A.A., Coveney, P.V., and Whiting, A. 2005. Interlayer structure and bonding in nonswelling primary amine intercalated clays. *Macromolecules* 38 (14):6189-6200.

Greer, J., and Bush, B.L. 1978. Macromolecular shape and surface maps by solvent exclusion. *Proc. Natl. Acad. Sci. U.S.A.* 75 (1):303-307.

Grim, R.E. 1953. Clay mineralogy. *Soil Sci.* 76 (4):317.

Grim, R.E. 1962. *Applied clay mineralogy*: McGraw-Hill New York.

Guggenheim, S., and Martin, R. 1995. Definition of clay and clay mineral: joint report of the AIPEA nomenclature and CMS nomenclature committees. *Clays Clay Miner.* 43 (2):255-256.

Gupta, V. Internal Research Report. University of Utah 2010.

Gupta, V. 2011. Surface charge features of kaolinite particles and their interactions, The University of Utah.

Gupta, V., Hampton, M.A., Stokes, J.R., Nguyen, A.V., and Miller, J.D. 2011. Particle interactions in kaolinite suspensions and corresponding aggregate structures. *J Colloid Interface Sci.* 359 (1):95-103.

Gupta, V., and Miller, J.D. 2010. Surface force measurements at the basal planes of ordered kaolinite particles. *J Colloid Interface Sci.* 344 (2):362-71.

Hamaker, H.C. 1937. The London—van der Waals attraction between spherical particles. *Physica* 4 (10):1058-1072.

Harris, R. 2004. Minerals in paper—looking east for growth. *Industrial Minerals* 443:52-57.

Hiemstra, T., Van Riemsdijk, W.H., and Bolt, G.H. 1989. Multisite proton adsorption modeling at the solid/solution interface of (hydr)oxides: A new approach: I. Model description and evaluation of intrinsic reaction constants. *J. Colloid Interface Sci.* 133 (1):91-104.

Hilderbrand, T.M., and Yoon, R.-H. 1986. Purification of kaolin clay by froth flotation using hydroxamate collectors. Google Patents.

Hogg, R. 2013. Bridging flocculation by polymers. *KONA Powder and Particle Journal* 30 (0):3-14.

Hu, Y., Jiang, H., Qiu, G., and Wang, D. 2001. Solution chemistry of flotation separation of diasporic bauxite. *J. Nonferrous Metals* 11 (1):125-130.

Hu, Y., Jiang, H., and Wang, D. 2003. Electrokinetic behavior and flotation of kaolinite in CTAB solution. *Miner. Eng.* 16 (11):1221-1223.

Hu, Y., Liu, X., and Xu, Z. 2003. Role of crystal structure in flotation separation of diaspore from kaolinite, pyrophyllite and illite. *Miner. Eng.* 16 (3):219-227.

Hu, Y., Wei, S., Haipu, L., and Xu, Z. 2004. Role of macromolecules in kaolinite flotation. *Miner. Eng.* 17 (9–10):1017-1022.

Hu, Y., Wei, S., Hao, J., Miller, J.D., and Fa, K. 2005. The anomalous behavior of kaolinite

flotation with dodecyl amine collector as explained from crystal structure considerations. *Int. J. Miner. Process.* 76 (3):163-172.

Israelachvili, J.N. 2011. *Intermolecular and Surface Forces: Revised Third Edition*: Academic press.

Jameson, G.J., Nguyen, A.V., and Ata, S. 2007. The flotation of fine and coarse particles. *Froth Flotation: A Century of Innovation*:339-372.

Jewett, A.I., Zhuang, Z., and Shea, J.-E. 2013. Moltemplate a coarse-grained model assembly tool. *Biophysical J.* 104:169.

Jiang, H., Xu, L.-H., Hu, Y.-H., Wang, D.-Z., Li, C.-K., Meng, W., and Wang, X.-J. 2011. Flotation and adsorption of quaternary ammonium cationic collectors on diaspore and kaolinite. *Trans. Nonferrous Met. Soc. China (English Edition)* 21 (11):2528-2534.

Jodin, M.-C., Gaboriaud, F., and Humbert, B. 2005. Limitations of potentiometric studies to determine the surface charge of gibbsite γ-Al(OH)3 particles. *J. Colloid Interface Sci.* 287 (2):581-591.

Joussein, E., Petit, S., Churchman, J., Theng, B., Righi, D., and Delvaux, B. 2005. Halloysite clay minerals—a review. *Clay Miner.* 40 (4):383-426.

Juffer, A.H., and Vogel, H.J. 1998. A flexible triangulation method to describe the solvent-accessible surface of biopolymers. *J. Comput. Aided Mol. Des.* 12 (3):289-299.

Klimpel, R., and Hogg, R. 1991. Evaluation of floc structures. *Colloids Surf.* 55:279-288.

Kosmulski, M. 2001. *Chemical properties of material surfaces*. New York, USA: CRC press.

Kosmulski, M. 2009. Compilation of PZC and IEP of sparingly soluble metal oxides and hydroxides from literature. *Adv. Colloid Interface Sci.* 152 (1–2):14-25.

Kretzschmar, R., Holthoff, H., and Sticher, H. 1998. Influence of pH and humic acid on coagulation kinetics of kaolinite: a dynamic light scattering study. *J. Colloid Interface Sci.* 202 (1):95-103.

Kubo, R. 1957. Statistical-mechanical theory of irreversible processes. I. General theory and simple applications to magnetic and conduction problems. *J. Phys. Soc. Jpn.* 12 (6):570-586.

Kutter, S., Hansen, J.-P., Sprik, M., and Boek, E. 2000. Structure and phase behavior of a model clay dispersion: A molecular-dynamics investigation. *J. Chem. Phys.* 112 (1):311-322.

Lagaly, G., and Bergaya, F. 2013. *Handbook of clay science*: Elsevier.

Laskowski, J. 1989. The colloid chemistry and flotation properties of primary aliphatic amines. *Challenges in Mineral Processing. Soc. Mining Eng.*:15-34.

Laskowski, J., Castro, S., and Ramos, O. 2013. Effect of Seawater Main Components on Frothability in the Flotation of Cu-Mo Sulfide Ore *Physicochem. Probl. Miner. Process.* 50 (1):17-29.

Lemieux, P.R., and Rumpf, D.S. 1991. Lightweight oil and gas well proppants. Google Patents.

Likos, W.J., and Lu, N. 2001. A Laser Technique to Quantify the Size, Porosity, and Density of Clay Clusters During Sedimentation. *Geotech. Test. J.* 24 (1):83-91.

Lin, C., and Miller, J. 2002. Cone beam X-ray microtomography-a new facility for three-dimensional analysis of multiphase materials. *Miner. Metall. Process* 19 (2):65-71.

Liu, C., Hu, Y., and Cao, X. 2009. Substituent effects in kaolinite flotation using dodecyl tertiary amines. *Miner. Eng.* 22 (9-10):849-852.

Liu, C., Hu, Y., Feng, A., Guo, Z., and Cao, X. 2011. The behavior of N,N-dipropyl dodecyl amine as a collector in the flotation of kaolinite and diaspore. *Miner. Eng.* 24 (8):737-740.

Liu, J., Sandaklie-Nikolova, L., Wang, X., and Miller, J.D. 2014. Surface force measurements at kaolinite edge surfaces using atomic force microscopy. *J. Colloid Interface Sci.* 420 (0):35-40.

Liu, J., Xu, Z., and Masliyah, J. 2004. Role of fine clays in bitumen extraction from oil sands. *AIChE J.* 50 (8):1917-1927.

Lorensen, W.E., and Cline, H.E. 1987. Marching cubes: A high resolution 3D surface construction algorithm. Paper read at ACM Siggraph Computer Graphics.

Ma, X., Bruckard, W.J., and Holmes, R. 2009. Effect of collector, pH and ionic strength on the cationic flotation of kaolinite. *Int. J. Miner. Process.* 93 (1):54-58.

Marino, S.L. 2012. The flotation of marginal gibbsitic bauxite ores from paragominas-brazil. Master Thesis. The University of Utah.

Markutsya, S., Subramaniam, S., Vigil, R.D., and Fox, R.O. 2008. On Brownian dynamics simulation of nanoparticle aggregation. *Ind. Eng. Chem. Res.* 47 (10):3338-3345.

Martyna, G.J., Tobias, D.J., and Klein, M.L. 1994. Constant pressure molecular dynamics algorithms. *J. Chem. Phys.* 101 (5):4177-4189.

Masliyah, J.H., and Bhattacharjee, S. 2006. *Electrokinetic and colloid transport phenomena*: John Wiley & Sons.

Massola, C.P., Chaves, A.P., Andrade, C.F., and Abreu, C.A.V. 2007. Reverse froth flotation of bauxites from the Zona da Mata area. *Xxii Encontro Nacional de Tratamento de Min ́erios e Metalurgia Extrativa* 1.

McCullough, E.C. 1975. Photon attenuation in computed tomography. *J. Med. Phys.* 2 (6):307-320.

Melchionna, S., Ciccotti, G., and Lee Holian, B. 1993. Hoover NPT dynamics for systems varying in shape and size. *Mol. Phys.* 78 (3):533-544.

Meunier, A., and Fradin, N. 2005. *Clays*: Springer.

Michaels, A., and Bolger, J. 1964. Particle interactions in aqueous kaolinite dispersions. *Ind. Eng. Chem. Fundam.* 3 (1):14-20.

Mierczynska-Vasilev, A., and Beattie, D.A. 2013. The effect of impurities and cleavage characteristics on talc hydrophobicity and polymer adsorption. *Int. J. Miner. Process.* 118 (0):34-42.

Miller, J.D., Nalaskowski, J., Abdul, B., and Du, H. 2007. Surface characteristics of kaolinite and other selected two layer silicate minerals. *Can. J. Chem. Eng.* 85 (5):617-624.

Mitchell, J.K., and Soga, K. 1976. *Fundamentals of soil behavior*: Wiley New York.

Mueller, S., Llewellin, E., and Mader, H. 2011. The effect of particle shape on suspension viscosity and implications for magmatic flows. *Geophys. Res. Lett.* 38 (13).

Murray, H.H. 1991. Overview—clay mineral applications. *Appl. Clay Sci.* 5 (5):379-395.

Murray, H.H. 2000. Traditional and new applications for kaolin, smectite, and palygorskite: a general overview. *Appl. Clay Sci.* 17 (5):207-221.

Nalaskowski, J., Abdul, B., Du, H., and Miller, J. 2007. Anisotropic character of talc surfaces as revealed by streaming potential measurements, atomic force microscopy, molecular dynamics simulations and contact angle measurements. *Can. Metall. Q.* 46 (3):227-235.

Nalaskowski, J., Drelich, J., Hupka, J., and Miller, J.D. 2003. Adhesion between hydrocarbon particles and silica surfaces with different degrees of hydration as determined by the AFM colloidal probe technique. *Langmuir* 19 (13):5311-5317.

Nishimura, S., Tateyama, H., Tsunematsu, K., and Jinnai, K. 1992. Zeta potential

measurement of muscovite mica basal plane-aqueous solution interface by means of plane interface technique. *J. Colloid Interface Sci.* 152 (2):359-367.

O'Brien, N.R. 1971. Fabric of kaolinite and illite floccules. *Clays Clay Miner.* 19:353-359.

Odriozola, G., Romero-Bastida, M., and Guevara-Rodriguez, F.d.J. 2004. Brownian dynamics simulations of Laponite colloid suspensions. *Phys. Rev. E* 70 (2):021405.

Palomino, A.M., and Santamarina, J.C. 2005. Fabric map for kaolinite effects of pH and ionic concentration on behavior. *Clays Clay Miner.* 53 (3):211-223.

Parsegian, V., Van Olphen, H., and Mysels, K. 1975. Physical chemistry: Enriching topics from colloid and surface science. *Theorex, La Jolla*:27.

Pashley, R., and Karaman, M. 2005. *Applied Colloid and Surface Chemistry*: John Wiley & Sons.

Peng, Y., Zhao, S., and Bradshaw, D. 2012. Role of saline water in the selective flotation of fine particles. *Water in Mineral Processing: Proceedings of the First International Symposium, SME*:61-71.

Pierre, A., Ma, K., and Barker, C. 1995. Structure of kaolinite flocs formed in an aqueous medium. *J. Mater. Sci.* 30 (8):2176-2181.

Plimpton, S., Crozier, P., and Thompson, A. 2007. LAMMPS-large-scale atomic/molecular massively parallel simulator. *Sandia National Laboratories*.

Pokrovsky, O.S., and Schott, J. 2004. Experimental study of brucite dissolution and precipitation in aqueous solutions: surface speciation and chemical affinity control. *Geochimica et Cosmochimica Acta* 68 (1):31-45.

R.L.Virta. 2014. Industrial Minerals Review 2013. *Mining Engineering* 66 (7):62-63.

Rand, B., and Melton, I. 1975. Isoelectric point of the edge surface of kaolinite. *Nature* 257:214-216.

Rand, B., and Melton, I.E. 1977. Particle interactions in aqueous kaolinite suspensions: I. Effect of pH and electrolyte upon the mode of particle interaction in homoionic sodium kaolinite suspensions. *J. Colloid Interface Sci.* 60 (2):308-320.

Roy, S.K., and Sengupta, P.K. 1988. Electrical properties and the surface characteristics of lanthanum oxide/water interface. *J. Colloid Interface Sci.* 125 (1):340-343.

Scales, P.J., Grieser, F., and Healy, T.W. 1990. Electrokinetics of the muscovite mica-aqueous solution interface. *Langmuir* 6 (3):582-589.

Schneider, T., and Stoll, E. 1978. Molecular-dynamics study of a three-dimensional one-component model for distortive phase transitions. *Phys. Rev. B* 17 (3):1302-1322.

Schofield, R., and Samson, H. 1954. Flocculation of kaolinite due to the attraction of oppositely charged crystal faces. *Discuss. Faraday Soc.* 18:135-145.

Schoonheydt, R.A., Pinnavaia, T., Lagaly, G., and Gangas, N. 1999. Pillared clays and pillared layered solids. *Pure Appl. Chem.* 71 (12):2367-2371.

Schroth, B.K., and Sposito, G. 1996. Surface charge properties of kaolinite. *MRS Online Proceedings Library* 432:null-null.

Seemann, R., Herminghaus, S., and Jacobs, K. 2001. Dewetting patterns and molecular forces: A reconciliation. *Phys. Rev. Lett.* 86 (24):5534-5537.

Shang, J.Q., and Lo, K.Y. 1997. Electrokinetic dewatering of a phosphate clay. *J. Hazard. Mater.* 55 (1–3):117-133.

Siddiqui, S., Zhang, J., Keswani, M., Fuerst, A., and Raghavan, S. 2011. Study of interaction between silicon surfaces in dilute ammonia peroxide mixtures (APM) and their components using atomic force microscope (AFM). *Microelectron. Eng.* 88 (12):3442-3447.

Smith, R. 1963. Coadsorption of dodecylamine ion and molecule on quartz. *Trans. AIME* 226:427-433.

Smith, R., and Scott, J. 1990. Mechanisms of dodecylamine flotation of quartz. *Miner. Process. Extr. Metall. Rev.* 7 (2):81-94.

Sokolov, I., Ong, Q.K., Shodiev, H., Chechik, N., James, D., and Oliver, M. 2006. AFM study of forces between silica, silicon nitride and polyurethane pads. *J. Colloid Interface Sci.* 300 (2):475-481.

Suter, J.L., Anderson, R.L., Greenwell, H.C., and Coveney, P.V. 2009. Recent advances in large-scale atomistic and coarse-grained molecular dynamics simulation of clay minerals. *J. Mater. Chem.* 19 (17):2482-2493.

Swartzen-Allen, S.L., and Matijevic, E. 1974. Surface and colloid chemistry of clays. *Chem. Rev.* 74 (3):385-400.

Tadros, T.F., and Lyklema, J. 1968. Adsorption of potential-determining ions at the silica-aqueous electrolyte interface and the role of some cations. *J. Electroanal. Chem. Interfacial Electrochem.* 17 (3–4):267-275.

Thiessen, P. 1942. Wechselseitige adsorption von kolloiden. *Zeitschrift für Elektrochemie und angewandte physikalische Chemie* 48 (12):675-681.

Thomas, F., Bottero, J.Y., and Cases, J.M. 1989. An experimental study of the adsorption mechanisms of aqueous organic acids on porous aluminas 2. Electrochemical modelling of salicylate adsorption. *Colloids Surf.* 37 (0):281-294.

Van Olphen, H. 1977. *An Introduction to Clay Colloid Chemistry: for Clay Technologists, Geologists, and Soil Scientists*. New York, USA: Wiley.

Videla, A., Lin, C.L., and Miller, J.D. 2006. Watershed functions applied to a 3D image segmentation problem for the analysis of packed particle beds. *Part. Part. Syst. Char.* 23 (3-4):237-245.

Vold, M.J. 1963. Computer simulation of floc formation in a colloidal suspension. *J. Colloid Interface Sci.* 18 (7):684-695.

Wang, J., Kalinichev, A.G., and Kirkpatrick, R.J. 2004. Molecular modeling of water structure in nano-pores between brucite (001) surfaces. *Geochimica et cosmochimica acta* 68 (16):3351-3365.

Willis, M.J., Mathur, S., and Young, R.H. 1999. kaolin flotation: beyond the classical. *Advances in flotation technology. SME, Littleton Colorado*:219-229.

Xia, L.-y., Zhong, H., Liu, G.-y., Huang, Z.-q., Chang, Q.-w., and Li, X.-g. 2009. Comparative studies on flotation of illite, pyrophyllite and kaolinite with Gemini and conventional cationic surfactants. *Trans. Nonferrous Met. Soc. China (English Edition)* 19 (2):446-453.

Xu, D., and Zhang, Y. 2009. Generating triangulated macromolecular surfaces by Euclidean distance transform. *PloS one* 4 (12):e8140.

Xu, Z., Plitt, V., and Liu, Q. 2004. Recent advances in reverse flotation of diasporic ores - A Chinese experience. *Miner. Eng.* 17 (9-10):1007-1015.

Yan, L., Englert, A.H., Masliyah, J.H., and Xu, Z. 2011. Determination of anisotropic surface characteristics of different phyllosilicates by direct force measurements. *Langmuir* 27 (21):12996-13007.

Yavuz, Ö., Altunkaynak, Y., and Güzel, F. 2003. Removal of copper, nickel, cobalt and manganese from aqueous solution by kaolinite. *Water Res.* 37 (4):948-952.

Yin, X. 2012. Anisotropic surface features of selected phyllosilicates, PhD Thesis. Department of Metallurgical Engineering, University of Utah.

Yin, X., Gupta, V., Du, H., Wang, X., and Miller, J.D. 2012. Surface charge and wetting characteristics of layered silicate minerals. *Adv. Colloid Interface Sci.* 179-182:43-50.

Yin, X., Yan, L., Liu, J., Xu, Z., and Miller, J.D. 2013. Anisotropic surface charging of chlorite surfaces *Clays Clay Miner.* 61 (2):152-164.

Yu, X., Zhong, H., and Liu, G. 2010. Reverse flotation of diaspore from aluminosilicates by a new cationic organosilicon quaternary ammonium collector. *Miner. Metall. Process.* 27 (3):173-178.

Zbik, M.S., Smart, R.S., and Morris, G.E. 2008. Kaolinite flocculation structure. *J. Colloid Interface Sci.* 328 (1):73-80.

Zembala, M., and Adamczyk, Z. 1999. Measurements of streaming potential for mica covered by colloid particles. *Langmuir* 16 (4):1593-1601.

Zeng, Q.H., Yu, A.B., Lu, G.Q., and Paul, D.R. 2005. Clay-based polymer nanocomposites: Research and commercial development. *J. Nanosci. Nanotechnol.* 5 (10):1574-1592.

Zhang, P., and Bogan, M. 1995. Recovery of phosphate from Florida beneficiation slimes I. Re-identifying the problem. *Miner. Eng.* 8 (4–5):523-534.

Zhao, Q., Miller, J., and Wang, X. 2010. Recent developments in the beneficiation of chinese bauxite. *Miner. Process. Extr. Metall. Rev.* 31 (2):111-119.

Zhao, S., Hu, Y., Wang,, and D., X., J. 2003. Investigation on the flotation of aluminosilicates using n-(2-aminoethyl)-dodecanamide. *Acta Phys. Chem. Sin.* 19 (6):573-576.

Zhao, S., Hu, Y., Wang, D., Zhang, Y. 2003. Flotation of aluminosilicates using n-(3-aminopropyl)-dodecanamide. *Chin. J. Nonferrous Metals* 13 (5):1273-1277.

Zhong, H., Liu, G., Xia, L., Lu, Y., Hu, Y., Zhao, S., and Yu, X. 2008. Flotation separation of diaspore from kaolinite, pyrophyllite and illite using three cationic collectors. *Miner. Eng.* 21 (12–14):1055-1061.